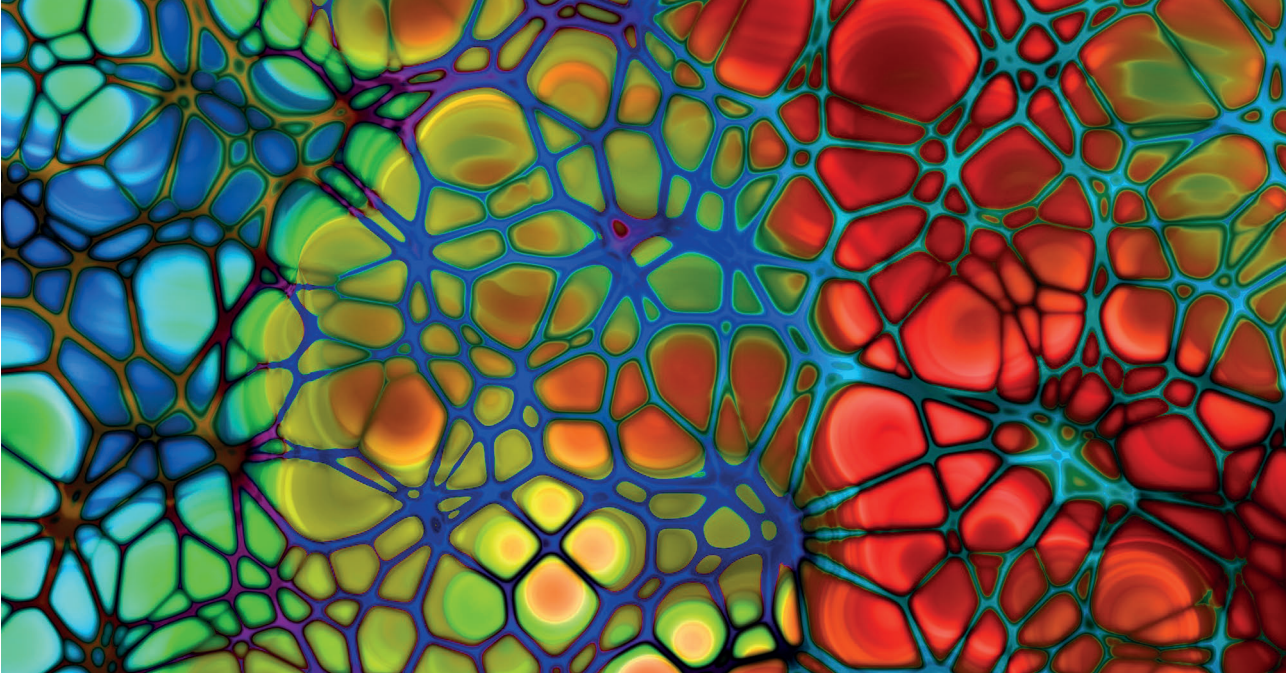

FAU Studien aus dem Maschinenbau 387

Chen Chen

Skin-equivalent opto-/elastofluidic in-vitro microphysiological vascular models for translational studies of optical biopsies

FAU University Press

Chen Chen

Skin-equivalent opto-/elastofluidic in-vitro microphysiological vascular models for translational studies of optical biopsies

FAU Studien aus dem Maschinenbau

Band 387

Chen Chen

Skin-equivalent opto-/elastofluidic in-vitro microphysiological vascular models for translational studies of optical biopsies

Dissertation aus dem Lehrstuhl für Photonische Technologien (LPT)

Prof. Dr.-Ing. Michael Schmidt

Erlangen
FAU University Press
2022

Bibliografische Information der Deutschen Nationalbibliothek:
Die Deutsche Nationalbibliothek verzeichnet diese Publikation in der Deutschen Nationalbibliografie; detaillierte bibliografische Daten sind im Internet über http://dnb.d-nb.de abrufbar.

Bitte zitieren als
Chen, Chen. 2022. *Skin-equivalent opto-/elastofluidic in-vitro microphysiological vascular models for translational studies of optical biopsies.* FAU Studien aus dem Maschinenbau Band 387. Erlangen: FAU University Press. DOI: 10.25593/978-3-96147-506-3

Umschlagsgestaltung unter Verwendung eines Bildes von:
Geralt auf pixabay.

Der vollständige Inhalt des Buchs ist als PDF über den OPUS-Server der Friedrich-Alexander-Universität Erlangen-Nürnberg abrufbar:
https://opus4.kobv.de/opus4-fau/home

Verlag und Auslieferung:
FAU University Press, Universitätsstraße 4, 91054 Erlangen

Druck: docupoint GmbH

ISBN: 978-3-96147-505-6 (Druckausgabe)
eISBN: 978-3-96147-506-3 (Online-Ausgabe)
ISSN: 2625-9974
DOI: 10.25593/978-3-96147-506-3

Skin-equivalent opto-/elastofluidic in-vitro microphysiological vascular models for translational studies of optical biopsies

Hautäquivalente opto-/elastofluidische in-vitro mikrophysiologische vaskuläre Modelle für Translationsstudien von optischen Biopsien

Der Technischen Fakultät

der Friedrich-Alexander-Universität

Erlangen-Nürnberg

zur

Erlangung des Doktorgrades Dr.-Ing.

vorgelegt von

Chen Chen M.Sc.

aus Shanghai, V.R. China

Als Dissertation genehmigt von der Technischen Fakultät
der Friedrich-Alexander-Universität Erlangen-Nürnberg
Tag der mündlichen Prüfung: 13.10.2021

Vorsitzender des Promotionsorgans:
Prof. Dr.-Ing. Knut Graichen

Gutachter: Prof. Dr.-Ing. Michael Schmidt
Prof. Dr. Jürgen Popp, Friedrich-Schiller-Universität Jena

Preface

This presented dissertation is written within the scope of my work as the research assistant at the Lehrstuhl für Photonische Technologien (LPT) of the Friedrich-Alexander Universität Erlangen-Nürnberg. The work is initiated by a preliminary scientific project of the Erlangen Graduate School in Advanced Optical Technologies (SAOT).
Here, I would like to thank my doctoral supervisor Prof. Dr.-Ing. Michael Schmidt, who financed my research work and supported me during my promotion in all aspects, as well as other tasks in the framework of industrial cooperation. I would also thank Prof. Dr. Dr. Med. Florian Stelzle as the medical supervisor of my work in the framework of the correlation with the Mund-, Kiefer- und Gesichtschirurgische Klinik (MKG) of the Universitätsklinikum Erlangen.
I would offer my special thanks to Dr.-Ing. Florian Klämpfl, the leader of the medical technologies group. Advices given by him have been a great help to me at all scientific and administrative aspects. I would also like to acknowledge the help provided by my colleagues, Martin Hohmann, Benjamin Lengenfelder, Fanuel Mehari, Moritz Späth, Rajesh Kanawade, Midhat Ahmed, and all my students involved in the repetitive work of my project. My greatest thanks go to my parents for being considerate of all my choices ever since I started with my study in Germany.

Chen Chen
15. 01. 2022
Shanghai, V.R. China

Table of contents

Symbols and abbreviations

List of symbols and units

Physical meaning	**Symbol**	**Unit**
Oxyhemoglobin concentration	$CtHbO_2$	g/L
Deoxyhemoglobin concentration	$CtRHb$	g/L
Oxyhemoglobin concentration (in-vivo)	$CtHbO_2$	$g/L.tissue\ mass$
Deoxyhemoglobin concentration (in-vivo)	$CtRHb$	$g/L.\ tissue\ mass$
Tissue oxygenation saturation	SO_2	$\%$
Blood oxygenation saturation	SpO_2	$\%$
Optical path length factor	f_{PF}	$const.$
Wavelength	λ	nm
Molar extinction coefficient	ε	$mm.mol^{-1}$
Chromophore concentration	$Ct_{Chromophore}$	g/L
Total transmittance	T_t	$\%$
Diffuse transmittance	T_d	$\%$
Absorbance	A_b	$a.u.$
Diffuse reflectance	R_d	$\%$
Scattering factor	F_{scatt}	$const.$
Absorption coefficient	μ_a	mm^{-1}/cm^{-1}
Reduced scattering coefficient	μ_s'	mm^{-1}/cm^{-1}
Young's modulus	E	mm^{-1}/MPa

List of abbreviation

Basal Cell Carcinoma	*BCC*
Squamous Cell Carcinoma	*SCC*
Positron Emission Tomography	*PET*
functional Magnetic Resonance Imaging	*fMRI*
Optical Coherence Elastography	*OCE*
Spectroscopic Optical Coherence Tomography	*sOCT*
Hue, Saturation, Luminance	*HSL*
PhotonAcoustic Tomography	*PAT*
Acoustic-Resolution Photoacoustic Microscopy	*AR-PAM*
Confocal Raman Scanning Microscopy	*CLSM*
Laser-Induced-Breakdown Spectroscopy	*LIBS*
Principal Component Analysis	*PCA*
Linear Discriminant Analysis	*LDA*
General Discriminant Analysis	*GDA*
Partial Least Squares	*PLS*
Receiver Operating Characteristic Curve	*ROC AUC*
Ultrasound modulated Optical Tomography	*UOT*
Polymethyl methacrylate	*PMMA*
Polydimethylsiloxane	*PDMS*
Thermoset Polyester	*TPE*
Polyurethane Methacrylate	*PUMA*
Norland Adhesive 81	*NOA81*
Near-infrared	*NIR*
Laminar Optical Tomography	*LOT*
Extracellular matrices	*ECM*
Photomultiplier Tube	*PMT*
Polyurethane	*PU*
Polyvinyl Chloride plastisol	*PVCp*
Radiative Transfer Equation	*RTE*
Modified Beer-Lambert Law	*MBLL*
Laser Scanning Microscope	*LSM*
Bis(2-Ethylhexyl) phthalate	*DEHP*
Continuous Wave Phosphate	*CW*
buffered saline	*PBS*
Time-of-Flight	*TOF*

Table of figures

Table of tables

1 Introduction

Operational skin biopsies are commonly done during the clinical skin lesion analysis to provide the pathological evidence of the existence of benign/cancerous lesions. However, they have shortboards in their functional uses for recognizing the metastasis of malignant skin lesions. In the case of a melanoma lesion, the metastasis spread occurs in the circumventing *extracellular matrices* (ECM) of the near/far margin around the appearing melanoma lesion site to form the metastasis components. If these metastasis components are not included in the biopsy site, the metastasis is not correctly recognized and might cause the recurrence of cancer.
Visual inspections of the superficial skin lesion site are usually done according to the ABCDE routine. Any lesion site that matches the descriptions according to the ABCDE routine[1] is regarded as a cancerous melanoma lesion. However, following the ABCDE routine is subjective, experience leaning, and brings a high chance of misdiagnosis[20]. To address this, operational biopsies of living cutaneous (skin) tissues help to address all not-confirmed cases from the skin lesion analysis through the abovementioned visual inspection. During the operation, dermatologists should be cautious so as to evade all possible complications, such as bleeding, inflammation and tissue damage[20]. Despite this, an abstraction with a large chunk of tissue in a safety margin (up to 1cm to the lesion edge for high risk patients) can be a solution, but does not help to remove all metastasis components. Regarding the diagnosis of the skin lesions containing melanocytes, J. Alcalay et al. prove that the majority (75%) of the patients show residual tumor around the operational wound of the biopsied site[21]. To more precisely position the embedded skin lesion with its metastasis components and to more safely reproduce the diagnostic results, various optical skin biopsies are developed, including optical imaging, optical angiographies and optical probes.
To more precisely and regularly monitor the skin lesion with its metastasis components in the tissue margin around the appearing lesion site, various optical skin biopsies are developed, including optical imaging, optical angiographies and optical probes. The optical biopsies reconstruct the tissue mor-

[1] (A) The lesion is *A*symmetric in shape; (B) The lesion *B*oarders are notch; (C) The pigmentation has *C*olor changes in different positions; (D) The *D*iameter of the lesion is bigger than 6mm; (E) The lesion mass *E*volutes over time.

phology, the vascularization anatomy, the tissue oxygenation metabolism, or recover the spatial distribution of cells/elements in the targeted tissue without tissue destruction. Although this non-destructiveness helps to reduce the operational complications during the clinical skin lesion analysis, it comes with a common technical constrain of clinical results validations. Unlike the direct pathological results from the operational biopsies, the optical biopsy results can only be validated on in-vitro phantoms to evaluate the performance of the imaging/angiographic resolution or validate the correctness of the recovered molecular parameters.

In principal, the tissue equivalences of the in-vitro skin phantoms, or other microphysiological skin models, within their sophistications in the bionic features, determine the correctness and comprehensiveness of the proposed phantom validations. However, the established in-vitro phantoms have not evolved to simultaneously imitate the vascularized skin/skin lesion in the blood oxygenation supply/metabolism and the biooptical/biomechanical/bioacoustical features of the skin matrices etc. This means, comprehensive tissue equivalences are missing in the established in-vitro phantoms. The discrepancies between the established in-vitro phantoms and the in-vivo skin obstacle their uses as the validation test charts during the translational studies, and therefore, must be addressed. Motivated by this, unique prototypes of opto-/elastofluidic in-vitro microphysiological vascular phantom models are investigated to simultaneously replicate the skin equivalent light/sound-tissue-interaction and the blood perfusion of the vascularized human skin.

2 State of the art

2.1 Optical skin biopsies and their applications

2.1.1 Skin lesion analysis by imaging and angiographies

A number of anatomic skin imaging approaches/angiographies have been proposed and used to replace the operational biopsies. These technologies engender cross-sectional or projection images of the cutaneous tissues (incl. scar tissue, granulation tissue, mucous cysts), the leukoplakia, and the cancer neoplasm. In Tbl. 1, the technical features and the shortboards of some established skin imaging approaches/angiographies are summarized. In the work of I. Carboni et al., the researchers use the *Positron Emission Tomography* (PET) to investigate an exophytic keratotic nodule lesion [22]. The disadvantage is its radiation dose because the system emits radiation from the radioactive substance and cannot be used for repetitive in-vivo screenings. The *functional Magnetic Resonance Imaging* (fMRI) has an advantage in acquiring soft tissue contrast. The latest modality also has spatial resolution of 10μm to image a skin lesion. However, the fMRI is profoundly expensive and is not suitable in clinics/places with low resources (technically and/or financially). The *Dynamic Optical Coherence Elastography* (OCE) features micrometer-scale resolution, non-destructiveness, and real-time processing. The OCE is designed for imaging the skin anatomy only. It is not aligned for recovering any tissue biological function. The stokes polarimetry derives multiple stoke parameters, such as the degree of polarization, the azimuth angle, and the ellipticity angles of the polarization ellipse to correspond to the topography of the targeted lesion site. However, it is not able to detect the embedded metastasis underneath the superficial skin surface[23].

Table 1: The main specifications and the induced hazards of the established skin imaging approaches/angiographies are given.

Approach	Functional recovery	Hazards	Expenses
fMRI	Molecular response	None	High
PET	None	Radiation	Acceptable
CLSM	Spectral response	None	High
PAT	oximetry measured	None	High
Polariscope	None	None	low
OCE	None	None	High
sOCT	Spectral response	None	High

A lack of functional imaging could affect the application of optical imaging for e. g. distinguishing the benign and cancerous tumor[3]. In some cases, both benign and cancerous tumor sites reflect similar vascularization morphology and only show differences in the tissue oxygenation metabolism[24]. Multi-modal functional imaging approaches are becoming the research front line because they provide information about various tissue metabolism. Apart from the skin anatomy, the functional imaging also reconstructs the tissue oxygenation, the blood hemodynamics, or recovers the distribution of specific cells/chromophores in the targeted tissue. In the established works, the integration of different optical, interferometric, photoacoustic, elastographic, spectroscopic, spectrographic alignments is the primary task. The *Confocal Raman Scanning Microscopy* (CLSM) is built to make an insight into the skin cutis and reconstructs the spatial distribution of the targeted molecules in the superficial skin. The experimental setup consists of a pin-aperture confocal scanning laser microscope and a Raman spectrometer (see Fig. 1(a)). In the microscopic alignment, a laser beam is delivered through a short-pass filter, partially reflected at wavelengths of 720 and 850nm. The light is delivered to the sample surface and scattered. The scattered light from the sample with a wavelength of 850nm is reflected. The light is then focused to a diffraction constrained spot when passing through a microscope objective. It is filtered by a laser rejection filter and focused onto an optical fiber. The core of the optical fiber is accommodated as a confocal pinhole alignment, which thresholds the light out-of-focus. The output of the fiber is connected to the Raman spectrometer. The focused laser beam scans across the focal plane over the sample surface, which can be merged with the Raman spectrograph pixel for pixel into one image.

The confocal Raman scanning microscopy gives an acquisition depth profile of 50μm to the skin surface and spatial resolution in micrometer. In the work of Sarowskin et al., the confocal Raman microscopy is used to determine the dihydrogen monoxide concentration in the skin stratum corneum. The results are plotted as the depth profile of the chromophores' concentration as a function of distance to the skin surface (see Fig. 1(b)). Semi-quantitative concentration profiles are resolved for the major constituents of certain natural moisturizing chromophores. Here, the natural moisturizing chromophores include the existence of serine, glycine, pyrrolidone-5-carboxylic acid, arginine, ornithine, citrulline, alanine, histidine, and urocanic in the tissue matrix. So far, no other non-invasive method enables the analysis of the molecular concentration as a function of distance (to the sample surface) with similar resolution to that of the CLSM[25]. However, the CLSM possesses the dis-

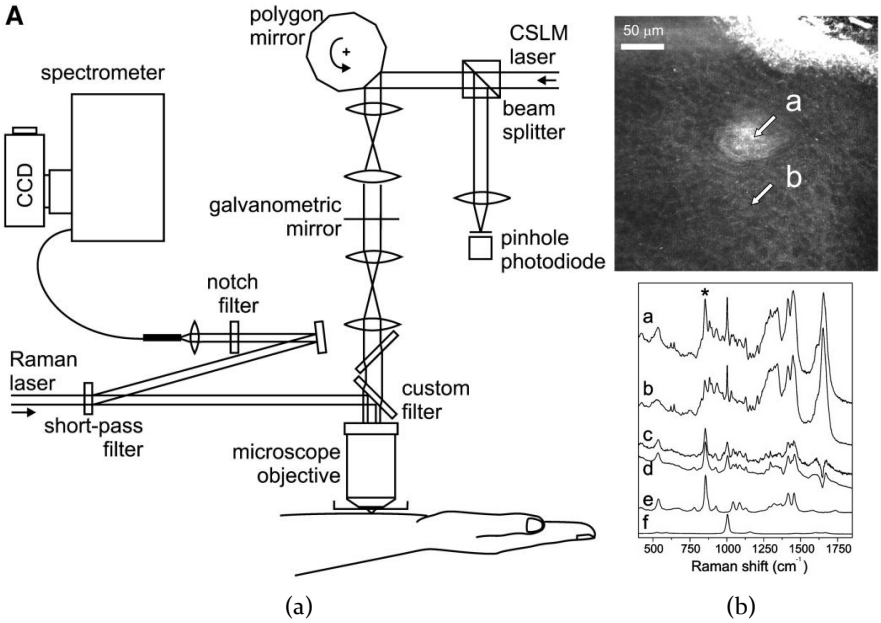

Figure 1: (a) Schematic of the CSLM setup is shown. (b) Raman spectrograph of a sweat duct on the palm, 30μm below the skin surface is given. The effulgent area is a sweat duct. Raman spectra are acquired from the marked spots. [1]

advantages of both Raman spectroscopy and confocal microscopy, namely, the expense and the facile influence of the fluorescent signal of the tissue chromophores. Besides, the effective acquisition depth of 50μm is still too shallow to detect the cancer components embedded under the skin epidermal layer.

Among all imaging targets, the angiogenesis activity is an easy-to-find marker regarding its macroscopic dimension. The angiogenesis activities occur in wound rejuvenating, in inflammatory condition, and in tumor magnification at their early stages. They induce changes in the morphology and the metabolism (hemodynamics, oximetry, etc.) of the tissue vascularization, especially in the margin around the visible lesion site. In a suspicious skin lesion, vessels start to grow in their size/density to fortify the oxygenation and nutrition of the extracellular tissue matrices. As if a dermatologist can already predict the development of a lesion by screening the angiogenesis activities in the margin around it, he/she can be precisely navigated to where the targeted cancerous cells locate during the treatment. The *Spectroscopic Optical Coherence Tomography* (sOCT) is developed to give functional ima-

ging of the skin angiogenesis activities. (see Fig. 2(a)). It is specified with approximately 5μm axial resolution and 10μm lateral resolution[2].

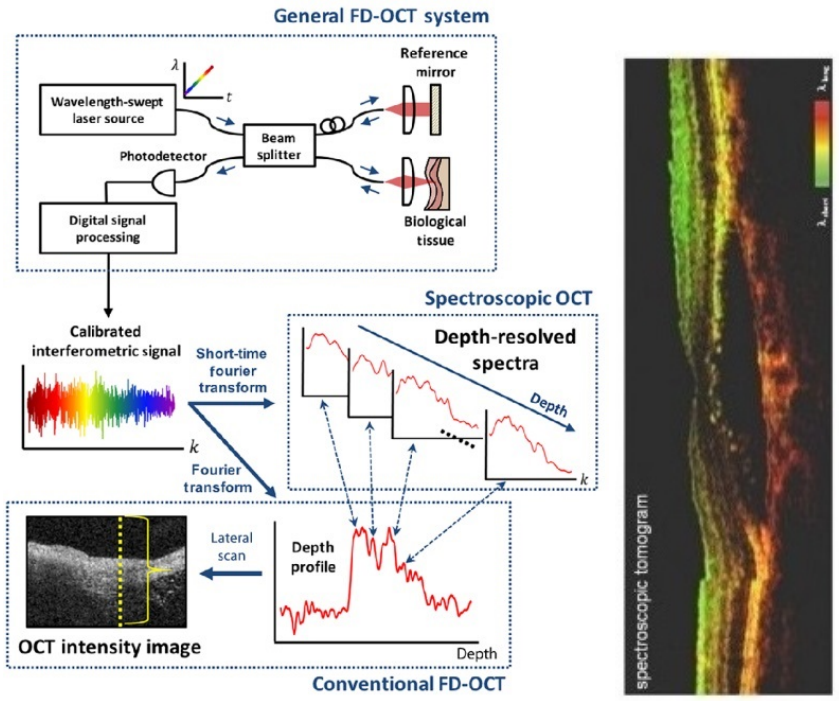

(a) (b)

Figure 2: (a) The system alignment of the spectroscopic OCT is shown. (b) The sOCT gives an image of an african frog tadpole, where the targeted mesenchymal cells in different sizes are shown in red in contrast to the scattering background in green[2].

Different from the conventional OCT, which reconstructs scattering targets only, the sOCT obtains the spectral replication of various absorbing chromophores from the targeted tissue. By using an appropriate time-frequency analysis on the light beams (both reference and sampling beams) with a broad bandwidth in their wavelengths, a depth-resolved spectroscopic profile is given. Instead of plotting an RGB picture, the sOCT image is engendered through *Hue, Saturation, Luminance* (HSL) color mapping to represent the anatomic reconstruction and the spectroscopic information in one given image. In the HSL mapping, the spectroscopic information determines the Hue, the light intensity out of the interferometer determines the Saturation, and the Luminance is kept constant. Figure 2(b) shows the

combined morphologic and spectroscopic information of an african frog tadpole in the HSL color mapping.
The sOCT is used to reconstruct the spatial distribution of the light absorbing melanocytes in the skin dermal matrices. The melanocytes are highlighted in the B-scan with a spectroscopic demonstration of a higher absorbing level to differ from the less-absorbing *extracellular matrix* (ECM). The sOCT has also been developed for extracting different tissue metabolism parameters, such as the blood oxygen saturation[2]. However, the sOCT is costly due to its sophisticated hardware. The sOCT consists of an interferometric setup, an ultrashort-pulse mode-locked Ti:Al_2O_3 laser as the light source, and an external spectroscopy module to acquire the depth-resolved spectra. Apart from this, the cost for all post-buy services (regular maintenance/system calibration) and the short stand time of the light source should be taken into consideration during its clinical deployment.
The *PhotoAcoustic Tomography* (PAT) [6] has recently been used to perform the skin lesion analysis. By using the PAT, the optical absorption in the cutaneous tissue due to the endogenous molecules, such as the hemoglobin and melanin, is reconstructed. This technical feature is used to determine whether to biopsy the skin lesions on the patients with suspected invasive squamous cell carcinoma[26]. The *Acoustic-Resolution Photoacoustic Microscopy* (AR-PAM) is built and brought into the clinical scenario of investigating the vessel distribution in the skin/lesion (see Fig. 3(a)). The spatial resolution of the PAT is similar to that of the OCT, namely, 3 to 5μm. In this establishment, a microscopic alignment is built to distribute laser pulses on the defined acoustic focus. Meanwhile, a mechanical wave transducer is synchronized to receive the generated acoustic signal from the acoustic focus. The AR-PAM reconstructs the blood perfusing vessels with better contrast and sharpness than the sOCT. Additionally, a functional reconstruction of the tissue oximetry parameters based on the optical absorption spectra can be given (see Fig. 3(b)). However, like all other photoacoustic approaches, the imaging procedure is relatively slow due to the transducer scanning speed and the repetition rate of the pulsed laser. Also, it is computationally very complex to derive the generation and propagation of the acoustic wave in an acoustically homogeneous inviscid medium from the given heating function[3].

2.1.2 Skin lesion analysis by using optical probes

Considering the cost and the inconvenience brought by the motion artifices during the clinic trials, the abovementioned optical angiographies/imaging

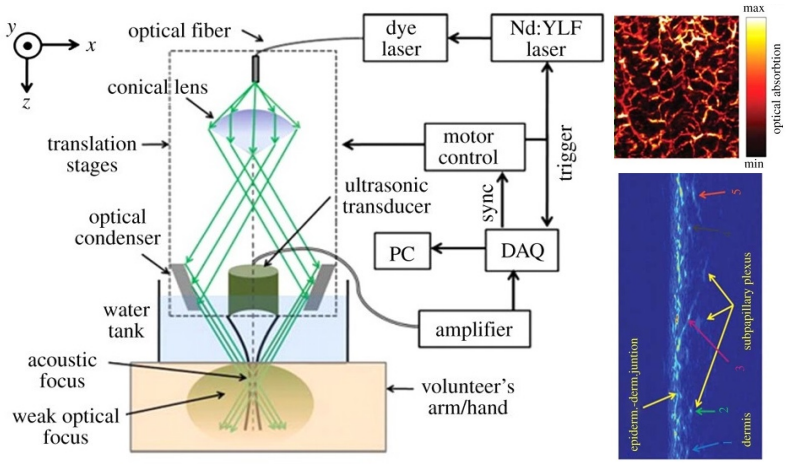

Figure 3: (a) The Acoustic-Resolution Photoacoustic Microscopy system is built and used for imaging the skin vasculature. (b) The AR-PAM reconstruction of the skin capillary network is shown[3].

are not always indispensable. To make clinical diagnoses less complicated, finding a particular biomarker of specific skin diseases at the local lesion site with an optical probe can become a more practical solution. The feasibility of using the *Laser-Induced-Breakdown Spectroscopy* (LIBS) as a novel method to analyse the elemental concentration in the human stratum corneum is already proved[27]. In this study, a 60mJ pulse energy Nd:YAG laser operating at 1064nm is used to engender the laser-induced plasma from the skin tissue. A high-resolution spectroscopy is used to acquire the optical signal from the induced plasma and records the atomic spectra from the optical signal (see Fig. 4(a)). In the case study of Sun et al., the researchers use the LIBS to detect the existence of *Zn* in the skin to differentiate the lesion from the salubrious tissue. During the experiments, an aqueous *Zn* dilution is deposited on the biceps area of the forearm for a short duration. After the quantification, it can be indicated that *Zn* is adsorbed by the skin and the concentration decrements exponentially with the depth into the superficial skin. An advantage of using the LIBS for the element detection is that the data acquisition procedure can be done simultaneously with the given laser pulse for the plasma excitation, thus allowing an online investigation of the dynamic changes in the chemical elements.

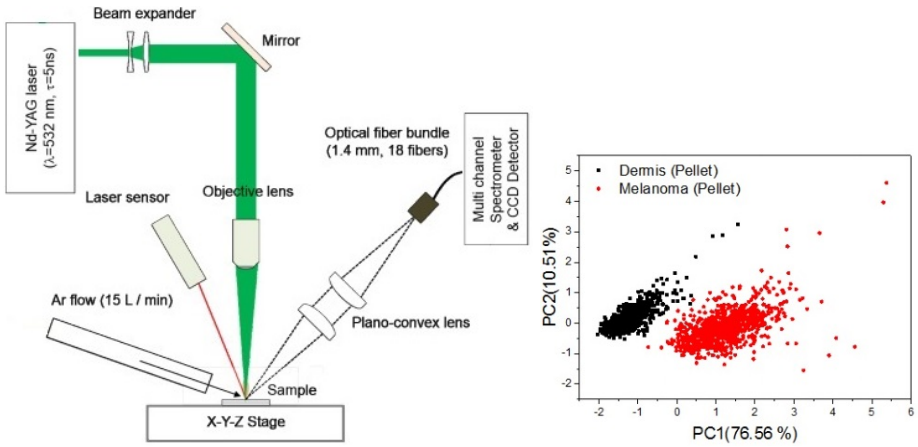

(a) (b)

Figure 4: (a) Schematic of the LIBS experimental set up used in the analysis of the excised tissue is shown. (b) The PCA scores along PC1 of the dermis pellets and the melanoma pellets are given[4].

The LIBS is used to distinguish the melanoma lesions based on the quantitative difference of elements in the epidermal lesion and the mundane dermis. Han et al. monitor the elements in the homogenized pellets from the excised skin samples of the melanoma-implanted mice. After the signal acquisition, statistical analyses on the raw LIBS spectra are performed by classifying the raw spectra through the *Principal Component Analysis* (PCA) and the *Linear Discriminant Analysis* (LDA). By comparing the results for different targeted elements, it is shown that the intensity of *Ca* in the epidermal lesion is higher than that in the dermis, which is not implanted with melanoma cells (see Fig. 4(b)). It is concluded that the epidermal lesion and the mundane dermis can be differentiated with high selectivity by either univariate or multivariate analysis of the registered LIBS spectra. It comes with an intensity ratio difference by a factor of 8 or relegation precision over 0.995[4].
The disadvantages of applying the LIBS in the skin tissue differentiation are also quite clear. The integration of the LIBS system into e. g. a laser scalpel/optical probe is involute because the LIBS signaling is very sensitive to the laser beam focusing. The motion artifacts can easily cause the defocusing of the incident laser beam and bring an erroneous spectrum. Additionally, a pulsed laser (most likely a ns-laser) and a spectrometer with sub-nanometer spectral resolution are needed, which increase the cost. Arduousness in obtaining opportune calibration standards for each individual case has to be

addressed. The tissue damage brought by the laser pulses cannot be ignored. Although the tissue ablation site is not commensurable to that of the operational skin biopsy in its size, the induced tissue-carbonization cannot easily heal.

The Raman spectroscopy is built and used to observe the vibrational, rotational, and other low-frequency modes of cell compounds when they are stimulated in their energy level. It acquires the inelastic scattering of laser that interacts with the molecular vibrations, or other excitations in the matter. In the established work of Forster et al.[5], the researchers apply an integrated real-time system of the Raman spectroscopy for in-vivo skin cancer diagnoses. They evaluate the performance of the Raman spectroscopy in differentiating skin diseases according to the registered molecular vibrations of the targeted chromophores (see Fig.5(a)). During the experiments, the benign and malignant skin lesions from the patients that carry attested skin diseases are taken as the targets. The study includes the lesion analysis of melanomas, *Basal Cell Carcinoma* (BCC)/*Squamous Cell Carcinoma* (SCC), atypical nevi, melanocytic nevi, and seborrheic keratoses (see Fig.5(b)). Based on the spectra from all these lesions, lesion relegation is made by performing the principal component with the *General Discriminant Analysis* (GDA). The study includes the tasks to abstract the skin cancers/pre-cancers from the benign skin lesions, to abstract the melanomas from the non-melanoma lesions (both with inked margin), and to abstract the melanomas from all other nevi. The results show the sensitivity between 95% and 99% and specificity between 15% to 54% in all abovementioned tasks. It can be concluded that it is practical to use the Raman spectroscopy to distinguish the malignant skin lesions from the benign lesions.

However, the induced Raman signal from the tissue, regardless of the excitation wavelength, is weak. A relatively long integration time in seconds is needed in the experimental practice to acquire Raman signals with sufficiently high intensity and reasonable read-out noise, which can additionally bring operational complications. The detection requires a sensitive and highly optimized optical probe. In most cases, Raman spectroscopy experiments must be performed in closed space without any external illumination. Besides, the fluorescence of the impurities can disrupt the Raman spectra acquisition. Some compounds in the human chromophores, such as the porphyrins, the tryptophan, and the collagen, release fluorescence to cover the induced Raman signal when they are irradiated at specific wavelengths.

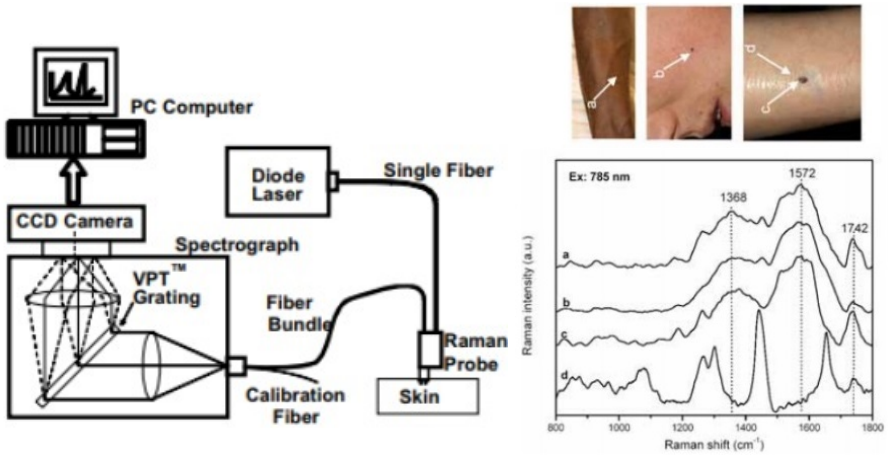

(a) (b)

Figure 5: (a) Schematic of the Raman laser probe with 785 nm excitation source is shown. (b) In-vivo Raman spectra of the cutaneous melanin are obtained from the volar forearm skin, the benign pigmented nevi lesion, and the malignant melanoma lesion respectively[5].

2.2 In-vitro phantoms for translational studies of optical biopsies

2.2.1 Challenges in phantom validations for optical biopsies

During the research on all techniques mentioned above, the researchers normally choose to first perform experiments on artificial in-vitro phantom models before the human/animal experiments. With fewer uncertainties compared to the real tissue, phantom validation provides a more controlled, repeatable estimation of the targeted tissue anatomy/function and forecasts the negative influences from the abovementioned technical shortboards of the tested system. A crucial problem is that no establish skin-equivalent in-vitro vascular phantom processes the sophistications to simulate the vascularized skin tissue from all aspects. Most established research works on phantoms/microfluidics suggest that the lamination and the smooth optical over-going of the multiple layered skin cutis cannot be simulated in phantoms[28][8]. In the established works from V.V.Tuchin and Wang et al.,[29][30], the diameter of the engendered 'microvessels' is not sufficiently proximate to that of the real cutaneous vasculature (10 - 100μm in width). The optical turbidity is not replicated in the phantom matrices to mimic the color tones/spectral features of different human skin types[28][8]. In

brief, an intact reflection of the in-vitro features, including the biophysical, biomechanical, biological and morphological characteristics of the skin tissue is missing. The established phantoms have not evolved into multi-functional tools to calibrate the multi-modal optical angiographies/optical probes mentioned above.

For instance, using a transparent microfluidic phantom as the imaging target for the spectroscopic OCT brings challenges on validating the functional recovery of the optical absorption of the melanocytes. The transparent matrix of the microfluidic phantom does not provide any absorption/scattering feature[31]. Consequently, the spectral separation of the absorbing and scattering nature of the targeted tissue must again be validated during the in-vivo experiments. The phantom validation for the *Ultrasound modulated Optical Tomography* (UOT) lacks the exact examination of the imaging resolution. In the established work, the researchers prepare light absorbing and scattering objects that are transparent to ultrasound in a phantom model. In order to check the imaging resolution of their system, a 31-gauge needle with an outside diameter of 254μm is embedded in a scattering latex sheet. Indeed, the size of the needle is too big to examine the axial and lateral resolution of the UOT system, claimed as few micrometers[32]. The mechanical properties and the acoustic impedance of the latex-based matrix are not similar to any real tissue. In the work of Beard P.C et al., the researchers validate the imaging correctness of the photoacoustic tomography device by using a phantom. This phantom comprises a *Polymethyl methacrylate* (PMMA) tube with a length of 1.3mm, which is filled with india ink and positioned in the intralipid-based liquid matrix (see Fig. 6). However, neither the intralipid matrix nor the PMMA tubing provides any similarity in the acoustic impedance to the real tissue[6].

In Tbl. 2, the major requirements on the in-vitro skin phantoms used for validating different imaging/probe approaches and the shortboards of the established phantoms are summarized[19]. On one side, the microfluidic phantoms mostly lack the replication of the optical turbidity in the phantom matrices. This obstacles the calibration of e. g. the spectrographic imaging, because the image contrast of these approaches is scaled by the separation of chromophores based on the forward/backward scattering and the absorption of the light incident on them. On the other side, the anatomic phantoms need vessel networks with an analog dimension to the real vasculature to examine e. g. the imaging resolution. Also, one should consider whether the phantom matrix could reflect the acoustic resistance/mechanical elasticity of the real

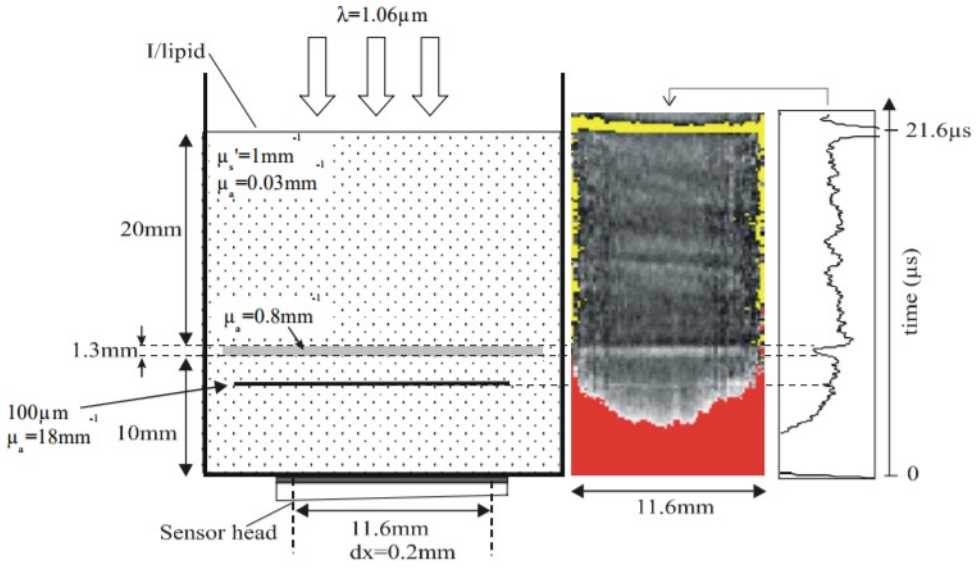

Figure 6: The phantom validation of the photoacoustic tomography device by using an intralipid-based liquid phantom is shown. This phantom comprises a length of 1.3mm PMMA tubing filled with india ink[6].

tissue because they are the decisive factors to determine e. g. the acoustic wave propagation in the tissue matrix during the acoustic imaging.

Table 2: Main specifications of the established phantoms, their applications, and their shortboards are listed[19].

Approach	Resolution	Function	Used phantoms	Short-boards
fMRI	submillimeter	Flowmetry	Anatomic	No perfusion
PAT	0.1 - 1mm	Acoustic	Anatomic	No turbidity
LOT	100 - 200μm	Oximetry	Anatomic	Big capillary
UOT	50 - 60μm	Acoustic	Anatomic	Big capillary
sOCT	5 - 10μm	Spectral	Microfluidic	No turbidity

2.2.2 Microphysiological phantoms with optical features

Microfluidic-based microphysiological phantoms provide Lab-on-a-chip solutions to imitate the skin microcirculation in the tissue capillary network. Some researchers have successfully generated hollow vasculature-mimicking microfluidic structures in the phantoms with optical turbidities[33]. In the

established work of Bykov et al. (see Fig. 7), the researchers prepare an elastomer-based skin-equivalent phantom with different vessel types. The thin vessels (ϕ = 0.2mm) are embedded in the depth of 1.4 – 2mm, similarly an embedding depth of 0.9 – 1.6mm for the middle size vessels (ϕ = 0.4mm), and 1.3 – 1.6mm for thick vessels (ϕ = 0.8mm). The variance in the vessel diameter and the embedding depth allows e. g. the validation of the resolution/depth discrimination of various tomographic imaging approaches. However, the dimension of the generated vessel is far away from that of the real cutaneous microvasculature (0.01 - 0.1mm). The turbidity of the microfluidic matrices is too low to simulate any tissue/organ[7].

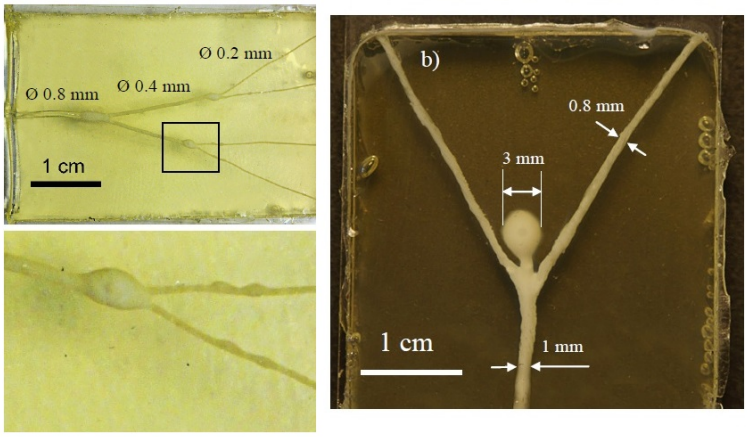

(a)

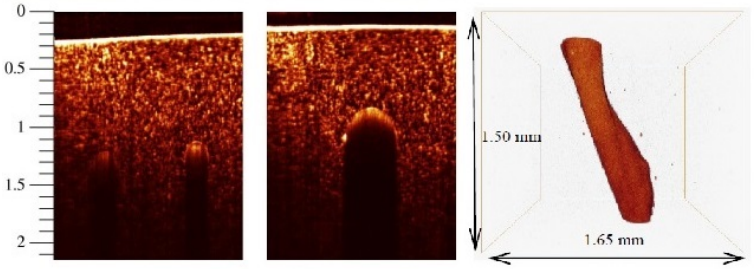

(b)

Figure 7: (a) The manufactured capillary system in a transparent phantom layer is shown. (b) OCT images of the capillaries filled with Intralipid 4% and the capillaries embedded into the scattering phantom layer filled with human whole blood are indicated[7].

An advanced example is from Wang et al.[30]. The researchers introduce a novel multiple-layered skin-simulating phantom. It is fabricated by using a light-cured 3D printer to generate microchannels in the *polydimethylsiloxane* (PDMS) matrix. The microchannels simulate the vascular anomalies and hypoxia, which are commonly observed in skin cancer. This phantom is used to calibrate a dual-modal multi-spectral laser speckle imaging system. However, it is challenging to characterize the optical parameters of the phantom matrix, after it is fabricated by the 3D printer. Also, there is no evidence to prove that the optical properties of the phantom matrix are not changed through the thermal effect brought by the light-cured 3D printing.
Lim et al. demonstrate a two-layered microfluidic phantom, which has staggered herringbone structures and artificial vasculatures in the matrix (see Fig. 8(a))[8]. However, it uses a spin-coated adhesive tape to seal the phantom slabs. This tape does not show any hydrophobicity to the inclusion in the microfluidic structure, and its adhesion can be broken off when the liquid inclusion diffuses onto the bonding interface of the tape.

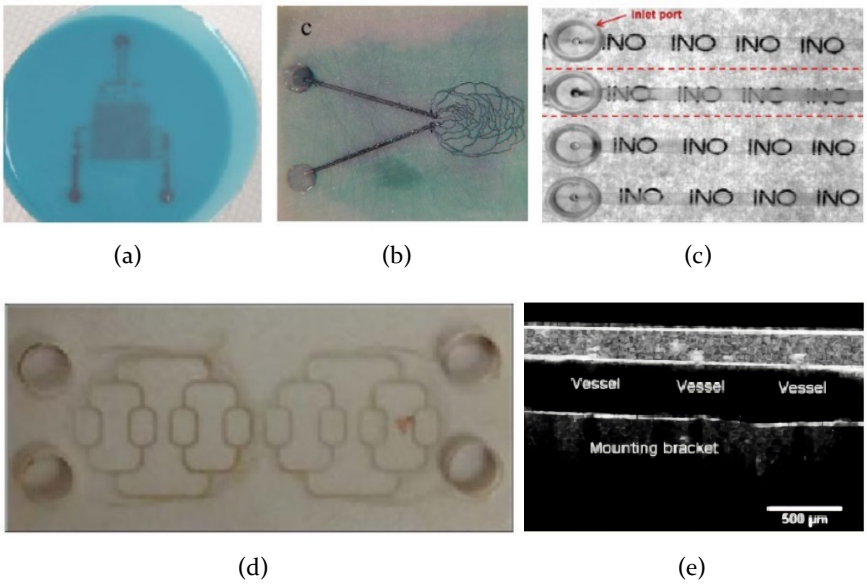

(a) (b) (c)

(d) (e)

Figure 8: (a) An example of a microfluidic phantom with scattering nature is shown. Microfluidic phantoms (b) to mimic the microvasculature in retinal layer[8], (c) with scattering fluidic flow [9], and (d) with scattering PDMS matrix to reflect the tissue optical turbidity[10] are shown. (e) A turbid microfluidic phantom with sub-millimeter scale vessels and turbid PU matrices to simulate the vascularized skin tissue is indicated in its OCT reconstruction[P4].

Paturzo et al. introduce a Lab-on-a-chip device containing microfluidic channels filled with a turbid flowing medium upon the imaging targets (see Fig. 8(c)). The microfluidic phantom is used to check the imaging contrast of a holographic imaging system [9]. However, the entire matrix of this microfluidic phantom still remains optically transparent. A unique example comes from Parthasarathy et al.. In their work, microfluidic phantoms are fabricated with PDMS and imitate the tissue capillary network. The microfluidic structure has a dimension in the range of ϕ = 10 - 150μm (see Fig. 8(d))[10]. The scientific uniqueness of this work is that it proves the possibility of mixing PDMS and *Titanium Oxide* (TiO_2) particles to achieve a certain level of optical turbidity in the microfluidic phantom matrices. The maximum concentration of TiO_2 reached is about 1.8mg per gram of PDMS. This concentration does not disturb the hydrophobic properties of PDMS to achieve the layer lamination. But at this concentration, the scattering level of human liver and skin cannot be reflected.
Principally, the limit comes from the disruption from the inserted the TiO_2 (or other) insertions on the laminate interconnection. The interconnection (see Fig.9) between e. g. the PDMS and the base substrate is the cross-links on the chemical combination of silicon and oxygenation, which connect the compound chains. They can be covalent bonds or ionic bonds. This interconnection interface requires a pure clean contact to achieve the least cross-linking degree. The introduction of e. g. the TiO_2 (as the most commonly used scatterer) is equivalent to the introduction of chemical impurity, which breaks the chemical bonds and disrupts the cross-linking[34]. Therefore, the amount of the insertions is limited so that their existence in the microfluidic matrices does not disrupt the cross-linking at the lamination interface .

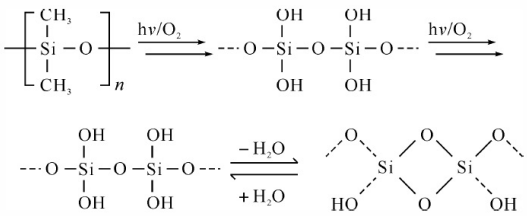

Figure 9: The chemical reaction of PDMS under UV radiance is shown. This reaction changes the hydrophobic interfaces of the PDMS layer and seals it onto e. g. another PDMS substrate.

Besides, the embossing procedures of the microfluidic structures, e. g. the laser direct writing and the heat engraving, bring thermal defect on the TiO_2 particles. Inserting high concentration scatterer into the PDMS matrix and

maintaining its turbidity during the fabrication are impossible. For all these reasons, reflecting exact the same optical turbidity in the microfluidic-based microphysiological vascular phantom matrices as that of the in-vivo/ex-vivo tissue is extraordinary challenging.

2.3 Skin lesion analysis by using diffuse optical biopsies

2.3.1 Diffuse optics in use of skin lesion analysis

Among all optical biopsies, diffuse optical biopsies require the most complicated optical spectral sophistications in the in-vitro phantoms used during the translational studies. Here, the general conception of diffuse optics and its application are first introduced to understand and define the bionic characteristics of the in-vitro phantoms proposed for the diffuse optical biopsies. The vascularization of tissue, combined with the changes in the normoxia/hypoxia status during the angiogenesis activities aid to better differentiate the lesion metabolism. For instance, the cancerous melanoma lesion has a lower oxygenation level in the lesion than that in the mundane benign nevi lesion[35]. It is concluded in the work of Paul J. Speicher et al., that the melanoma hypoxia is always found to modulate the function of the immune cells in the lesion[36]. The melanoma hypoxia can be characterized by monitoring the *oxygenation saturation* SO_2 of the targeted tissue margin/lesion. In the melanoma lesion, the SO_2 of the tissue around the appearing lesion site can be reduced to 40 %[35]. To monitor the hypoxia of the tissue margin with a good cost-efficiency, the conception of diffuse optical biopsy is proposed to derive the tissue oximetry from the spectral replication of the chromophores' absorption of light[37]. These approaches have already been used to visualize the oxygenation distribution of cerebral blood flow in breast cancer [38, 11], traumatic encephalon injury [39], and heart defect[40](see Fig. 10).
Among all diffuse optical approaches, the *Laminar Optical Tomography* (LOT) is exceptional for monitoring micron-scale targets in the human skin. The LOT has sub-millimeter resolution to reconstruct micro-lesions associated with their oxygenation status. The established LOT system consists of a confocal microscope with an array of multiple pin-holes that deliver light to a spectrometer (see Fig.11(a)).
The LOT is first developed for the multispectral imaging of rat cortex. During the animal experiments, the functional hemodynamics in various layers of the brain's cortex with a target depth profile of about 1500nm. The effective penetration depth and the imaging resolution of the LOT can help dermatologists to implement the skin lesion analysis. As the first application in

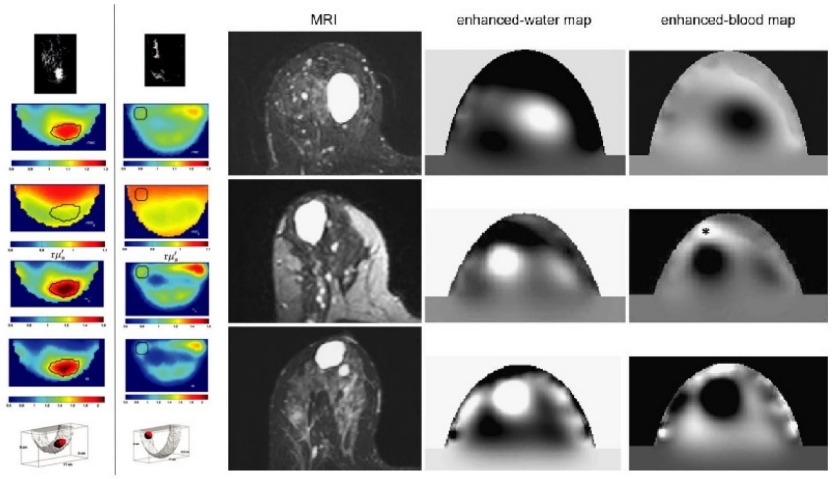

(a) (b)

Figure 10: Image is reconstructed by the diffuse optical tomography to indicate the tumor mass in (a) a breast mimicking phantom and (b) the real breast organ of a female volunteer within a tomographic reconstruction of the tissue oxygenation to mark the tumor hypoxia[11].

the skin lesion analysis, the LOT demonstrates the oxygenation metabolism during a melanoma invasion in the dermis, as reported by E. MC. Hillman et al.(see Fig.11(b))[12] .
In the work of Rajesh et al., the researchers introduce a spatially-resolved diffuse reflectance spectroscopy for monitoring the vessel density spatial pattern[13]. The setup contains a spatially-resolved optical fiber probe with multiple cores to deliver light. All assembled fiber cores are coupled to a supersensitive spectrometer to acquire the light absorption of hemoglobin as a function of the detector-to-source distance over a broadly visible wavelength range from 298 to 1092nm (see Fig. 12). The results prove that the spatial pattern of the changes in the SO_2 can be derived from the reconstructed vessel density pattern (see Fig.12(b)). This approach can potentially be used in clinical trials to monitor the changes in the skin hemodynamics and the hypoxia in the superficial skin cancer [13].

2.3.2 Diffuse optics and skin optical models

Understanding the light-tissue-interaction and its role in the diffuse optical measurement is essential for defining the biophysical in-vitro features of the microphysiological phantoms for the diffuse optical biopsies. Two crucial

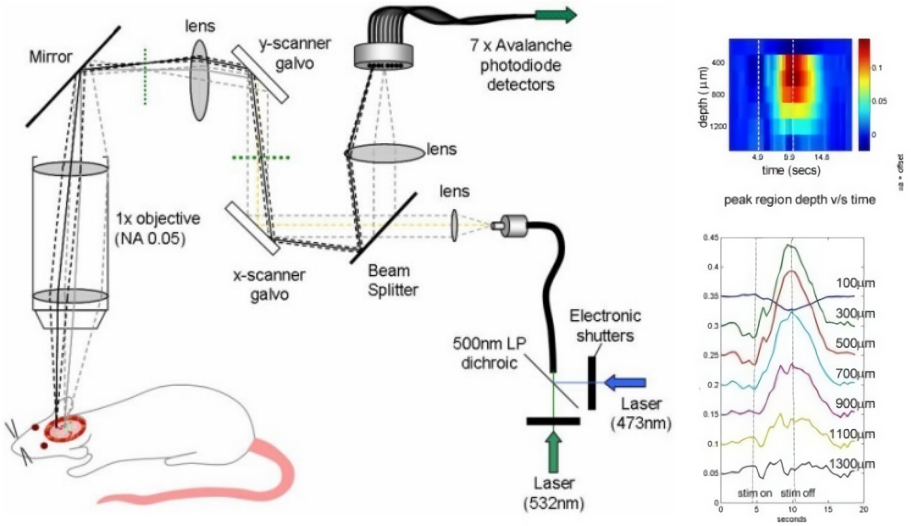

(a) (b)

Figure 11: (a) The Laminar Optical Tomography system for the depth-resolved hemodynamic imaging of rat cortex is drawn in the sketch. (b) A 50 x 50 image frame can be acquired in 100 ms. The time courses of the changes in each raw data image are shown to the right. These time courses demonstrate the differing amplitude of the signal seen by different illumination-detection pairs[12].

phenomena that decide the light-tissue-interaction are the optical absorption and scattering. The optical absorption determines how far into a matter light with a particular wavelength can penetrate before the photon is dismissed. This portion of light is absorbed, and its energy is delivered to the rotational/horizontal oscillation of the tissue compound chains. The absorption coefficient μ_a is defined as the probability of photon absorbed in the medium per unit length. Likewise, the incident light changes its propagation direction when the photon hits on a particle. To describe this, the scattering coefficient μ_s is defined as the probability of photon changing its direction when propagating in the medium per unit length. The optical anisotropy factor g is the average of the cosine of the scattering angle θ and has a probability density with a single scattering direction as a parameter. It ranges from -1 to 1, with g = 1 representing the total forward scattering and g = -1 representing the total backward scattering. From the three abovementioned optical parameters, the reduced scattering coefficient μ_s' can be calculated. It represents the probability, that a photon loses its original direction in random

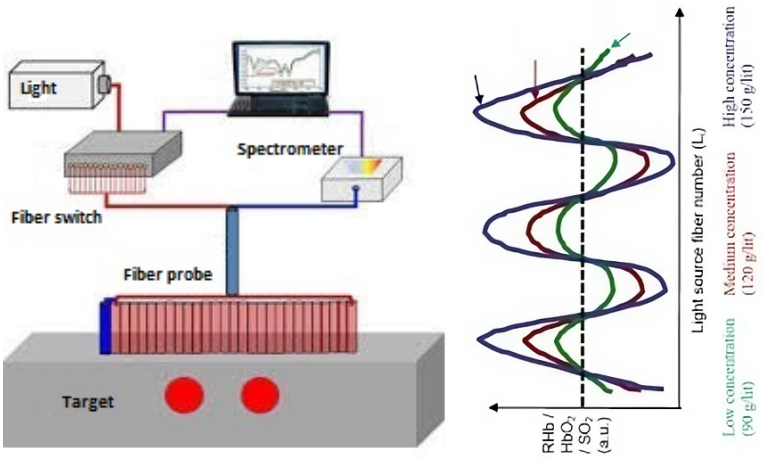

(a) (b)

Figure 12: (a) Schematic of the experimental setup for the diffuse reflectance spectroscopy is given. (b) The system is based on an optical fiber probe assembling 30 fiber cores to acquire the light attenuation from the diffusely reflected light to represent the vessel pattern[13].

walks per unit length, where each walk step involves isotropic scattering (see Equ. 1[18]).

$$\mu_s' = \mu_s(1-g) \tag{1}$$

The work principle of diffuse optics in general is expounded by the model of light propagation in turbid media. The photon trajectories through the targeted tissue with a paramount scattering from the illumination source to the detection port, which is approximated as random walks. The average length of the light path through the tissue is longer than the straight-line distance between the illumination source and the detection port. Along this photon path, the incident light is attenuated through the absorption and scattering when it hits different chromophores. In the light-skin-interaction specifically, the major chromophores include the hemoglobin in the blood mass, the hemoglobin in the skin extracellular matrices, the melanin in the superficial epidermis, the fat (lipid) in the blood mass, the fat (lipid) in the skin tissue extracellular matrix, as well as the water mass overall in the skin tissue. The absorption spectra of all abovementioned chromophores are found in Fig. 13. Among all chromophores, the hemoglobin absorbs the most amount of light in the visible wavelength range. Difference between the oxygenated and de-

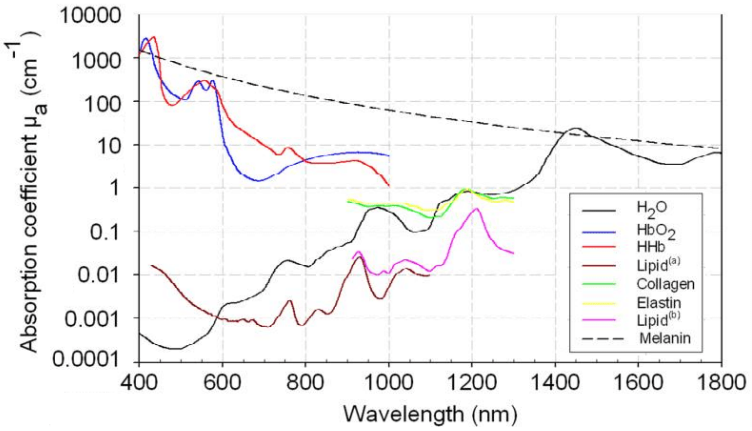

Figure 13: The absorption coefficient spectra of the major chromophores in the skin tissue are given, including the oxy-/deoxygenated hemoglobin, fat, water, and melanin etc..[14].

oxygenated hemoglobin can be judged from the difference in their spectral features. The oxygenated hemoglobin gives 2 absorption peaks at 540 and 570nm respectively, meanwhile, the deoxygenated hemoglobin gives a single absorption peak at 557nm. The diffuse optical measurements on the skin start with the acquisition of the total attenuation in the light intensity when the light passes from the illumination through the random walks in the scattering tissue toward the detection port. The portion of the light attenuation induced by the absorption of the hemoglobin is then abstracted from the total attenuation at the defined wavelengths. Based on the light attenuation and the wavelength dependencies of the oxy- and deoxygenated hemoglobin, their amount/concentration can be further quantified, and the blood oxygenation can be calculated.

To eliminate the skin structure variability on the light propagation, different skin optical models are introduced[17]. In these models, the skin-air interface and the interfaces between the skin layers are optically smooth without considering any internal reflection at the interface. The optical parameters of the epidermis/dermis come along with a constant refractive index n_{epi} = 1.45 approximately at the wavelength of 537nm and 1.42 at 577nm. The light absorption of the skin cutis mainly comes from the existence of hemoglobin in the ECM/ human whole blood and the existence of melanin pigmentation in the epidermal layer. It is presented in the following equation (see Equ. 2).

$$\mu_a = \varepsilon_{melanin} \cdot C_{melanin} + \varepsilon_{hemoglobin} \cdot C_{hemoglobin} \tag{2}$$

The absorption coefficient of the ECM can be estimated through the following empirical equation (see Equ. 3).

$$\mu_{aECM} = 7.84.10^{8}.\lambda^{-3.255} \tag{3}$$

The scattering coefficients of the epidermis and dermis are assumed to be identical. They are given by the following equation (see Equ. 4), whereby the scattering power constant b is assumed equal to 1.50. The constant C ranges from 10^5 to 10^6 cm^{-1}.

$$\mu_{s\lambda} = C.(\lambda/\lambda_0)^{b} \tag{4}$$

There is also an existing equation to calculate the reduced scattering coefficient of the skin cutis (see Eq. 5). In this equation, the rayleigh scattering factor f_{ray}, the mie scattering factor b_{mie}, and the scaling factor $a^{'}$ can be directly obtained from the literature[41]. The estimated values of the μ_a and μ_s' are given in Tbl. 6 and later compared to the values measured from the human volunteers (claimed in the later section).

$$\mu_s^{'} = a^{'} \cdot (f_{ray}(\frac{\lambda}{500})^{-4} + (1 - f_{ray}) \cdot (\frac{\lambda}{500})^{-b_{mie}}) \tag{5}$$

2.4 Challenges in phantom validations for diffuse optical biopsies

No standardized tissue-equivalent in-vitro microphysiological vascular phantom has so far been developed for validating the diffuse optical approaches, neither in the applications of the diffuse optical angiographies nor in the diffuse optical probes. In the phantom validation of the laminar optical tomography[15], a phantom with sub-millimeter absorbing structures is made to mimic the embedded absorbing targets in micron-scale (see Fig. 14(a)). The phantom includes a human hair suspended horizontally in the tissue-like liquid. The LOT data is acquired as the hair is sequentially lowered into the liquid, and concludes about the lateral resolution and the depth discrimination of the LOT (see Fig. 14(b)).
However, when work is conducted toward the functional recovery of the tissue oxygenation saturation, no corresponding phantom is prepared to simulate the blood perfusion to substitute the embedding of the solid hair in the phantom matrix. The solid hair gives no optical absorption feature to simulate the real human blood. The experimental strategy is not consistent to approve the correctness of the recovered tissue oximetry during the in-vivo

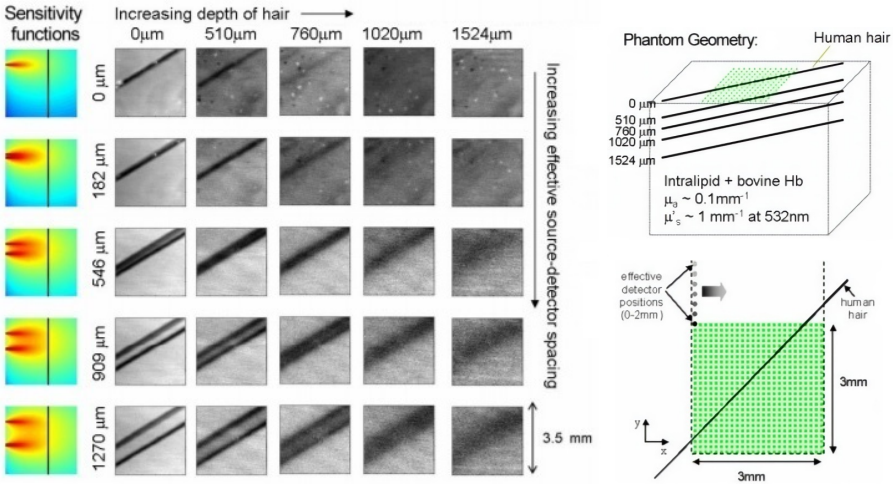

(a) (b)

Figure 14: (a) The raw LOT data acquired on the phantom consisting of a human hair lowered into the absorbing and scattering liquid is given. Far left show the simulated sensitivity functions for each separation corresponding to the raw data. Each column of data shows the hair at gradually deeper depths. Each row is a wider separation between the light source and the detector. (b) The phantom geometry is shown. [15].

experiments. Also, this in-vitro phantom models the skin cutis as a simplified single-layered homogeneous light scattering bulk. Neither the sophistication in the inhomogeneous spatial distribution of the light absorbing/scattering chromophores, nor the multi-layered structure of the cutaneous tissue is replicated in the phantom.

In the translational studies of the spatially-resolved diffuse reflectance spectroscopy[13], the researchers prepare a rigid polyurethane-based tissue phantom to replicate the vessel pattern of the vascularized skin tissue. The polyurethane matrix of the phantom is inserted with TiO_2 and india ink to tune the color tune of the phantom. In this phantom, the absorption coefficient and the reduced scattering coefficient of the PU matrices are tailored to reflect the turbidities of the real cutaneous tissue. The physical parameters of the vessel density pattern, namely the diameter of the capillary channel, are defined and range from 200 over 400 to 1000nm (see Fig.15). However, with this dimensional scale, neither the artery/vein nor the capillary vessel can be simulated properly in the size (diameter).

Concluded from the state of the art of the in-vitro microphysiological vascular phantoms and their applications in the translational studies of

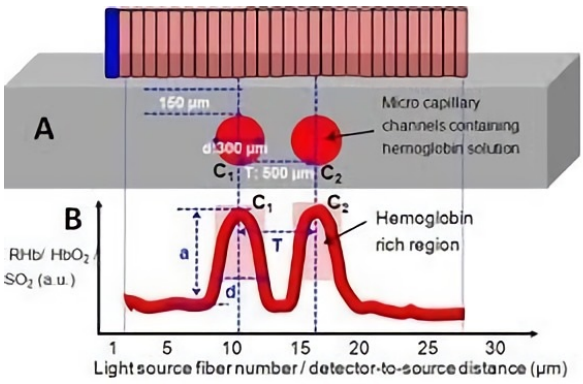

Figure 15: (a) Schematic of the polyurethane-based skin mimicking tissue phantom to mimic the artificial microcapillary channels perfused with blood and the results of the spatially-resolved diffuse reflectance spectra recovered from the phantom are given[13].

the optical biopsies, especially the diffuse optical biopsies, none of the established in-vitro phantoms possesses sufficient bionic features to simultaneously validate the angiographic/imaging results and the functional recovery of the molecular parameters. Consequently, the correctness and comprehensiveness of the biooptical measurements in the proposed phantom validations are missing. The performance of the validated optical imaging approaches/angiographies/probes or their multi-modalities can be doubtful. Including the mechanical/acoustical sophistications in the in-vitro microphysiological phantom matrices is even more elusive. It usually involves the insertion of plasticizers in the phantom matrices, which directly changes the polymerization and breaks the lamination of the multiple layered phantoms. To address all these challenges, novel hybridpolymer-based artificial in-vitro microphysiological phantoms with microfluidic structures (to simulate the skin vascularization) and all biophysical skin-equivalences to the real human skin, as well as a unique process to fabricate such phantoms are needed.

3 Objective and work flow

3.1 Scientific aim

In this work, unique prototypes of opto-/elastofluidic in-vitro microphysiological vascular phantom models are investigated to simultaneously replicate the skin equivalent light-tissue-interaction, the sound-tissue-interaction, the blood perfusion function, and the anatomic features of the vascularized human skin. In these opto-/elastofluidic phantoms, a total flexible manipulation of the μ_a/μ_s', E, the sound wave propagation characteristics, and other physical sophistications in their matrices is allowed to simulate the existence of all major chromophores in the skin cutis. Meanwhile, the anatomic structure of the hollow vasculature is perfused with blood-equivalent artificial human whole blood to functionalize the 'oxygen supply' in the microcirculation of the microphysiological phantom. A diffuse optical biopsy is then built and used in the first translational study to register the oximetry parameters on the prepared in-vitro microphysiological vascular phantoms. A flowchart of all work packages is given in Fig. 16, and the proposed hypothesis is explained as following.

3.2 Hypothesis and work flow

- **Hypothesis:** The first hypothesis is that optofluidics with unlimited amount of chemical impurity in the matrices, namely the insertion of nano-spheres and molecular dyes in the sub- and superstrate matrices, can be laminated. This enables the manipulation of the optical properties of the optofluidic in-vitro phantom matrices.

  Work flow: Ultra-short pulse laser micro-fabrication is used to shape the microvascular structure in the prepared optofluidics. The μ_a and μ_s' values of the real skin tissue are measured in their wavelength dependencies on the chosen human volunteers in-vivo. The μ_a and μ_s' values of the phantom matrices are tailored and characterized to approach the ex-vivo, as well as the in-vivo results.

- **Hypothesis:** The second hypothesis is that plastisol can be laminated directly without any polar/medium-polar adhesive. It can be used as the elastofluidic phantom matrices, which can be assigned with the defined randomness in the propagation of light/sound wave and the same sophistication in the mechanical reaction to the load as the real soft skin tissue.

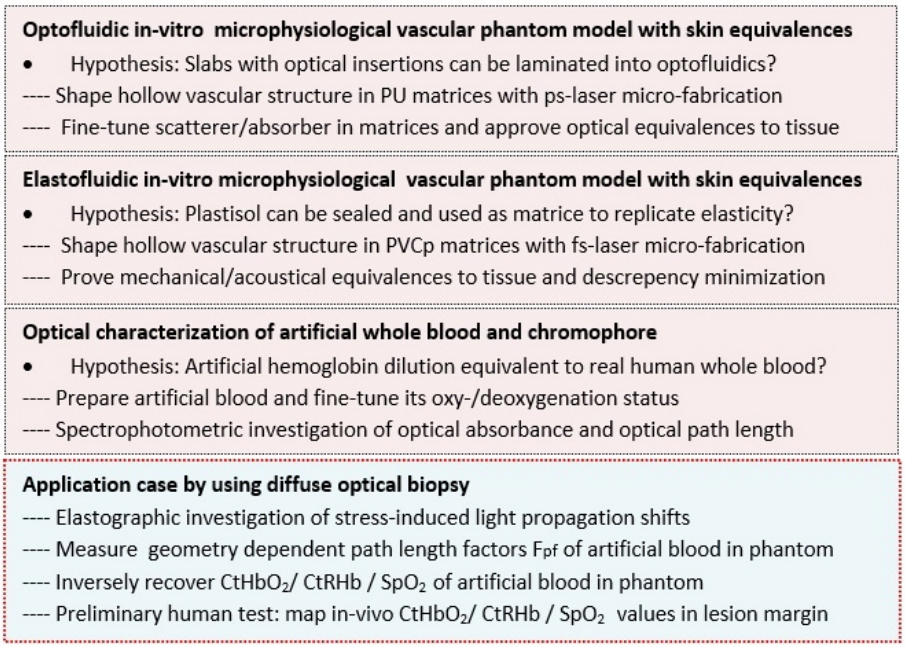

Figure 16: The research strategy, the hypothesis, and the working contents of each work package are given.

Work flow: PVCp-based elastofluidic phantoms are prepared to incorporate the mechanical elasticity of the soft skin cutis. They simulate the vascularized soft skin tissue of the human volunteers in the Young's moduli E and the sound wave velocity. Light propagation shifts due to the mechanical contact/load at the elastofluidic phantom surface are studied through optical elastography. Differences in the chromophores' heterogeneity between the skin tissue and the elastofluidic phantom matrices are discussed.

- **Hypothesis:** The third hypothesis is that artificial whole blood can be prepared to replicated the f_{PF} of the real human whole blood in their global distribution to prove their equivalences in the optical absorbance and the light path length. This aims to give the same light-blood-interaction of the artificial blood as the real human whole blood.

  Work flow: Artificial hemoglobin dilutions are prepared in oxy-/deoxygenated status respectively. They contain the same major blood chromophores as those in the real human whole blood. Their optical ab-

sorbance spectra in the wavelength dependencies are measured, and the time-stability of the measured optical properties is evaluated.

For the first application case, a compact fiber-based diffuse optical biopsy is built and used to recover the hemoglobin concentration of the artificial blood included in the opto-/elastofluidic in-vitro microphysiological vascular phantoms. A full calibration of the f_{PF} values of the oxy- and deoxygenated hemoglobin dilutions is done on all prepared phantoms with different optical turbidities to study their dependencies on the hemoglobin concentration, the oxygenation status etc. Inverse measurements of the *oxyhemoglobin concentration* Ct_{HbO_2}, the *deoxyhemoglobin concentration* Ct_{RHb}, and the *oxygenation saturation* SO_2 on the opto-/elastofluidic phantoms, based on the recovered f_{PF} values of the artificial blood, are performed. Here, the use of the modified Beer-Lambert Law and its boundary conditions are discussed. Preliminary in-vivo experiments are done on the chosen human volunteers to reconstruct the tissue metabolism in a nevi lesion and a potential subcutaneous nodule lesion. During the experiments, the recovery of the tissue oximetry parameters in the near and far safety margins around the superficial lesion sites by using the diffuse optical biopsy is done to simulate its future use in clinical trials. Discrepancies between the phantoms and the real cutaneous tissue in the recovery of the oximetry parameters are investigated and discussed.

4 Material and methodology

4.1 Preparation and characterization of in-vitro vascular phantoms

4.1.1 Optical characterization of human skin in-vivo

The μ_a and μ_s' of the human volunteers' skin are measured without blood fraction as the reference to later define the optical properties of the in-vitro vascular phantom matrices. An asian female (31 years old, no anemia, no tinea infected) and an asian male (29 years old, no anemia, no tinea infected) are chosen as the human volunteers. In these studies, the μ_a and μ_s' of the cutaneous tissue in different body parts, including the forehead, the wrist, and the neck are collected to omit the possible transmutations in the light propagation on body hairs. To quantify the optical parameters of the skin extracellular matrix without any perturbance from the blood mass, the vascular perfusion is occluded by dressing a direct press around the area of interest (see Fig. 17). All experiments are repeated 13 times, and the results are plotted with an average value with standard deviation.

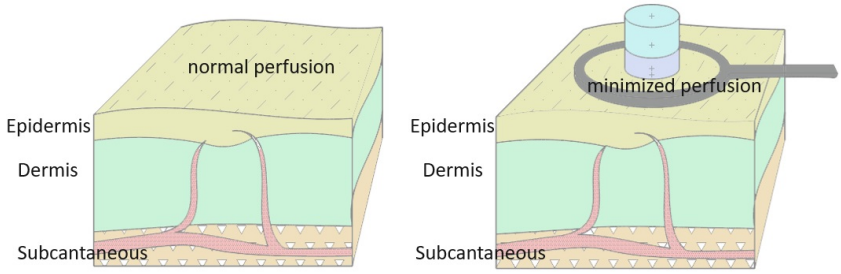

Figure 17: A metal ring is used to occlude the blood perfusion at the area of interest for measuring the optical properties of the cutaneous extracellular matrices without blood fraction.

The measurements are done by using the bifurcated fiber probe to perform the path length spectroscopic quantifications of the targeted skin sites. The diffuse optical probe consists of a fiber probe head, a CW spectrometer module, and a white light source. The bifurcated fiber is used as the illumination-detection pair (see Fig. 27). Steadily on each sampling point, light is coupled from a 200W white light source (Mercury 200 W, Newport Co., US) through a fiber collimator into the illumination core and delivered to the sample (skin/phantoms).

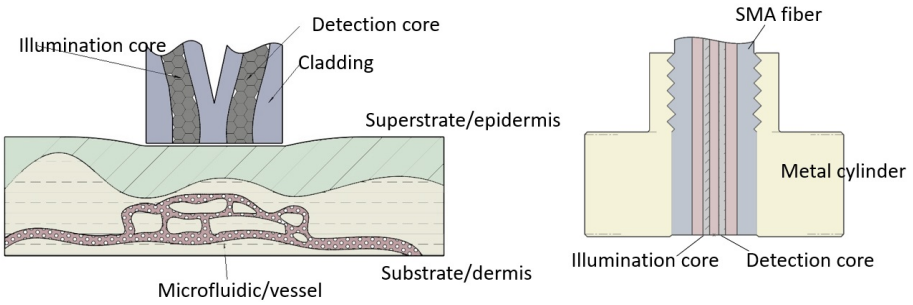

Figure 18: The bifurcated optical fibers, the fiber probe head, and the aperture separation between the illumination core and the detection core are drawn in the sketch. A cutaneous tissue model with a lesion embedded under the epidermis is also given to indicate the positioning of the diffuse optical probe on the tissue/phantom sample.

The diffusely reflected light from the sample is acquired through the detection core toward a scientific grade *Continuous Wave* (CW) spectrometer (Compact spectrometer Serie, Thorlabs Co., US). The bifurcated fiber has a core separation of 65μm. The bifurcated fiber itself is mounted in a standard SMA head and affixed to a metal cylinder with 1cm in diameter through screw level to form the diffuse optical probe head (see Fig. 27). The bifurcated optical fiber probe measures the optical reflectance $R(\lambda)$ within the illumination-detection separation. The semi-empirical reflectance model employed in this study is expressed in the following equation (see Equ. 6), whereby the $R(\lambda)$ stands for the diffuse reflectance, the μ_a and μ_s' stand for the absorption and the reduced scattering coefficients of the targeted skin site respectively. There are two constants that depend on the geometrical characteristics of the optical probe, with k1 = 0.025 mm^{-1} and k2 = 0.057 mm^{-1}. Same experiments are done on the elastofluidic phantoms (in regime with no 'vessels' underneath the superstrate) preliminarily to check their equivalences to the skin in the μ_a and $\mu_s^{'}$ values. This helps to judge whether the elastofluidic phantoms can be used to simulate the skin of the chose human volunteers in the light-tissue-interaction.

$$R(\lambda) = \frac{1}{k_1 . \frac{1}{\mu_s'} + k2 . \frac{\mu_a}{\mu_s'}} \tag{6}$$

Due to the fact that the blood is excluded by clogging the tissue margin around the sampling point, the absorption coefficient calculated in Equ. 6 represents the value of the skin extracellular matrices only. The absorption of the melanin in the skin epidermis is regarded as a minor factor, as the skin

color tone of the selected asian human volunteers (both male and female), is rather light and close to the color tone of the caucasian skin.

4.1.2 Turbid optofluidic phantoms to mimic vascularized skin

The optofluidic in-vitro microphysiological vascular phantom simulates the vascularized skin tissue from 3 aspects: the superstrate/substrate to simulate the skin tissue ECM, the perfusion channels to simulate the blood vessels, and the pumping facility to give the blood circulation function. The end product is the optofluidic phantom system as shown in Fig. 19. By connecting a membrane dosing pump (FEM 1.10 KT.18 S, Carl Roth) to the optofluidic phantom on its inlet, the prepared hemoglobin dilutions (mentioned later) can be injected into the hollow optofluidic structure. The outflow is remitted back to the blood reservoir through the outlet. This recycling mimics the blood perfusion from the artery through the capillary network into the vein.

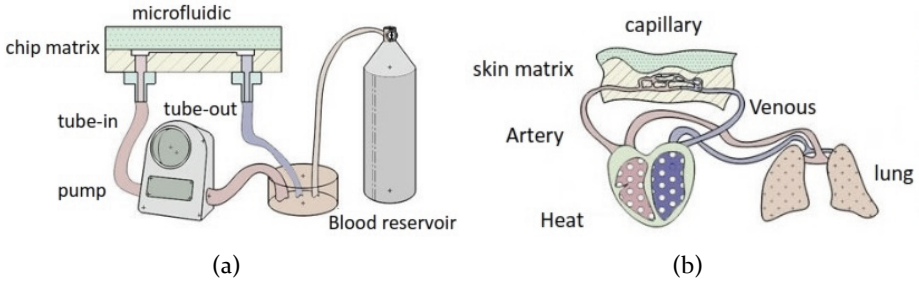

Figure 19: (a) Schematics of the optofluidic phantom, its connection with the membrane pump, and (b) the blood flow in the skin microcirculation are given.

The diameter of the cutaneous vasculature (capillary) ranges from 10 to 100μm. The microvascular network is mostly located in the first 200μm of the skin. In the design of the vascular structure in the optofluidic phantom, the inlet is split into 4 branches and these branches are then merged to the outlet. The inlet is located on one side and has a diameter of 1mm to accommodate the incoming fluid flow. The outlet in the same dimension is situated on the other side at a symmetrical position. The diameter of the branches between the inlet and outlet is set at 50μm (see Fig. 20(a)). The designed pattern is put into an SLM scanning system, coupled with a ps-laser (TBWP Fuego ps-laser, Time-Bandwidth Products AG, Switzerland). The laser beam spot is positioned and scans over a copper film along the outline of the DFX-drawing. The copper mold is then cut from the copper

film through the laser ablation along the drawn pattern. The output power of the laser is set at 1.45 W, and the beam diameter is 10μm. The frequency of the pulse repetition rate is set at 25 kHz, and the linear scanning speed is 600 mm/s (see Fig. 20(b))[P1].

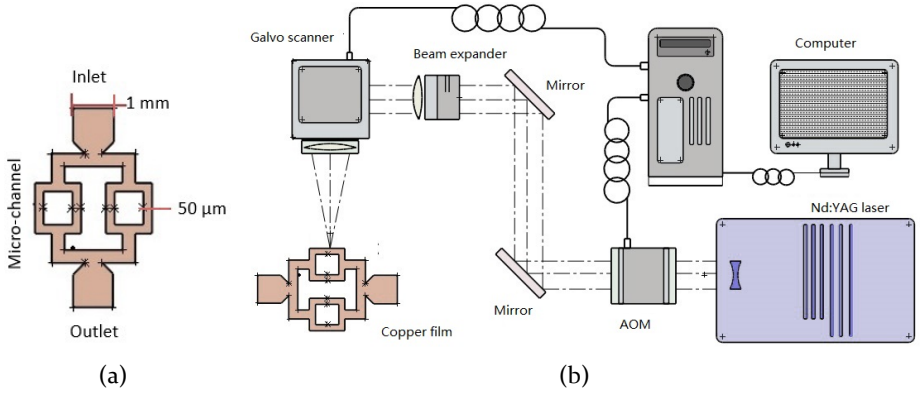

Figure 20: (a) Schematic of the optofluidic pattern design is demonstrated. (b) Schematic of the ps-laser system used for the fabrication of the mold from the thin copper film is shown[P1].

The structured copper mold is embedded between the laminated *polyurethane* (PU) super- and substrate. Contact between an electrolysis pool and the embedded copper is made through the drilling holes over the defined positions for the inlet and outlet. The electrolyte perfuses through the hole and 'dissolves' the embedded copper mold through electrolysis reaction. The schematic of the etching pool is shown in Fig. 21. The pool consists of 2 plastic beakers, which are joint by the copper mold in the sealed phantom. This makes it possible for electrons to pass from the electrolysis pool in one beaker to that in the other. Platinum wires are used as the anode/cathode pair. Over-saturated *sodium chloride* (NaCl) solution is prepared as the electrolyte. In one beaker, the copper captures electrons from NaCl in the electrolyte, turns into *copper chloride* ($CuCl_2$), and flows into the electrolyte pool. In the other beaker, NaCl captures electrons to turn into *chloride gas* (Cl_2). This fabrication procedure is called the Embedding-and-Etching.
The optofluidic phantom matrices (both super- and substrate) are constructed of castable aliphatic 2-components polyurethanes (PU WC-783, BJB Enterprise Co., US). To replicate the optical properties of the skin epidermis and dermis, TiO_2 powder (Sigma-Aldrich GmbH, Germany) and India ink (Pelikan GmbH, Germany) are inserted into the PU. The recipes, together with the mimicked skin types are listed in Tbl. 3. The additives are mixed

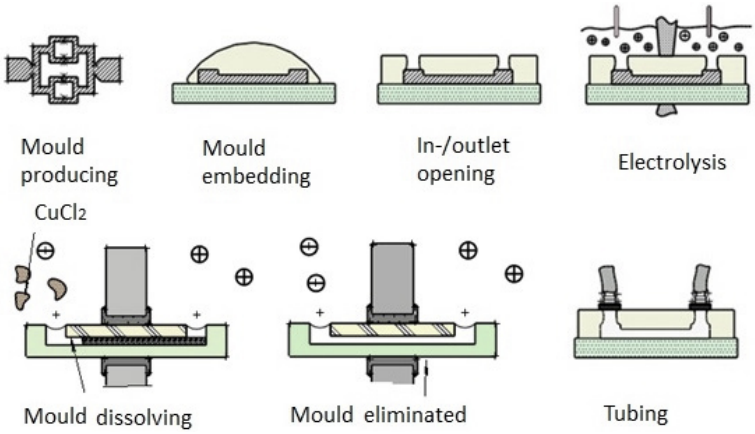

Figure 21: The Embedding-and-Etching method to fabricate the optofluidic phantom is given in the sketch. It includes the following processes: preparing copper mold by using ps-laser, embedding mold, laminating layers, in-/outlet drilling, eliminating copper mold in electrolysis, and lastly connecting with microtubing[P1].

with the PU and dispersed by stirring for 30 min, followed by an ultrasound bath (Elmasonic P, Elma Hans Schmidbauer GmbH, Germany) at 45 °C. The PU slab (the 'epidermal layer') is first casted and de-molded after 0.5 h. The second layer (namely, the 'dermal layer') is directly casted upon the half-solidified 'epidermal layer' and directly laminated, where the structured copper mold is sealed in-between (see Fig. 21). The 'epidermal layer' is 200μm in thickness, while the 'dermal layer' is 400μm in thickness.

The μ_a and μ_s' of the PU matrices are measured with the SHIMADZU spectrophotometer (UV-3600, SHIMADZU Corp., Japan). The spectrophotometer has 2 detectors; a *Photomultiplier Tube* (PMT) for the UV/VIS range and a cooled PbS detector for the near-infrared range. It gives spectral resolution of 0.1nm. Spectral resolution of 2nm is defined for a precise quantification with acceptable time-efficiency. The sampling beam is gathered by a single integration sphere, whereby the light intensity is measured and compared to the reference beam to evaluate the absorbance, the transmittance, and the reflectance (see Fig. 22).

To improve the accuracy of measuring the *diffuse reflectance Rd* and to give more precise values when calculating the μ_a and μ_s', an entrance port is customized with a diameter of 1.5mm and installed to the integration sphere. The collimated transmittance of the light beam passing through the downscaled port is measured. After the measurement, the Inverse Adding Doubling is used to convert the measured raw spectra into the μ_a and μ_s' spectra. All

Table 3: The phantom norm, the concentration of TiO_2 and india ink, correlated to the mimicked skin types, are listed as following[P1,P4].

Norm	Types	Ct [TiO_2] (g/40 mLPU)	Ct [Ink] (μL/40 mLPU)	Cutis type
Phantom1	Caucasian	0.5	120	Epidermis
Phantom2	Caucasian	0.25	120	Epidermis
Phantom3	Caucasian	0.25	60	Epidermis
Phantom4	Caucasian	0.25	30	Epidermis
Phantom5	Caucasian	0.25	20	Epidermis
Phantom6	Caucasian	0.37	30	Epidermis
Phantom7	Caucasian	0.175	30	Dermis
Phantom8	Caucasian	0.38	30	Dermis
Phantom9	Negroid	0.5	240	Epidermis
Phantom10	Caucasian	0.3	80	Epidermis
Phantom11	Caucasian	0.4	80	Epidermis
Phantom12	Caucasian	0.05	120	Epidermis

experiments are repeated 13 times. The μ_a and $\mu_s^{'}$ at specific wavelengths are plotted in the average value $\pm$ standard deviation and compared to the data from the ex-vivo biometrology studies[17, 18, 42, 43, 44, 45] to prove the skin equivalence of the optofluidic phantom matrices in the optical turbidity.

4.1.3 Turbid elastofluidic phantoms to mimic soft skin

To achieve a higher sophistication in the in-vitro phantom model, elastofluidic phantoms are prepared to simultaneously simulate the optical turbidities and the mechanical elasticities of the human skin. This feature helps

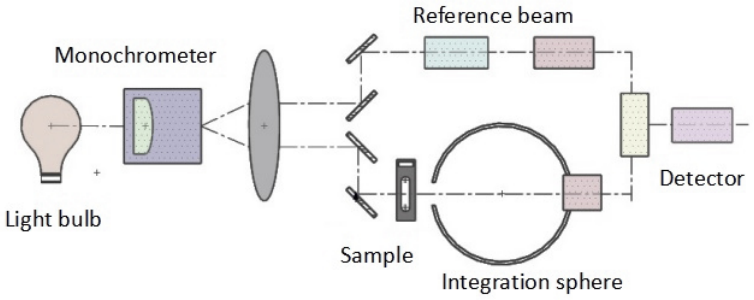

Figure 22: The light path in the SHIMADZU spectrophotometer with a single integration sphere and 2 detectors for the optical signaling is shown.

to eliminate/minimize possible discrepancies to the real soft skin tissue of the human volunteers. The bridge between the optofluidic and the elasto-fluidic phantoms is that they apportion a similar recipe for the insertion of the scatterers/absorbers in the phantom matrix. They are supposed to reflect the same μ_a and $\mu_s^{'}$ in the phantom matrices. The bridge between the elastofluidic phantoms and the targeted human skin during the in-vivo studies is the parity in the matrices' color tones, the similarity in the optical turbidities, and the similarity in the mechanical elasticities. The relegation of the skin color tones is done according to e. g. the Fitzpatrick scale. [1] The quantified μ_a and $\mu_s^{'}$ values are relegated according to the skin's appearance and correspond to the phantom databank to find the phantom with the same/most similar μ_a and $\mu_s^{'}$ values (see Fig. 23). In this case, the elastofluidic phantoms with the norm OP6 is prepared to represent the asian female and OP8 to represent the asian male because their color tones match according to the Fitzpatrick scale (see Fig. 23). The Norm and recipes of the phantoms are seen in Tbl. 4.

Figure 23: The correspondence of the color tone between the elastofluidic phantom matrices and the skin of the asian male/female volunteers is shown. The PVCp slabs in different color and the skin sites at the forehead of the chosen human volunteers are indicated.

Thin hollow microchannels with a min. width $\phi = 20\mu$m are derived at a depth of 200μm to the elastofluidic phantom surface (see Fig.24(a) and (b)). The vasculature mimicking structure includes 12 separate microchannels (sized from 200μm in the center to 100μm on edge), which imitate the artery, the veins, and the capillary network respectively. A rhombus-shaped resolution test target is placed at the center of a 1mm x 1mm square to represent the micro-lesion morphology. A dimensional gradient from 1mm to 20μm is purposefully made to achieve the min. dimension of the human micro-lesions. The in-/outlets are located on the upper/middle/bottom sites, and all have a width of 2mm to accommodate the liquid flow.
The workflow of the fabrication procedure, so-called the Chemical-Tunnel-Shielding, is shown in Fig.24(c)). The option for the mold material is the

[1] The Fitzpatrick scale is a scoring system to categorize the skin types upon the amount of human skin pigmentation. Higher the score is, darker the skin color tone appears.

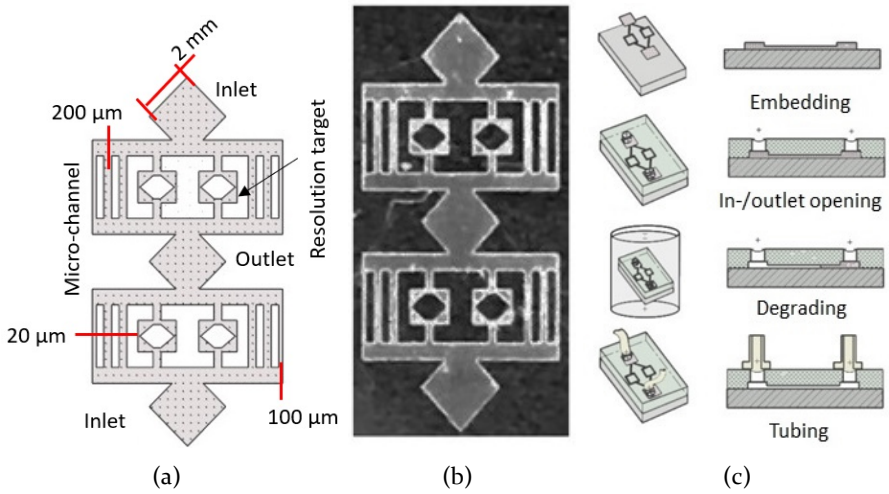

Figure 24: (a) Schematic of the elastofluidic pattern design and (b) a microscopic picture of the starch paper mold are given. (c) The workflow of the Chemical-Tunnel-Shielding procedure, including the steps for embedding, laminating, degrading, and tubing, is shown.

starch pulp paper, which is a chemical pulp product of boiling and bleaching the mixture of amylum (powder), lecithin, potassium alum, gelatin, and water. This material can be degraded in water and does not react with the plastisol matrices. A fs-laser (ORIGAMI XP fs-laser, Onefive GmbH, Switzerland) is used to cut the designed geometry from prepared the starch paper (20μm in thickness) into the mold. The laser used here is a Yb-YAG laser with an operating wavelength of 1030nm, and the pulse repetition rate is 50kHz. The pulse energy is kept constant at E_{pulse} = 11.1 μJ, and the scanning speed of 200 mm/s is set.

After the structured starch mold is made, it is embedded between the laminated PVCp layers. Water perfuses through the drilling holes over the in-/outlets and degrades the embedded pulp paper mold through amylohydrolysis (with distilled water). The amylohydrolysis reaction is performed at 40°C, at which the plastisol-based phantom matrix does not undergo any phase change in its compound chain. Powder formed α-amylase (Enzyme-Amylase, Sigma-Aldrich, Germany) is added into the water to accelerate the amylohydrolysis reaction. After the amylohydrolysis reaction ends, the hollow elastofluidic structure remains to stay between the laminated PVCp matrix (see Fig. 24).

Due to the high flexibility in the mechanical elasticity, PVCp (Plastisol medium, Lure Factor co. UK) becomes the first option for constructing the ma-

trices of the elastofluidic phantom. To replicate the optical/mechanical properties of different skin tissue types, TiO_2 powder (Sigma-Aldrich GmbH, Germany), molecular dye (Pelikan GmbH, Germany), and Lubricant worm oil softener (Lure Factor co. UK) additives are inserted into the PVCp matrices. The recipes for the scatterers/absorbers/softener are given in Tbl. 4. The additives are dispersed by stirring for 2 min, followed with an ultrasound bath (Elmasonic P, Elma Hans Schmidbauer GmbH, Germany) at 45 °C for up to 30 min. The PVCp is then heated to 350 °C and further homogenized through 300 Hz magnet stirring to smash the agglomeration of the absorbers/scatterers in the PVCp material. All mentioned fabrication steps are performed with the help of a vacuum line, which creates a UHV environment to release the air bubbles generated when stirring the viscous PVCp. The heated PVCp is casted, pressed to planar form, and gradually cooled down to 50°C for plasticization. As the final product, a pressure resistant lamination of the PVCp super- and substrate is obtained, and the elastofluidic phantom is then finished. The μ_a and $\mu_s^{\cdot}$ of the slabs are measured by the SHIMADZU spectrophotometer used previously with the same resolution configuration. Mechanical characterizations of the prepared PVCp slabs are performed according to the DIN-ISO-527-1 protocol.

Table 4: The recipes for preparing the PVCp matrices with defined optical/mechanical properties and the phantom norm are listed.

Norm	Ct [Worm oil] (μL/40 mLPVCp)	Nom	Ct [TiO_2] (g/40 mLPVCp)	Ct [Dye] (μL/40 mLPVCp)
Me1	0	Op1	0.5	120
Me2	0.1	Op2	0.25	120
Me3	0.2	Op3	0.25	60
Me4	0.3	Op4	0.25	30
Me5	0.4	Op5	0.25	20
Me6	0.5	Op6	0.37	30
Me7	1	Op7	0.175	30
Me8	1.5	Op8	0.38	30
Me9	2.5	Op9	1	120
		Op10	0.3	80
		Op11	0.2	160
		Op12	0.05	120

Acoustical *Time-Of-Flight* (TOF) measurements are performed to acquire the acoustical properties of PVCp matrices. To do this, an Nd-YAG ns-laser (Q-smart 450, Quantel Laser co., Germany) is used to generate acoustic waves at

the surface of a 3x3x3 cm PVCp cubic. The pulse duration of 5 ns, the pulse energy of 50 mJ at the wavelength of 532 nm are set. During the measurement of the velocity of acoustic wave transmitting through the sample, the pulsed laser light is incident on the sample placed on the top of a contact transducer (Atalas transducer CN2R-10, OLYMPUS co., Japan). This transducer has a typical bandwidth of 85 %, a nominal element size of 10 mm and a near field of 7.2 mm. All measurements are repeated 10 times.

4.1.4 Optical elastography of light propagation in phantoms

The refractive index of the elastofluidic phantom matrices/skin tissue can be mutated when they are loaded with mechanical forces. The light propagation can be shifted under the physical contact between the diffuse optical fiber probe head and the skin/phantom surface. It should be assured that the light delivery at the contact site is not shifted when the probe is placed on the sample surface. To first investigate how light propagation can be shifted around the contact site, a monochromatic polariscope is built to perform the optical elastography study. It consists of 2 linear polarizers, 2 quarter-wave plates, an LED light source (λ = 630 nm), and a CMOS camera (Compact USB 2.0 CMOS Cameras, Thorlabs, Germany). The normal force is placed perpendicularly onto the optical probe head through a lever and delivered to the transparent PVCp thin phantom slabs (see Fig. 25).

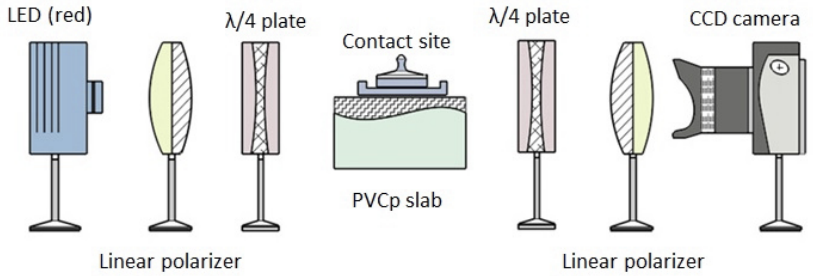

Figure 25: Schematic of the optical elastography setup is given. The inner stress distribution is recorded by the compact CMOS camera from the red LED light source through a set of polariscope.

The normal force is defined at 1, 2, 5, and 10 N. The normal force of 10 N actually exceeds the exact need and is only implemented for redundancy. The CMOS camera records the isocline lines from the last piece of the polarizer, and the isoclinic interference pattern is binarized during the image post-processing. A visualization of the stress intensity (fringe order: 0, 1/2, 1, 3/2,

2, 5/2, etc) in different parts of the phantom (near/far to the contact site) is performed. Recovered from the fringe pattern, the induced mechanical force distribution on the soft skin mimicking phantom slabs is seen. The phantom slabs are constructed with the same Polyvinyl Chloride plastisol as that of the elastofluidic phantoms without any optical insertion (recipe is found in Tbl. 4). The PVCp liquid cumulation is molded as a transparent thin slab-shaped specimen with a thickness of 5mm.

4.1.5 Preparation and optical characterization of artificial whole blood

Fresh human whole blood should be injected into the opto-/elastofluidic in-vitro phantom to simulate the blood micro-circulation. Due to the restriction in medical ethics and the amount of blood needed, it is preferred to prepare artificial blood dilutions instead of drawing real whole blood from human. About 95% of the blood dry mass is hemoglobin. In males, the total hemoglobin concentration ranges from 120 to 140 g/L. In non-anemia females, the range is 110 to 130 g/L. For preparing the artificial blood to simulate the real human whole blood, powder form dried hemoglobin (human hemoglobin, Sigma-Aldrich. Co., US) is diluted in liquid buffer and converted into the oxygenated and deoxygenated status (see Fig. 26).
For deoxygenating the hemoglobin dilution, *Sodium Hydrosulphite* ($Na_2S_2O_3$) (Hemoglobin Human, Sigma-Aldrich. Co., US) is donated and mixed with the prepared hemoglobin dilution, while *Sodium bicarbonate* ($NaHCO_3$) is used for oxygenating the hemoglobin dilution. *Phosphate buffered saline* (PBS) (Sigma-Aldrich. Co., US) is used as the host buffer. The PBS used preserves a stable pH value of 7.2-7.6, which benefits the conversion of the hemoglobin dilution into the oxy- and deoxygenation status. The fat (lipid) in the real human whole blood is simulated by diluting intralipid (20 % Intralipid, Sigma-Aldrich. Co., US) in the same PBS buffer. The intralipid dilution concentration is about 0.4 % to mimic the existence of lipid in the real whole blood. After each single chromophore is prepared, they are mixed into one dilution. The oxygenated hemoglobin dilution shows pinky light red color, while the deoxygenated hemoglobin dilution in dark brownish color (see Fig. 26).
The optical properties of all artificial chromophores, including the hemoglobin (alone), the intralipid, and the water mass, are investigated individually by using the SHIMADZU spectrophotometer with the same resolution configuration as that for the measurements of the phantom slabs. To contain the liquid sample, a quartz glass cuvette (1mm thickness, Altmann Analytik

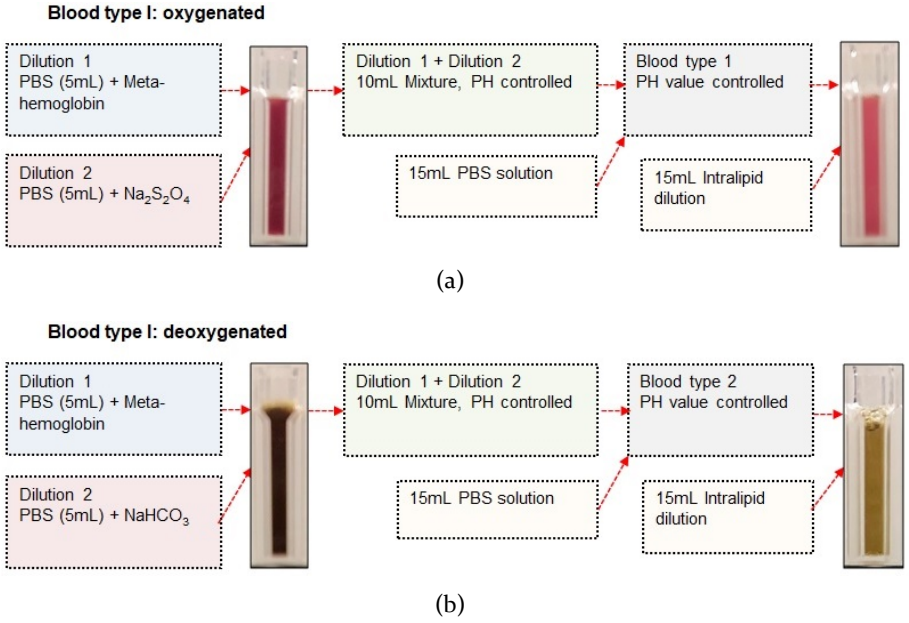

Figure 26: Pictures of the hemoglobin dilutions in the (a) oxygenated and (b) deoxygenated status, as well as the preparation workflow are shown.

GmnH, Germany) is used, which itself gives total optical transparency in the wavelength range from 350 - 1000nm. The recorded spectra are compared to the results from the established biooptical studies to prove the equivalences of the artificial chromophores to the real chromophores correspondingly.
The equivalence between the artificial chromophores and the real chromophores also requires the equivalence in the optical path length. The optical path length factor f_{PF} of the prepared chromophores is vigorously dependent on the geometry of the illumination-to-detection setup. In this case, the spectrophotometer is giving a transmission mode of the light path from the incident light illumination through the sample in the cuvette toward the detector. Meanwhile, the light path of the diffuse optical probe is in a reflection mode. The quantified f_{PF} values from the spectrophotometer/diffuse optical probe must be different, even on one same sample. Nevertheless, it still gives an estimation of the value range to compare to the spectroscopic results from other studies on the real human whole blood, and aids to prove the equivalence of the artificial blood to the real human whole blood. The path length factors of the artificial chromophores measured by the spectro-

photometer are calculated from the quantified values of the light absorbance through the Beer-Lambert-Law shown as following (see Equ. 7),

$$Absorbance^{\lambda_i} = exp(\varepsilon^{\lambda_i}_{Chromophore} \cdot d \cdot Ct_{Chromophore} \cdot f^{\lambda_i}_{PF}) \tag{7}$$

whereby, the ε stands for the molar extinction coefficient of the chromophores, the $Ct_{Chromophore}$ stands for the molar concentration of the prepared chromophore (calculated from the mass concentration[45]), the d stands for the sample thickness (1mm), and the f_{PF} stands for the to-be-calculated optical path length factor. The specular reflection at the cuvette surface is assumed to be zero because the incoming light beam is perpendicularly incident onto the cuvette. All experiments are repeated 13 times to plot an interval of all f_{PF} spectra in the wavelength range from 350 to 1000nm.

4.2 Translational studies of diffuse optical biopsy

4.2.1 Experimental setup of diffuse optical biopsy

The first prototype of the diffuse optical biopsy is built based on the diffuse optical probe mentioned previously. The diffuse optical probe-based approach is initially proposed to recover the light attenuation at the local skin site, while the experiments proposed in this section are automatized to give a 2D mapping of the light attenuation distribution in the sample to provide better visualized results. To realize this, the bifurcated fiber probe is montaged to a set of motorized scanners (see Fig. 27(a)). Components of the bifurcated fiber and the scanning stages are coupled together in a housing cage (A drawing of the housing cage is found in the appendix). The motorized stage (M-663 ®motion stage, Physik Instrumente GmbH, Germany) has a motion range of 18mm and a 2μm minimal motion step length to scan over the sample within a point-to-point scanning scheme.
Two orthogonally aligned motion stages enable a combined scanning along X and Y directions. The spectrometer and the motion stages are synchronously triggered with a controller (C-867.260 PILine ®Controller, Physik Instrumente GmbH, Germany) through an I/O socket (TTL signal, analog: 0 - 5V square) to start/stop the spectrum acquisition. On each measuring point, one acquisition is gated by a TTL triggering signal (from the controller) after the stage brakes. The entire cycling of motion, brake, trigger, acquisition, and delay on each single measuring point lasts 30ms. The sketch of the scanning scheme is seen in Fig. 27(b)
The entire scanning procedure is monitored by a closed-loop DIP controller embedded in the motion stage. The sensor reads the angular change of the

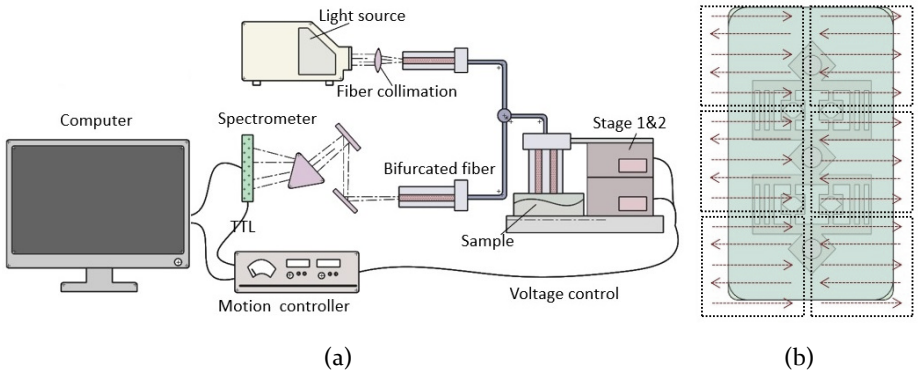

Figure 27: (a) Schematic of the diffuse reflectance probe montaged on the mechanical scanning stages is shown. (b) A simple demonstration of the scanning scheme upon the phantom/tissue sample is given.

rotational motor and sends a signal to the controller to provide error rectification of the stage motion. The closed-loop control ascertains that the positioning system, in this case, the motorized stage, reaches the commanded position. It adopts interferometric calibrations for each stage to corroborate the position in each motion step. Typical linearity deviation in the open-loop is 7% while the deviation of the calibrated closed-loop system is lower than 0.01%. This allows motion resolution of about 15nm to minimize the scanning shift in the given scanning scheme.

4.2.2 Investigation of blood oxygenation on phantoms

The modified Beer-Lambert law is chosen to separate the light absorbance of the hemoglobin from the total light attenuation *OD* measured by the diffuse optical probe (see Equ. 8). Unlike the optical path length factor calculated from the spectrophotometer studies, the f_{PF} in the modified Beer-Lambert law represents a proportionality factor converting the source-detector separation into the average light path length. It describes that light peregrinates through a focal region of chromophores change in the light diffuse reflectance. In this case, the f_{PF} of the hemoglobin dilutions is not only decided by the absorptivity of the chromophore itself but also dependent on the illumination-detection pair geometry. Eventually, the f_{PF} values of the hemoglobin dilutions can be influenced by the existence of the other chromophores in the tissue ECM/phantom matrices. The MBLL is adopted in its focal form (see Eq. 8)[46]. In this equation, the oxygenated hemoglobin, the

deoxygenated hemoglobin, the minor existence of melanin, as well as the turbid tissue ECM/phantom matrices are assigned with their own path length factor correspondingly.

$$OD^{\lambda_i} = [\varepsilon_{HbO_2}^{\lambda_i} \cdot CtHbO_2 \cdot d \cdot f_{PFHbO2}^{\lambda_i} + \varepsilon_{Hb}^{\lambda_i} \cdot CtRHb \cdot d \cdot f_{PFRHb}^{\lambda_i}] + F_{scatt} \quad (8)$$

According to the conclusion of the established research, the F_{scatt} can be solved mathematically if the light scattering is inhibited. The F_{scatt} equals to the extinction coefficient ε of the tissue/phantom matrix multiplied by the photon path length. One alternative to solve the F_{scatt} is to estimate its value through the deviation of the diffusion equation based on the μ_a and μ_s' of the tissue ECM/phantom matrices (see Equ. 9). The μ_a and μ_s' values of the phantom matrices involved in the calculation are obtained from the previous spectrophotometric studies on the PU slabs.

$$f_{PF}^{\lambda_i} = \frac{1}{2}(\frac{3\mu_s^{'}}{\mu_a})^{1/2} \cdot [1 - \frac{1}{(1 + d(3\mu_a \mu_s^{'1/2}))}] \quad (9)$$

To obtain the f_{PFHbO2} and f_{PFRHb2} from the phantom, a projection image over the opto-/elastofluidic phantoms with included oxy- and deoxygenated hemoglobin dilutions in different defined concentrations is given. The light intensity attenuation OD is directly taken from the image in its pixel, as each pixel contains the belonging spectral information. These mentioned values are taken from the recovered image in the regime, which is regarded as the 'vascular structure', or in other words, where the hemoglobin dilutions flow through. The F_{scatt} is first calculated in its spectral dependency and reduced from the total light attenuation OD. After this, the optimized forms of the f_{PFHbO2} and f_{PFRHb2} are attested and given in the exact values based on the known $CtHbO_2$ and $CtRHb$ values.
During the inverse measurements, the opto-/elastofluidic phantoms are injected with the oxygenated and deoxygenated hemoglobin dilutions with predefined concentration. Unlike the measurement of the f_{PFHbO2} and f_{PFRHb2} as described in the previous step, the defined concentration is kept single blind to the investigator during the experiments. The same measurement of the light intensity attenuation is done, the hemoglobin concentration $CtRHb$ and $CtHbO_2$ are calculated based on the known values of the optical path length factors obtained previously. It is noticed here that the recovered $CtRHb$ and $CtHbO_2$ values are presented by the mass concentration per liter dilution in unit mass. Correspondingly, the presentation of the f_{PFHbO2} and

f_{PFRHb} should match, and gives a unit in mass concentration. The $CtRHb$ and $CtHbO_2$ are calculated on the same reference, namely, on one same phantom, which allows a normalization between these values. Based on all these, the absolute values of the oxygenation saturation SO_2 are calculated (see Equ. 10).

$$SO_2 = \frac{CtRHb}{CtHemototal} = \frac{CtRHb}{CtRHb + CtHbO_2} \tag{10}$$

4.2.3 Pilot studies of lesion analysis on human volunteers

For the in-vivo experiments on the human volunteers, reconstructing a spider nevi lesion on the female volunteer to distinguish its malignancy is first performed. The spider nevi lesion on the wrist is chosen as the target, because the cutaneous arteries and veins in this body part are relatively more superficial. This makes it easier to find the lesion visually and simplifies the experimental procedure. For the same reason, The female asian volunteer is chosen, because the epidermis of females is thinner, optically less scattering, and hairless. Similar to the experiments on the in-vitro microphysiological vascular phantoms, scanning experiments are performed to give the mapping of the $CtHbO_2$, $CtRHb$, and SO_2 distribution in the margin around the lesion.

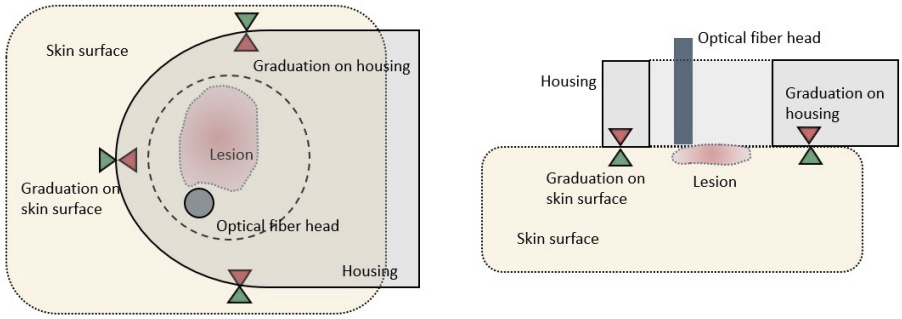

Figure 28: The optical fiber probe is placed above the lesion by matching the scale graduation (in red) at the housing surface of the optical probe head to the graduation (in green) at the skin surface.

The optical fiber head is placed on the tissue surface by matching the scale graduation on the housing of the fiber head probe to those marked on the skin surface (see Fig. 28). By doing this, the targeted lesion, as well as the margin around it, can be properly included in the proposed scanning scheme. As the result, images of the margin (5 X 5mm diameter of each stitch) of the vascular

spider are given and stitched, where the telangiectasia and the swollen blood vessels of the nevi lesion are located (see Fig. 29(a)). This dimensional scale is chosen for each stitch for the interest of short scanning time, thus minimizing the motion artifacts during the experiments.
The optical fiber probe is also directly used to acquire the light attenuation and read the tissue oximetry parameters in a diminutive margin (near margin, 2cm in diameter) and a sizably voluminous margin (far margin, 4cm in diameter) around the lesion (see Fig. 29(b)). Such an implementation of experiments follows the suggested protocol for placing the operational skin biopsy as mentioned in the introduction. The most used protocol would be followed, as some dermatologists even suggest a safety margin with 0.5cm distance from margin board to lesion center. The distance of 1cm to the lesion center is chosen to correspond to the literature cited previously[21]. The shape of the safety margin is adjusted to fit the shape of the lesion under investigation.

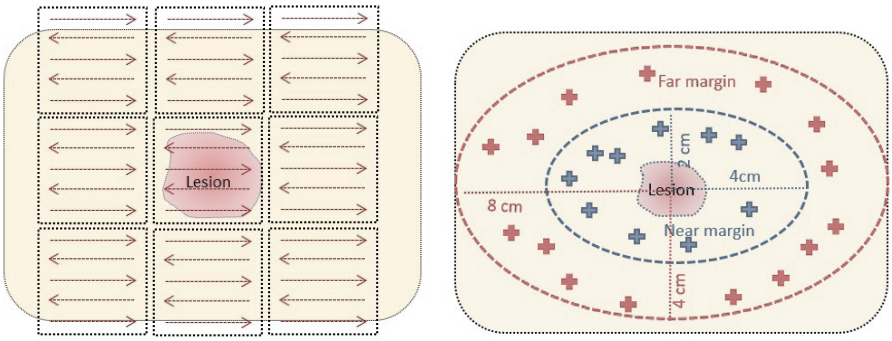

Figure 29: The experimental procedure of using the diffuse optical biopsy for the lesion analysis is shown, within (a) the scanning projection experiments and (b) the probe studies.

Similar experiments are performed on the asian male volunteer, who is suspicious of having a potential nodule site under the superficial skin surface on the knee. Likewise, scanning experiments and probe studies are done around the embedded nodule lesion to recover the tissue oximetry parameters. Here, both spider nevi lesion and nodule lesion should reflect the normoxia metabolism at the lesion site as well as in the margin around the lesion because they are both benign lesions according to their medical definition.

All optical measurements are carried out with the fiber-coupled mercury lamp. The light intensity at the fiber end is far below a sunny day light (approx. 70 mW/cm^2). The measurements mainly cover the wavelength range from 500 to 900nm in order to exclude damages to the skin tissue by UV light. The intensity at the end of the fiber is 1-2 mW/cm^2, and each measurement takes a very short time at the site (2 seconds for a single probe study, 5 min for an entire scanning scheme). According to DIN-EN-62471, an irradiation duration of up to 10 mW/cm^2 is safe for the retina and duration of approx. 100000 seconds for the skin tissue. No photochemical or thermal effect is induced in the skin tissue within a total working time of 300 seconds. According to ANSI, an intensity of 200 mW/cm^2 is safe for the skin tissue. Pain, inconvenience, or injury of the personnel are excluded. The used optical probe is not contact-free. The possible hygiene problems can be solved by cleansing the skin surface with medical washing lotion and cleaning the optical probe with 70% ethanol before and after the measurement. In view of the expected use, the possible risk is justifiable. The ethical permission and the agreements from the human volunteers are found in the appendix.

5 Optofluidic and elastofluidic in-vitro vascular phantoms

5.1 Equivalences of artificial blood to human whole blood

5.1.1 Spectra of water mass and artificial lipid

The human whole blood contains mostly water, which is experimentally simulated by using the PBS buffer because it is facile to tune the PH value of the PBS buffer. This benefits later the preparation of the hemoglobin and the intralipid dilutions. A portion of water is prepared and measured, which shows a major absorption peak at the wavelength of 960nm. The water-equivalence is found in the spectral feature of the PBS buffer prepared, which shows an absorption peak at 960nm as well. Some minor absorption peaks in the visible range from 400 to 600nm are missing from the PBS spectra, whereby the real water gives low absorption peaks around the wavelength of 585nm (see Fig. 30(a))

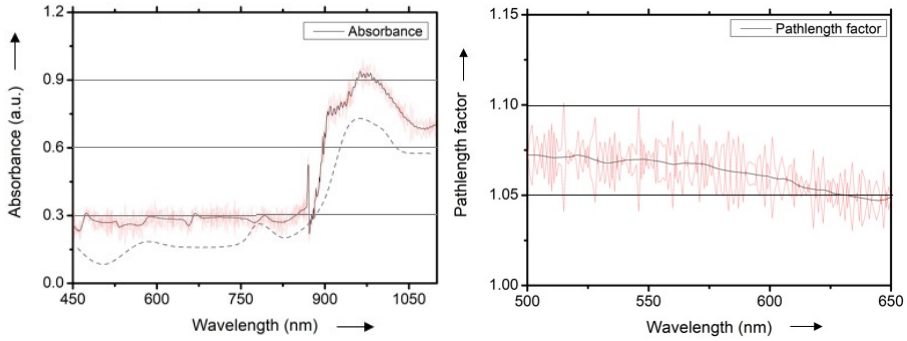

Figure 30: (a) The optical absorbance spectra and (b) the optical path length spectra of the PBS buffer are given, with black for the fitted spectra and red for the original data. The fitted absorbance spectrum of water (in gray dash line) is given as the reference.

To obtain the f_{PF} spectra of the pure PBS buffer, individual absorbance quantification is done to calculate the f_{PF} values at each single wavelength. The molar attenuation coefficient is first calculated from the observed transmission and reflectance. With the transmittance spectra and the reflectance spectra quantified through the Inverse Adding Doubling method, the molar attenuation coefficient spectra are computed. By dividing the absorbance spectrum by the molar attenuation spectrum, the f_{PF} spectrum of the PBS

buffer is plotted. At 537 and 577nm, the f_{PF} values of the PBS are 1.0336 and 1.0339 respectively (see Fig. 30(b)). In brief, the PBS is exhibiting high optical transparency and a spectral similarity to that of the real water.
Intralipid is used to simulate the lipid that exists in the human whole blood, in the form of its dilution in the PBS buffer, and its optical absorbance is quantified. The absorbance spectra of the intralipid dilution are given in Fig.31(a). In this case, a major absorption peak at 1000nm is found to match the spectral feature of the real human lipid (see Fig.31(c)).

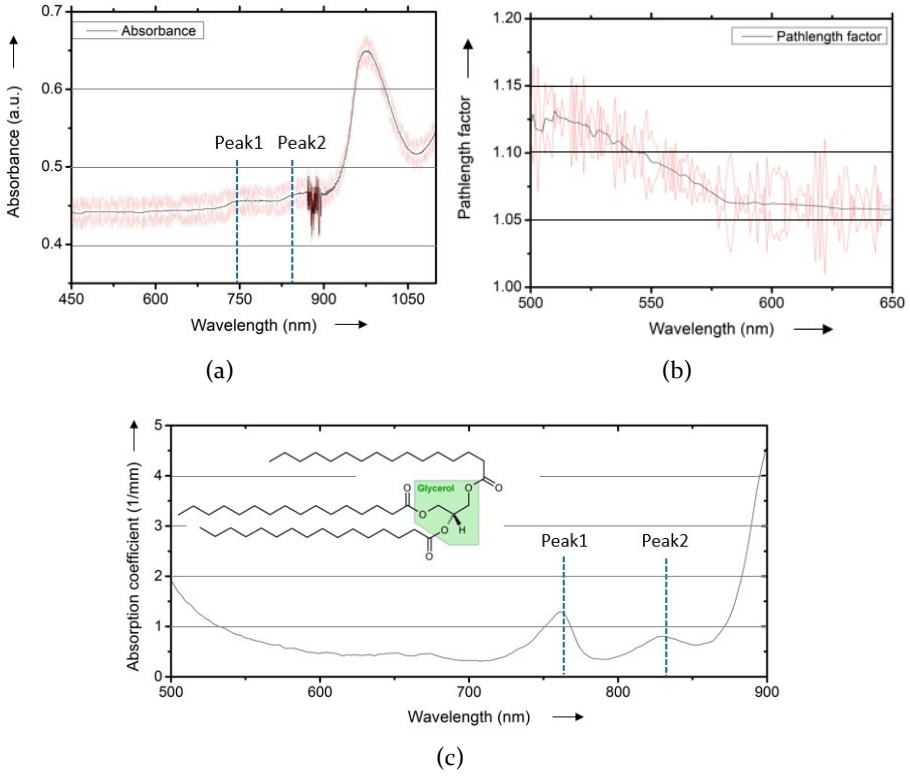

Figure 31: (a) The optical absorbance spectra, (b) the optical path length spectra of the prepared artificial intralipid dilution, and (c) the optical absorbance spectra of the real lipid (in the major existence of triacylglycerol compound) are given, with black for the fitted spectra and red for the original data.

An absorption peak is missing at 730nm, whereby the real lipid gives some minor absorption peaks around this wavelength. In the spectra of the prepared intralipid dilution, the absorption peak is truncated at 850nm, due to the fact, that the spectra show a major skip at the wavelength of 872nm

caused by the switch of the photon-detectors during the spectrophotometric measurement. The f_{PF} spectra of the intralipid dilution are plotted in the same way as it is done for the PBS buffer. The typical f_{PF} spectrum of the intralipid dilution shows a linear descent against the wavelength from 500 to 600nm, where the f_{PF} values of 1.113 and 1.0026 are given at 537 and 577nm respectively, all with a standard deviation of $\pm$ 0.0737 (see Fig.31(b)).

5.1.2 Spectra of artificial hemoglobin dilutions

By inserting the abovementioned intralipid dilution into the oxy- and deoxygenated hemoglobin dilutions, the blood dilutions are made to simulate the real whole blood in the oxy- and deoxygenated status. The oxygenation status and the optical spectra of the artificial hemoglobin dilutions should remain steady throughout the experimental procedure of the diffuse optical measurement. In this case, time stability of 30 min is expected regarding the absorbance spectra of the oxy- and deoxygenated hemoglobin dilutions prepared in different concentrations from 5 to 20 g/L. In Fig. 32(a), the absorbance spectra of the 20 g/L deoxygenated hemoglobin are shown at time intervals from 0 min to 30 min. The spectral feature of the deoxyhemoglobin dilution at this concentration is quite homogeneous and similar to that of the real deoxygenated blood, by which an absorption peak at 550nm is found (refer to Fig. 13 for the spectra of the real whole blood). The oxygenated hemoglobin dilution is giving absorption peaks at 532 and 573nm, namely, the α and β peaks (see Fig. 32(b)).

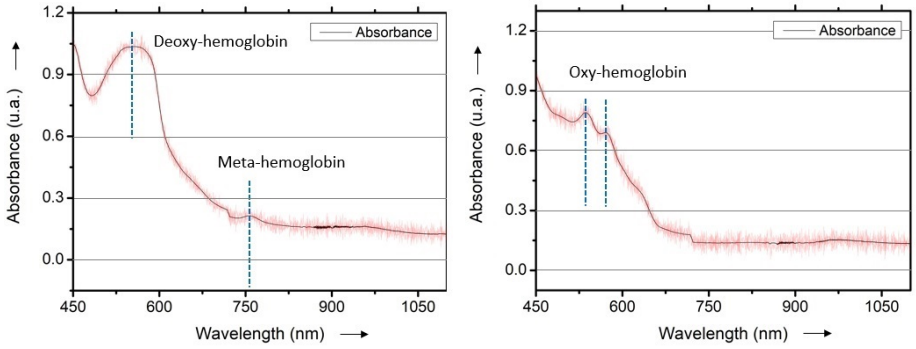

Figure 32: The absorbance spectra of (a) the deoxygenated hemoglobin and (b) the oxygenated hemoglobin against the wavelength are given, with black for the fitted spectra and red for the original data from the time frame up to 30 min.

The absorbance spectra of the deoxyhemoglobin dilution at a lower concentration (i. e. 3 g/L) show a smooth ascension to the peak, which is a consequence of the congruous deoxygenation of the hemoglobin dilution. For the high concentration hemoglobin dilution, the stability of the optical spectra (at 20 g/L) at different time courses is proved from the overlapping of the spectra. A minor change of 4 % in the optical absorbance spectra from all time frames (in arbitrary unit) confirms the fact, that the spectral feature is steady within 20 min and can substitute the real human whole blood as the inclusion in the in-vitro microphysiological vascular phantom.
A minor absorbance peak at 690nm, for both oxygenated and deoxygenated hemoglobin, is found to represent the retain of the methehemoglobin component. For the human whole blood in all concentrations, this retained portion of methehemoglobin cannot bind oxygen, and its existence can be caused by the autooxidation during the preparation of the hemoglobin dilution within its lyophilization, or so-called oxyhemoglobin dissociation. The hemoglobin's oxygen binding ability is inversely cognate to the acidity of the mass dilution and to the concentration of carbon dioxide. Since carbon dioxide reacts with water to compose carbonic acid, an incrementation in CO_2 results in a decrementation in the blood pH value. This brings the effect that the hemoglobin proteins relinquish their load of oxygen. In this case, the hemoglobin binds less O_2. A reduction in the total binding capacity of the hemoglobin (to O_2) against the reduced PH values is called the Root-effect. This means, the binding affinity of the hemoglobin to O_2 is optimized under a relatively high PH value.
In figure 33(a) and (b), the optical path length factors of the oxygenated and deoxygenated dilutions at the concentration of 10 g/L are shown. Like the case for the intralipid dilution and the PBS buffer, the optical path length factor of the corresponding hemoglobin sample is calculated from the absorbance/reflectance data. The f_{PF} values of the oxygenated hemoglobin dilution at 537 and 577nm are found to be 1.27 and 1.32 respectively. The f_{PF} values of the deoxygenated hemoglobin dilution at 537 nm and 577nm are 1.18 and 1.23 respectively. The spectral feature of the optical path length factor and its wavelength dependency match the results from other research works on the real human whole blood[47, 48]. This proves again the equivalence of the artificial hemoglobin dilutions to the real human whole blood, regardless of the difference in the concentration. For both oxygenated and deoxygenated hemoglobin dilutions, the f_{PF} values at 10 g/L are lower than those of 3 g/L. Also, the absorbance spectra and the f_{PF} spectra for the high concentration hemoglobin are not as smooth as those of the low concentration ones, when

the concentration of the artificial hemoglobin dilution increases over 5 g/L. This could emanate from the low signal-to-noise ratio of the spectrophotometer detector when measuring highly absorbing samples.

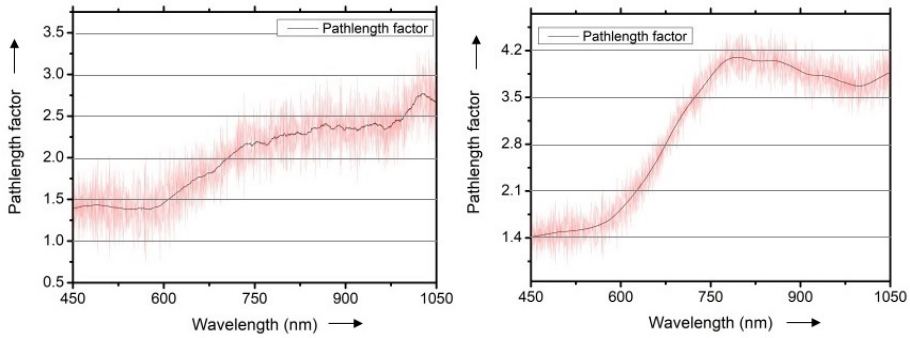

(a) (b)

Figure 33: The path length factor spectra of (a) the artificial oxygenated hemoglobin and (b) the deoxygenated hemoglobin at the concentration of 10 g/L against the wavelength are given, with black for the fitted spectra and red for the original data.

The concentration dependency of the optical path length factor of the prepared hemoglobin dilutions is plotted (see Tbl. 5). The average values are descending with the hemoglobin concentration. The optical path length factors of the hemoglobin dilution, at both wavelengths of 537 and 577nm, are inversely proportional to the concentration in the power index of about -1. Based on this, it is confirmed that the f_{PF} of the prepared hemoglobin dilution is not only dependent on the geometry of the illumination-detection pair adopted in the optical measurement, but also dependent on the concentration of the hemoglobin dilution itself. The correlation between the optical path length factors of the oxy- and deoxygenated hemoglobin dilutions within a reflection mode illumination-detection pair (in the diffuse optics) will be investigated later again during the phantom validations and should show a similar dependency on the concentration.
Besides, the optical cross-talk brought by the system configuration of the used spectrophotometer and the attached integration sphere should be mentioned. The μ_a of the pure blood sample can be 5 to 6 times higher than that of e. g. the skin extracellular matrix (with the same optical thickness) because of its rich blood content. Optical signals through the blood sample are extraordinarily low, and this brings a low signal-to-noise ratio. To address this, an integration sphere with an appropriate diameter is needed to engender

Table 5: The f_{PF} values of the oxygenated and deoxygenated hemoglobin dilutions at the concentration of 2, 5, and 20 g/L are listed to indicate their dependencies on the hemoglobin concentration.

Concen	Oxy2	Oxy5	Oxy20	Deoxy2	Deoxy5	Deoxy20
537nm n=3	1.98	1.32	1.11	2.41	1.47	1.22
537nm n=5	1.95	1.34	1.13	2.38	1.49	1.19
537nm n=10	1.92	1.32	1.15	2.40	1.48	1.21
577nm n=3	2.03	1.35	1.17	2.52	1.53	1.30
577nm n=5	2.07	1.36	1.16	2.55	1.55	1.32
537nm n=10	2.08	1.34	1.18	2.56	1.56	1.34

a better light collection and better light uniformity at the detector port. On one side, a smaller diameter sphere engenders higher throughput of the light beam reaching the detector, and brings resultantly smoother spectra with less noise. On the other side, a bigger sphere improves the light uniformity. To make a balance, an integration sphere with 15cm diameter is made and installed to the integration sphere.
As a short summarization for the optical characterization of the artificial hemoglobin dilutions, it is found that the minor existence of the methehemoglobin. Although the amount of them can be ignored, it would be preferred to oxygenate the hemoglobin with pure oxygen gas instead of air. It is also noticed that the deoxygenation is not impeccably adequate at a high concentration > 20 g/L, but still sufficient to simulate the real deoxygenated human whole blood. For a higher concentration up to 100 g/L, it would be suggested to take the real human blood from the healthy human volunteers. Despite these, the artificial hemoglobin dilutions are equivalent to the real human whole blood in the light-blood-interaction.

5.2 Turbid optofluidic vascular phantoms to mimic turbid skin tissue

5.2.1 OCT reconstruction of turbid optofluidic phantoms

A prototype optofluidic in-vitro microphysiological vascular phantom containing the in-/outlet and 4 separate rows of hollow microchannels is prepared and shown (finished sample see Fig. 34(a) and (b), schematic and photo see Fig. 34(c)). The diameter and the depth of the microchannels are measured separately on the finished optofluidic phantom by using an SD-OCT (Telesto-II-SP1, Thorlabs GmbH, Germany).

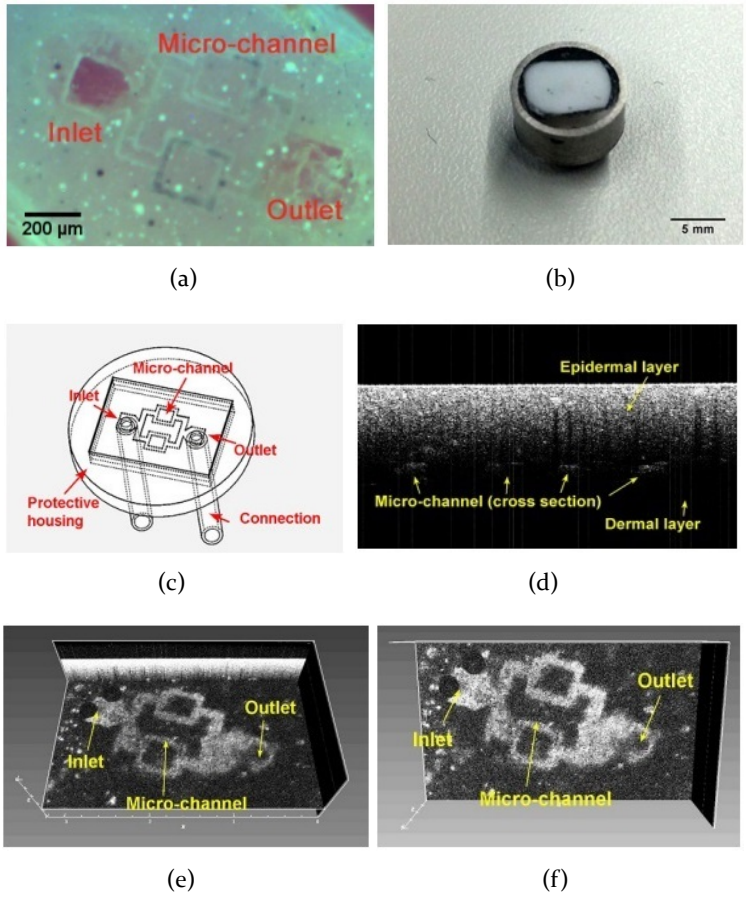

Figure 34: (a) Photo of the microchannels in the phantom with one transparent layer, (b) photo of the phantom with two scattering layers, (c) schematic of the generated optofluidic structure, (d) OCT B-Scan image of the two-layer geometry, (e) OCT top view of the generated optofluidic structure, and (f) OCT C-Scan 3D volume view of the generated optofluidic structure are shown[P1].

Figure 34(d) shows the cross-section of the phantom, where a clear view of the two-layer-geometry is displayed. The flat flecks represent the cross-section of the generated microchannels. As shown in these images, the inlet and outlet mimic respectively the arteries and veins, while the microchannels mimic the microvasculature. In order to check the vessel geometry uniformity more directly, the OCT is used for a 3D reconstruction (see Fig. 34(e) and (f)). The measured value of the microchannel width is 52μm on average. Overall,

the reconstructed optofluidic structure matches the original intention of the optofluidic design given in Fig. 20 in the shape and dimension.

5.2.2 Tunability in optical properties of optofluidic matrices

The phantom optical properties are presented in the μ_a against μ_s' of the PU matrices from different optofluidic phantom slabs. The paradigm of the μ_a and μ_s' are first attained from the ex-vivo skin slabs at the wavelengths of 500, 600, 700nm, and 900nm [16, 17, 18]. The results are seen in Fig. 35.

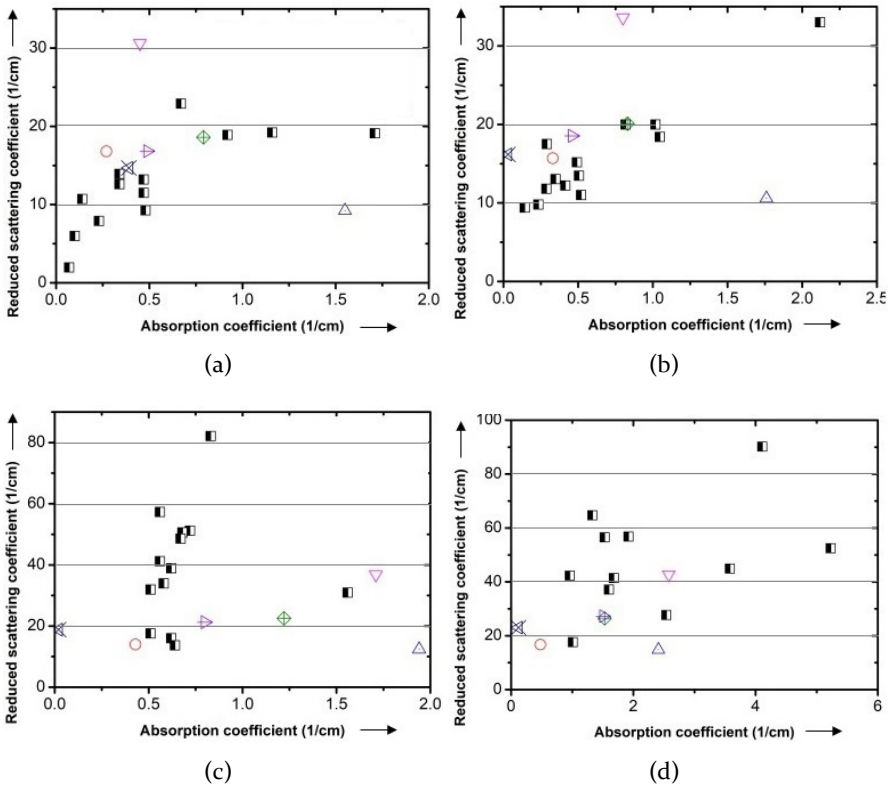

Figure 35: The optical properties of the phantom matrices at the wavelengths of (a) 500, (b) 600, (c) 700, (d) 900nm are plotted[S1]. The measured values are displayed in black dots, and the reference values representing the ex-vivo skin optical parameters are plotted in colored dots from the established literature [16, 17, 18].

It is expected to find a significant similarity within a comparison of the optical properties of the optofluidic phantom matrices to those of the ex-vivo human cutis. Whether the measured μ_a and μ_s' values could cover the reference va-

lues is the key question. The measured values are displayed in black dots. The paradigm zone concludes the optical properties of the real ex-vivo caucasian skin. At the wavelength of 600 nm, the μ_a of the PU slab gives a variance from 0.1 to 1.91 mm^{-1}. This range covers the paradigm from the real tissue, which gives a variance from 0.23 to 1.61 mm^{-1}. The $\mu_{s'}$ values show the same coverage. Similar coverage can be found at 700 and 1000nm, where the sampling zone of the μ_a and $\mu_{s'}$ overlaps with the paradigm zone (see Fig. 35). An exception can be found at 500nm, at which the sampling zone does not cover the paradigm zone (see Fig. 35(a)). This is due to the fact that the reference values are mostly attained from the blood perfused tissue as reported. The ex-vivo tissue sample contains residual blood in the ECM, which induces an increasing absorption at 500nm compared to that of the PU phantom matrices with no blood fraction. In brief, the optical turbidities of the optofluidic phantom matrices are equivalent to the optical turbidities of the ex-vivo skin tissue.
During the Embedding-and-Etching fabrication process, $NaHCO_3$ is added and dispersed into the water-based electrolyte during the phantom fabrication to prevent $CuCl_2$ from condensing. A side effect by doing this is that continuous chemical reaction occurs at the solid-liquid (electrolyte-PU) interface and changes the optical properties of the PU surface. To characterize the possible changes in the optical properties, the optical parameters of the phantom matrices are investigated before and after the PU slabs are attached to the electrolysis for 96 hours (see Fig. 36). PU slabs with different amount of TiO_2 and india ink are prepared into 200μm slabs for this study. Figure 36 summarizes the attenuation rate in the *total transmittance* T_t, the *diffuse transmittance* T_d, the *absorbance* A_b, and the *diffuse reflectance* R_d before and after etching. The Z-axis indicates the projection of the normalized values. The normalized A_b, T_d, and T_t values do not change with the etching progress. The registered values are around 1 in their correlation with the optical parameters μ_a and μ_s'. The standard deviations of these values do not exceed $\pm$ 5 %. The R_d values alter more after the etching and range between 0.89 and 1.12. This change is mostly caused by the wetting of the PU slab surface during the Embedding-and-Etching[P2].

5.3 Elastofluidic microphysiological phantoms to mimic soft skin tissue

5.3.1 OCT reconstruction of turbid elastofluidic phantoms

Despite the similarity of the optofluidic phantoms to the real skin in their optical turbidity, the optofluidic phantoms do not reflect all in-vitro features

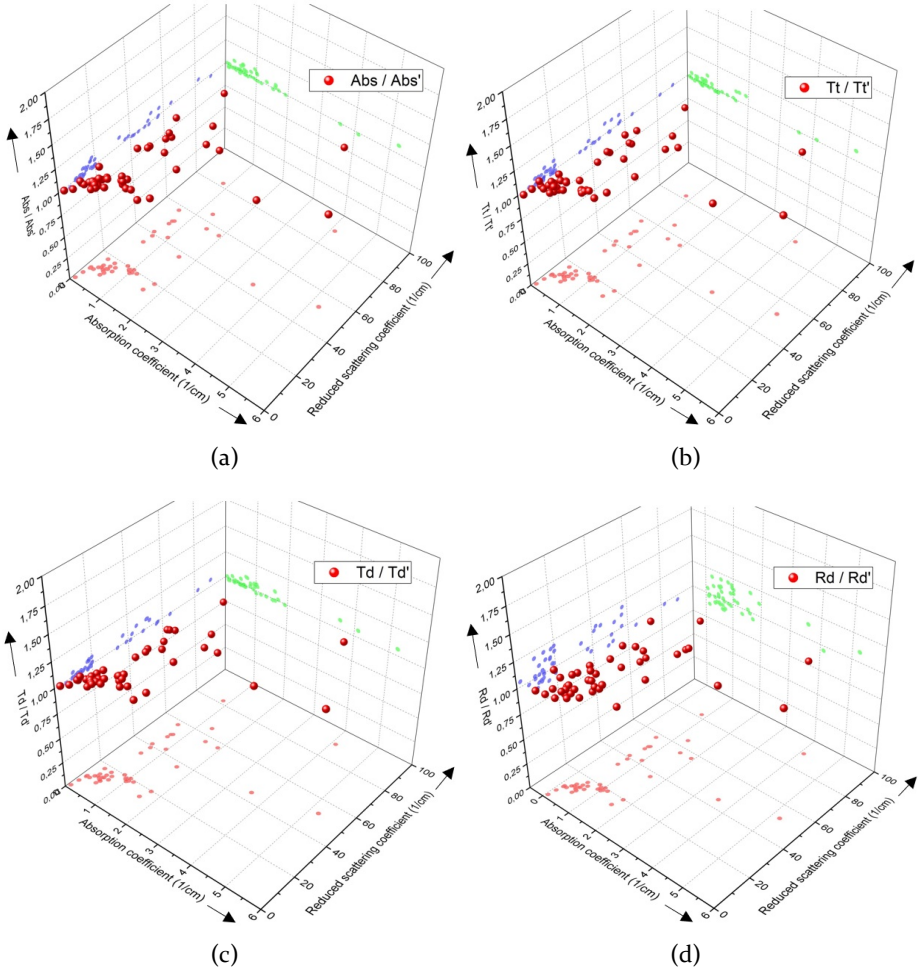

Figure 36: The optical properties of the PU slabs before and after etching are shown through the 3D scatter plot of (a) the absorbance, (b) the total transmittance, (c) the diffuse transmittance, and (d) the diffuse reflectance in the Z-axis against the μ_a and μ_s' in the XY-axis[P2].

of the real skin tissue for more complicated experiments. For instance, the light propagation shifts should be investigated at the contact site between the contact-based optical biopsies (typically the transducer-based PAT and the diffuse optics) and the soft phantom surface. For this, using soft elastomer-based matrix materials to fabricate more sophisticated in-vitro phantoms is essential. In figure.37, a prototype elastofluidic in-vitro microphysiological

vascular phantom with a minimum amount of scatterers in the superstrate is demonstrated to highlight the layout of the elastofluidic structure. Figure 37 (b) and (c) demonstrate the top-views of the elastofluidic channels and the resolution targets. It is expected to read 200μm in the channel width for the hi-flow speed and the mid-flow speed channels and 100μm for the diffusion channel. This variance in the microchannel dimension allows the manipulation of the flow dynamics when they are perfused with low dynamic viscosity (< 0.001 Pa.s at 23°C) liquid.

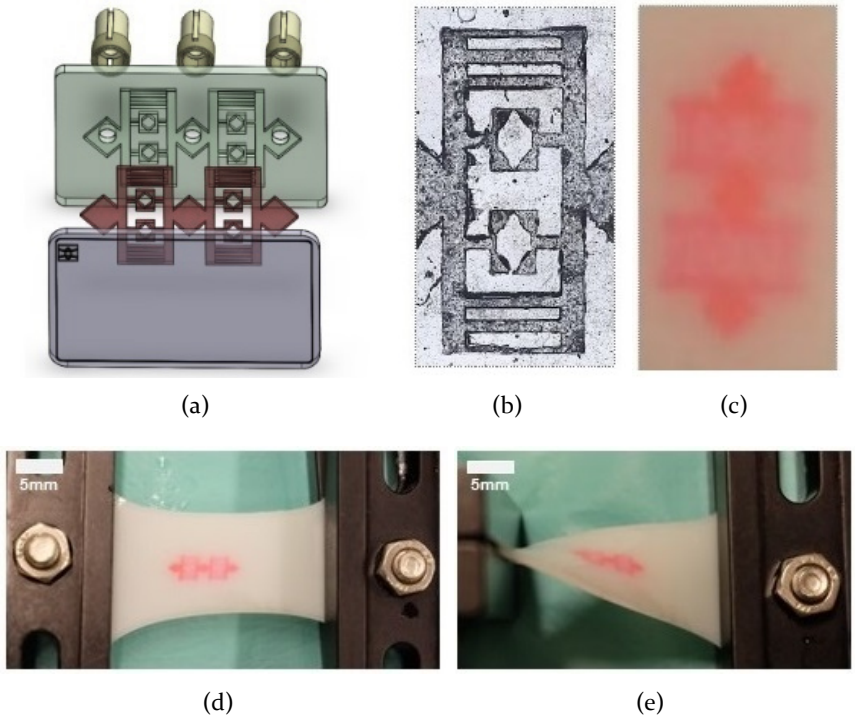

Figure 37: (a) Schematic of the elastofluidic phantom design is shown. (b) LSM picture of the generated fluidics structure, (c) photographic top view of the generated fluidic structure in the demonstration prototype with semi-transparent PVCp matrices are given. The elastofluidic phantoms under (d) stretch and (e) twist are demonstrated.

All mentioned geometries are measured again with the help of a *Laser Scanning Microscope* (LSM) (LEXT OLS4000, Olympas co., Japan). As the result of the LSM study, of which the phantom superstrate is peeled-off, a sharper picture is given without any optical disruption from the light scattering in the phantom matrices (see Fig.37). Regarding the changes in the surface tension

of the PVCp material during its polymerization, the cross-sectional widths of the channels are around 207μm and 93μm respectively. The measured thickness of the PVCp superstrate is around 213μm, which is slightly overriding the designed value of 200μm.

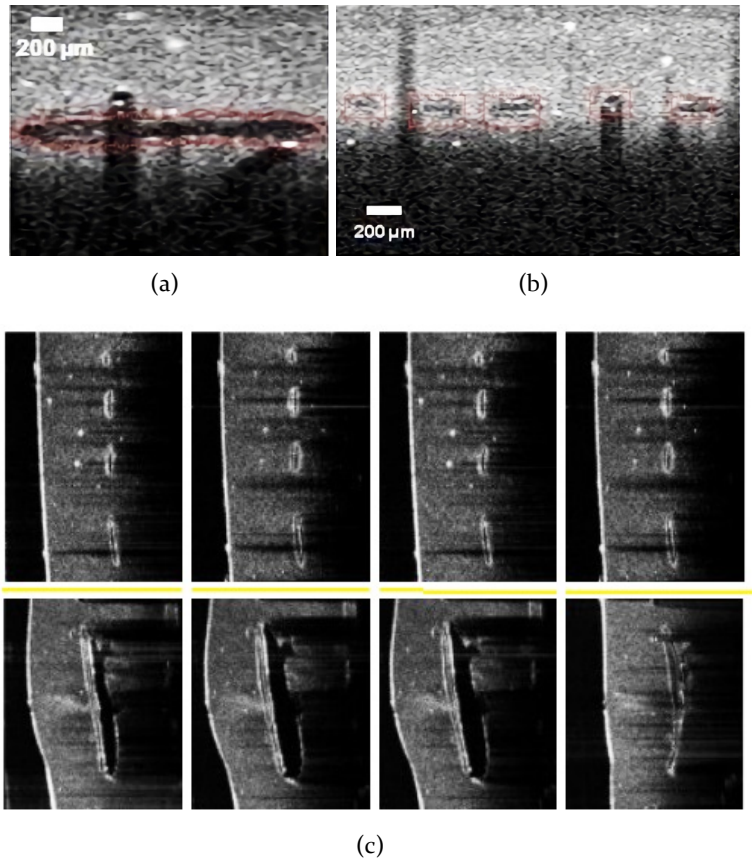

Figure 38: OCT B-Scans of (a) the inlet and (b) the microchannels, including the hi-flow speed channel, the mid-flow speed channel, the diffusion channel, and the cross-section of the resolution target are shown. (c) OCT images of the microchannels and the inlets are given to show their expand under 6-bar liquid flush in the time courses of 0, 0.5, 1 and 1.5s.

The resolution targets show 4 triangular quarters surrounding a rhombus shape in the center (see Fig.37(b)). A minimum dimension of the elastofluidic structure is found at the gap between the rhombus diagonal corner and the square, where 21μm is registered for the gap size. The cross-sectional views of the microchannels and the inlets are also given in the OCT 2D B-Scans

(see Fig. 38(a) and (b)). Same specifications are measured and show unity in the cross-sectional width obtained in the top-views. Under the depress liquid pressure given by the membrane pump (up to 6 bar), the elastic PVCp matrices start to spread out horizontally (see Fig.38(b)). This simulates the vessel expansion under the flush of blood from the systolation. Overall, the reconstructed elastofluidic structure shows an agreement to the initial drawing given in Fig. 24 in its shape and dimension.

5.3.2 Tunability in optical properties of elastofluidic matrices

The optical properties of the elastofluidic phantom matrices are first compared to those of the optofluidic phantom matrices (see Fig. 39). As the result, the μ_a and $\mu_{s'}$ approach each other in the diagram. This means, the switch in the material selection of the phantom matrices from the castable polyurethane to the elastomer PVCp does not bring severe changes in the optical properties, although these two materials show slight differences in their refractive index N at all wavelengths.

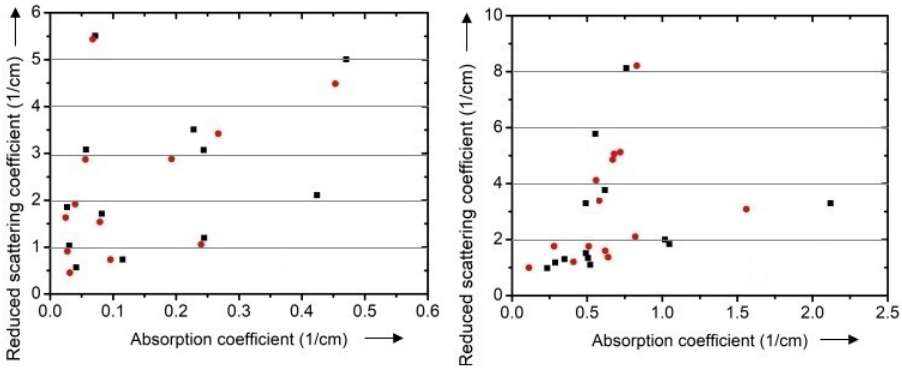

(a) (b)

Figure 39: The match between the optofluidic phantom matrices (in black dots) and the elastofluidic phantom matrices (in red dots) in their absorption coefficient and reduced scattering coefficient at the wavelengths of (a) 630 nm and (b) 700 nm is given as the showcase.

It is also expected to find a significant similarity between the optical properties of the PVCp matrices and those of the ex-vivo tissue. The results are plotted in the scale-diagrams of the μ_s' against μ_a (see Fig. 40).
The measured values are displayed in the circled scale diagram due to the minor inhomogeneity of the scatterers/absorbers purposefully made (claimed in the later subsection). The paradigm of the μ_a and $\mu_{s'}$ is attained from the

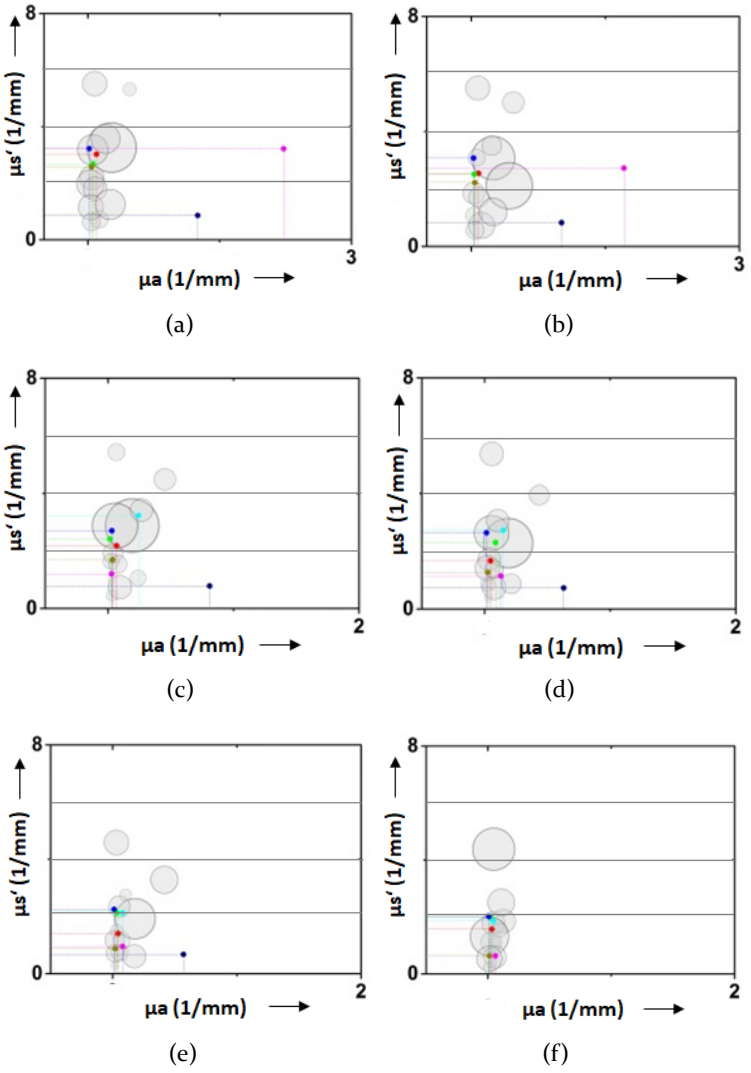

Figure 40: The optical properties of the prepared PVCp slabs and the comparison to those of reference values plotted in colored dots from the literature [16, 17, 18] are shown. The optical properties of the PVCp matrices at the wavelengths of (a) 500, (b) 540, (c) 570, (d) 630, (e) 700, (f) 800nm are given in circled scale diagram to represent their range in the μ_a and μ_s' values.

ex-vivo human tissue and shown colored dots. As shown in the diagram for 500nm (see Fig.40), the min. absorption coefficient of the PVCp slab is found at 0.06 mm^{-1}, which represents the caucasian epidermis. The maximum value

is found at 1.7 mm^{-1} and represents the skin type with dark color tone. This interval mostly covers the absorption coefficients of the ex-vivo skin tissue of all color tones, ranging from 0.05 to 1.7 mm^{-1}. Likewise, the reduced scattering coefficients of the PVCp slabs overlap those of the ex-vivo tissue. During the fabrication of the elastofluidic phantoms, the PVCp surface hydrates with H_2O molecules, and this causes the opacification of the plastisol matrix. Some elastofluidic phantoms form a milky appearance after 30 min reaction with water, which can turn transparent in 2 hours.

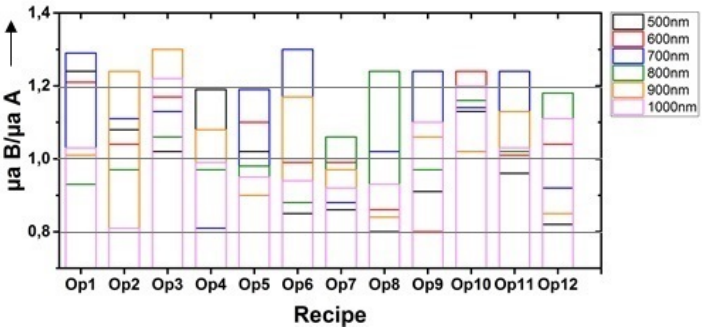

(a)

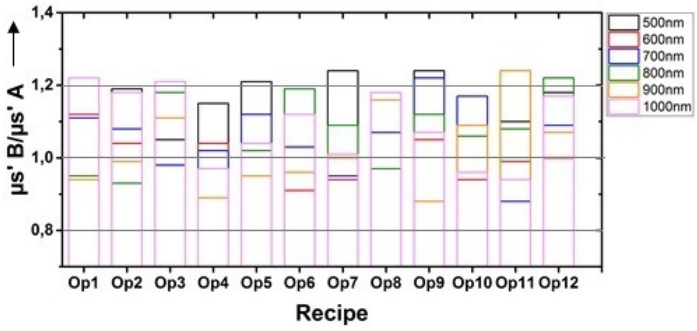

(b)

Figure 41: The attenuation in (a) the absorption coefficient and (b) the reduced scattering coefficient of the PVCp slabs are given for before and after the opacification.

To indicate the possible changes in the matrices' optical properties before and after the degrading procedure, the normalized values $\mu_{abefore}/\mu_{aafter}$ and $\mu_{sbefore'}/\mu_{safter'}$ are measured (see Fig. 41). The normalized values are supposed to be 1 as if the changes in the optical properties did not occur. In principle, the registered values are from 0.85 to 1.25. This change may also be caused by the angular resolution of the photo-detectors used in the

spectrophotometer, the limited size of the integration sphere, and the light oscillations. After reducing the systematic error, the normalized values of the optical coefficients are around 1 with a ± 1.5 - 1.7% within 13 times repetitions. By evaluating the normalized μ_a and $\mu_{s'}$ values, it can be verified that the fabrication procedure does not reveal any significant alteration in the optical properties of the PVCp matrices.

5.3.3 Optical equivalences to in-vivo human skin

After the comparison of the elastofluidic phantom turbidities to the ex-vivo skin and the optofluidic phantom within the spectrophotometric measurements, the μ_a and $\mu_s^{'}$ of the elastofluidic phantom matrices are measured by the diffuse optical probe and compared to the in-vivo results measured from the chose volunteers to find the optical equivalences. The results, as well as the estimated values from Equ.3 and Equ.5, are listed in Tbl. 6. At the wavelength of 537nm, the female forehead (n = 13) gives a μ_a of 0.15 mm^{-1} on average with a standard deviation of ± 0.012 mm^{-1}. The $\mu_s^{'}$ is 3.7 mm^{-1} on average with a standard deviation of ± 0.32 mm^{-1}. The μ_a and $\mu_s^{'}$ of the male forehead are about 7 - 10 % higher than those of the female volunteer, even when they have rather the same skin color tone. The reason is that males mostly have a thicker stratum corneum layer than females. When the incident light hits the stratum corneum layer, the light is first scattered and delivered along the flattened cells in the stratum corneum layer, thus inducing more backward scattering.

Table 6: The optical parameters of the human skin at different body parts and the optical parameters of the elastofluidic phantom matrices are given and compared.

	mu_a 537	$mu_s^{'}$ 537	mu_a 577	$mu_s^{'}$ 577
M. fhead	0.15 ± 0.012	3.7 ± 0.32	0.14 ± 0.008	3.8 ± 0.26
F. fhead	0.12 ± 0.009	2.9 ± 0.28	0.13 ± 0.013	3.2 ± 0.21
M. arm	0.14 ± 0.015	4.2 ± 0.27	0.12 ± 0.011	4.1 ± 0.29
F. arm	0.11 ± 0.011	4.0 ± 0.31	0.09 ± 0.009	3.9 ± 0.22
M. knee	0.17 ± 0.014	5.6 ± 0.25	0.15 ± 0.01	5.8 ±0.28
F. knee	0.15 ± 0.013	4.8 ± 0.28	0.13 ± 0.015	5.2 ±0.26
Phantom OP6	0.15-0.2	3.5-4.1	0.14-0.19	2.8-4.9
Phantom OP8	0.17-0.23	4.7-5.5	0.016-0.22	4.3-5.2
Esti.	0.13-0.45	1.7-6.8	0.12-0.39	1.6-5.7

The optical properties of the skin on the arm and the knees (n = 13) are also measured, where the μ_a in the range of 0.12-0.17 mm^{-1} is found. The $\mu_s^{'}$ varies

from 4 to 6 mm^{-1}. The reduced scattering coefficient of the skin on the human knee is virtually 1.5 times higher than that of the forehead. The absorption coefficient of the skin on the knee is marginally higher as well. This is due to the fact that long-term friction between the skin surface and the textile might cause the skin pigmentation deposition. It also makes the stratum corneum layer thicker. This phenomenon is named as the skin discoloration. The estimation from the empirical equation as mentioned in the optical model gives a very slight over-estimation of 5 % in the μ_a and 4% in the μ_s'. It is found that the phantom OP6 matches the female volunteer in the values of μ_a and μ_s', while the skin optical turbidites of the male volunteer is replicated in the phantom OP8. To this point, the measured optical properties of the human skin in-vivo are close to those of the elastofluidic phantoms OP6/OP8 and the calculation from the optical model. The equivalences between the in-vitro microphysiological vascular phantoms and the in-vivo skin in their optical turbidities are approved.

5.3.4 Tunability in mechanical/acoustical properties of elastofluidic matrices

As for rubber-type materials like the PVCp, the random molecular conformations change with the material deformation and form the mechanical elasticity. Regarding the mechanical similarity of the PVCp to the human skin cutis, it is expected to find a tissue-equivalence when comparing the Young's moduli of the prepared PVCp slabs to the ex-vivo tissue. Figure 42(a) shows the Young's moduli of the PVCp slabs inserted with different portions of softener, while the same parameters of the ex-vivo tissue are shown in Fig.42(b). The Young's moduli of the PVCp slabs range from a minimum of 0.28 MPa over an average of 0.57 MPa to a maximum of 0.81 MPa, rather linearly decrease with the softener concentration. Compared to the results from the ex-vivo tissue, which range between 0.5 and 0.8 MPa, the PVCp has a wider band in the mechanical elasticity.

One remarkable note during the experiments is that the Young's moduli of the PVCp slabs remain invariant with time changing, or known as the phenomenon of mechanical creep. The stress-and-strain relationship of living tissues is non-linear and is slightly different from the mechanical characteristics of the PVCp slabs. However, reflecting any creep feature in the PVCp matrices of the elastofluidic phantom is not considered in the framework of this project. Optimized mechanical compliance, in terms of the stretchability of the PVCp super-/substrate, is essential to keep the phantom matrix resistant to any deformation during the use of the elastofluidic phantom. The

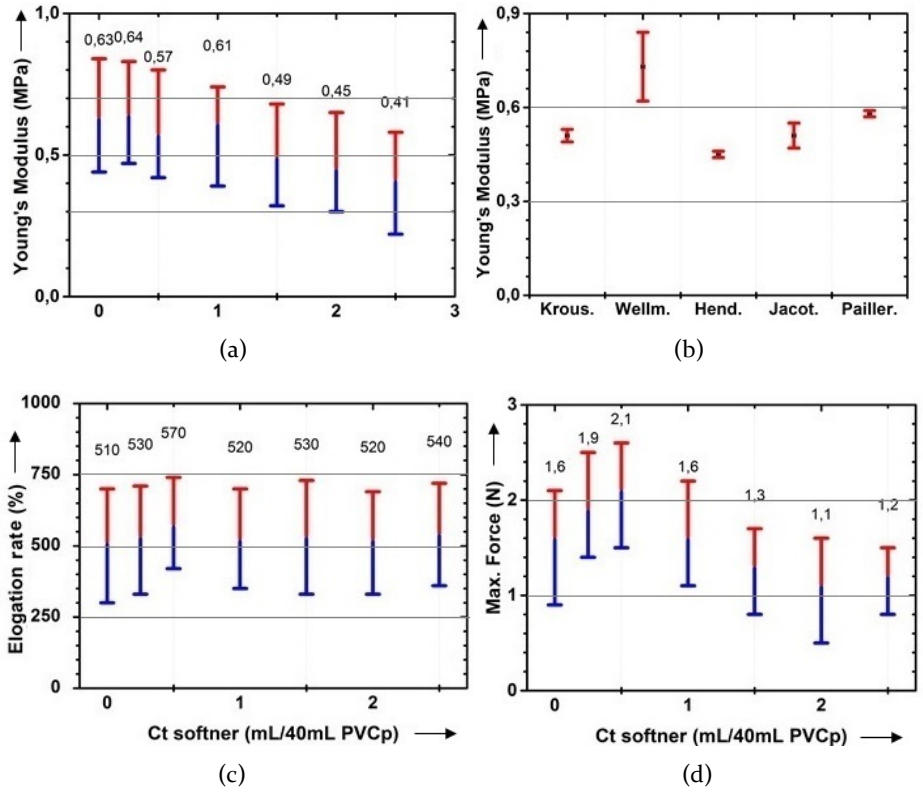

Figure 42: (a) The Young's moduli, (c) the elongation rate, and (d) the maximum force during the mechanical test on the PVCp slabs are shown. (b) The Young's moduli of different tissue types are given as the reference.

stretchability is evaluated through the elongation rate ε. An elongation of around 300% in minimum over 500 % on average to 700% in maximum is reported, almost 10 times higher than that of any tissue type (see Fig.42(c)). Combined with the max. force that the PVCp can withstand (see Fig.42(d)), the PVCp matrices exhibit a premium resistance to the fracture when the elastofluidic structure is undertaking physical loads or stress induced by the liquid flush.

The speed of sound in the real soft tissue rates a mean value of 1540 m/s. Moreover, the variation in the speed of sound around this mean value is rather small, on the order of 7%[49] depending on the tissue type. The speed of sound of 1350 to 1500 m/s are measured from the PVCp matrices. Unlike the real tissue, the anisotropy of the acoustical properties cannot be clearly found

in the PVCp material compared to that of tissue. In fact, the sound wave can be more dominantly propagating along the fiber/layer morphology. Here, it is suggested to improve the degree of crystallinity by e. g. inject moulding during the preparation of the PVCp sub-/superstrate if the researchers aim to achieve the acoustic anisotropy in certain degrees.

5.3.5 Heterogeneity in chromophores' distribution in elastofluidic phantoms

In-vivo studies require more considerations about the heterogeneity of the chromospheres' distribution in the skin. The extracellular matrices of the skin epidermis and dermis are considered as a less homogeneous mixture of cells, RNA, acid, water, melanin, and some other fiberized cell bonds, compared to the opto-/elastofluidic phantoms prepared in-house[19]. Such problems have been met during the phantom validations of other biooptical approaches. As if the researchers implement the in-vivo experiments directly on the human volunteers without any forecast of the chromophores' heterogeneity from the phantom validations, they could not realize the erroneous results from the in-vivo experiments. In this study, the existence of the fibroblasts and the inhomogeneous spatial distribution of the major chromophores in the in-vivo human skin (see Fig. 43) should be replicated in the in-vitro phantom matrices.

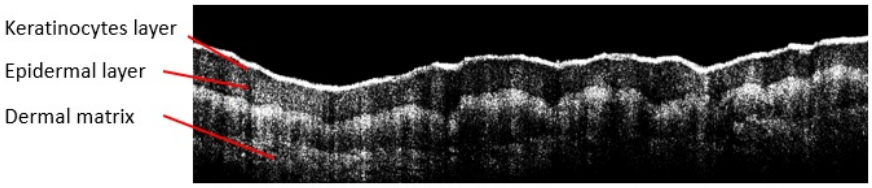

Figure 43: OCT B-scan of the in-vivo human skin is given to indicate the heterogeneous distribution of the light scattering chromophores in the epidermis and dermis.

The fibroblasts cause the anisotropy in the propagation of light along their fiberized structure. When light is incident perpendicular to the fibroblasts, backward scattering/reflectance becomes dominating. They block the incident light from propagating forward to reach the deeper extracellular matrices which are rich in blood diffusion. The elastofluidic in-vitro phantom models should reflect a certain heterogeneity of the major chromophores in the presence of different heterogeneities in the spatial distribution of the scatterers in the superstrate and substrate respectively. During the fabrica-

tion of the elastofluidic phantoms, an agglomeration of the inserted TiO_2 nano-spheres exists after the PVCp matrices are plasticized. In one sense, this enables the tuning in the homogeneity of the scatterers' distribution in the low viscous PVCp raw material (in its liquid form). Experimentally, an ultrasound bath in 37Hz pulse frequency (Elmasonic, Germany) is used to decouple the molecular attraction among the TiO_2 nano-spheres in the viscous PVCp raw liquid. The OCT B-scans of the scatterers' distribution are given in Fig. 44.

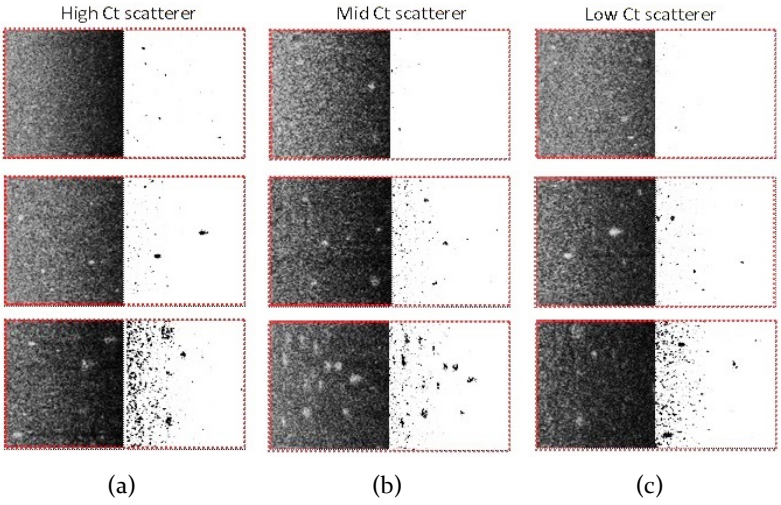

Figure 44: The original OCT B-Scan images of a low scattering PVCp slab with (a) 2 h sonification time, 30 min sonification time, and 10 min sonification time; (b) a middle scattering PVCp slab with 2 h sonification time, 30 min sonification time, and 10 min sonification time; (c) a high scattering PVCp slab with 2 h sonification time, 30 min sonification time, and 10 min sonification time, are given. The post-processed binary images (in white background) that threshold the scattering clusters from the OCT images are shown next to the corresponding OCT images.

Subsequently to check the outcome of this homogenization process, PVCp slabs with TiO_2 insertions in different concentrations from 0.2 (low scattering) over 0.5 (middle scattering) to 1 g/40mLPVCp (high scattering) are prepared and imaged by using the SD-OCT. The scatterers' homogeneity is evaluated from the OCT B-scan of the turbid PVCp matrices. The image post-processing is performed and given to all OCT images for before and after the homogenization. The 8-bits grayscale OCT raw images are de-speckled by filtering with the raw OCT images with high dB values to give binary images as the final results (see Fig. 44). By comparing among all binary images, it is

found that the speckling spots start to vanish over time along with the ultrasound bath duration, as the TiO_2 clustering is smashed and broken through the ultrasound pulses. Numerical quantification of the homogeneity is implemented on the binary OCT images (see Fig. 44) by measuring the size of the speckle representing the scatterer cluster. The maximum (A_{max}), as well as the average values A_{ave} of the cluster area (per slice of OCT image) are calculated and plotted against the ultrasound bath duration (see Fig.45(a) and (b)).

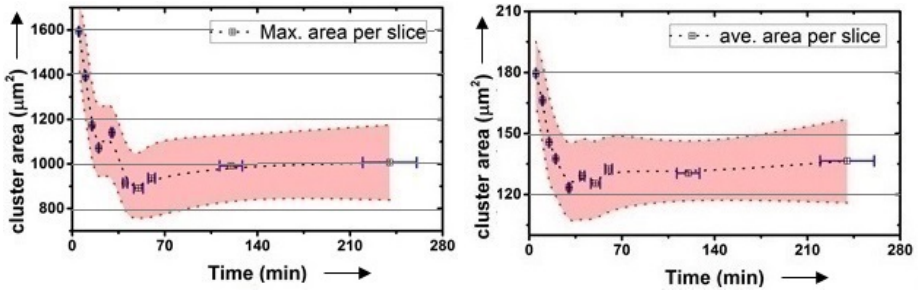

(a) (b)

Figure 45: The quantitative evaluation of the homogeneity of the scatterers in the PVCp matrices is shown. The size of the scatterer clusters per B-scan area is given in the values of (a) maximum and (b) average area per slice of PVCp slab.

As indicated, the A_{max} decreases from 1600 μm^2 (0 min sonification) to 650 μm^2 (30 min sonification), and A_{ave} from 180 μm^2 to 50 μm^2. The lowest values are found at 30 min sonification time. For this reason, it is suggested to perform a 30 min ultrasound bath for a perfect homogenization of the scatterers according to the researchers' needs. In the specific case of the elastofluidic phantom preparation for later the translational studies of the diffuse optical biopsy, a 15 min ultrasound bath is chosen to achieve a certain heterogeneity in the PVCp substrate to simulate the heterogeneous chromophores' distribution in the real skin dermis, while a 20 min ultrasound bath is done on the PVCp superstate to simulate the more homogeneous epidermis.

5.3.6 Delamination of elastofluidic sub-/superstrate

The delamination between the sub- and superstrate can affect the conformity rate of the elastofluidic phantom fabrication and its experimental uses. In this case, weak bonding between the sub- and superstrate leads to the delamination. This can result in the cross-contamination of fluids between the layers

or the disintegration of the two-layer-geometry. One class of components susceptible to the delamination is at the liquid depress pits, which consists of the in-/outlets and their over-going into the microchannels. When the induced strain in the PVCp matrices around the fluid flow exceeds the on-off strain, the PVCp matrices buckle, and the PVCp substrate deforms coherently. This might result in the opening of the microchannels in the elastofluidic structure, and the lamination at the site of these microchannels starts to crash continuously. To minimize the delamination, a modification method is investigated to better join the superstrate and substrate of the elastofluidic phantom (see Fig.46).

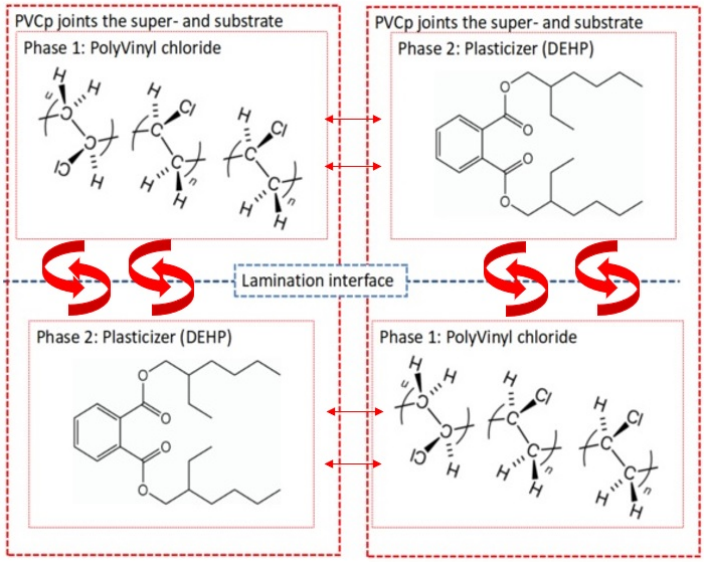

Figure 46: Schematic of the chemical partial diffusion of the PVC and the plasticizer (*Bis(2-Ethylhexyl) phthalate* (DEHP)) in the modified plasticization procedure is shown in the sketch. In the modified case, the PVC in the superstrate joints with the DEHP in the substrate to form strong bonds at the PVCp lamination interface.

In the modified process, the PVCp superstrate is directly cast onto the heated PVCp substrate at 343K. By doing this, the free PVC chains at the superstrate catch the plasticizer (*Bis(2-Ethylhexyl) phthalate* (DEHP) chains at the substrate to form a conjunction. The C-C bond between the monomers can be engaged at the lamination interface. Consequently, the semi-pregelized plastisol compounds at the interface between the super-/substrate can generate partial diffusion into each other to form into one single phase

To check the outcome, two elastofluidic phantoms are prepared and compared: one produced with the modified procedure, while the other one without any modification. A delaminated elastofluidic phantom is shown in Fig.46, This phantom is specially made and has a transparent superstrate to give a highlighted view of the lamination interface. In this delaminated phantom, the injected liquid flows out of the channel wall. The cross-contamination is found, and the fluidic structure is blurred (see Fig.46 (c) and (d)).

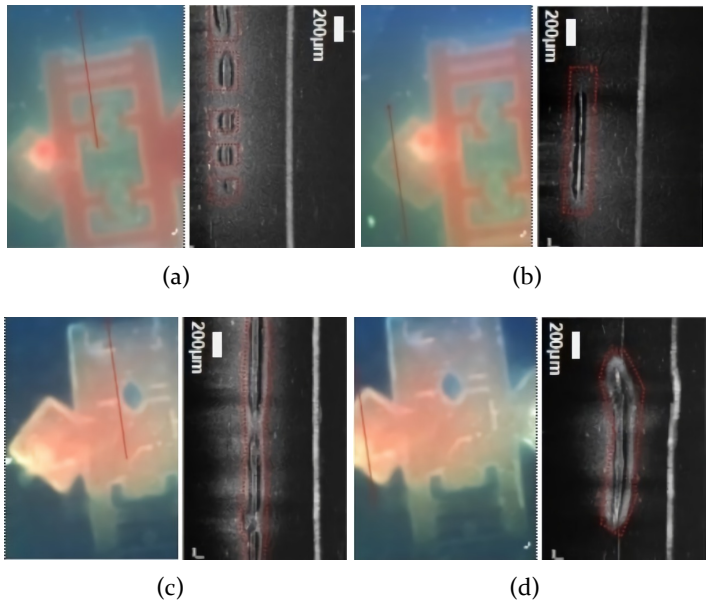

Figure 47: OCT B-scans and microscopic top-views of a laminated phantom (a) at the microchannels and (b) at the inlet are shown. Likewise, OCT B-scans and microscopic top-views of a delaminated phantom (c) at the microchannels and (d) at the inlet are shown.

To view the delamination at the depress pit more directly, OCT imaging is performed upon one of the elastofluidic phantoms in the regions that are depressed with the highest flow rate, namely, the inlet and the microchannels (see Fig.47). During the experiments, water is injected into the elastofluidic phantom with liquid pressure of 6 bar (actual flow rate of 10 mL/min), and the phantom is continuously flushed for 96 hours. In the case of the cross-contamination (see Fig.47(c) and (d)), the microchannels are joint into each other, and the upper boundary of the inlet starts to depart from the bottom layer when the phantom is flushed for 9 hours only. Oppositely in the case of a

perfectly laminated phantom as shown in Fig.47(a) and (b), the layers remain attached to each other with no cross-contamination occurs over time. After the modification in the PVCp fabrication is done, the elastofluidic phantom is sufficiently robust to withstand 96 hours continuous liquid flush with high liquid pressure up to 6 bar and high flow rate up to 10 mL/min. This means, the prepared elastofluidic in-vitro microphysiological vascular phantoms can guarantee safe uses during the phantom validations for the optical biopsies of all kinds. Within this given specification, the blood hydraulic at any level (pressure and flow rate) can be simulated in the elastofluidic in-vitro microphysiological phantom without any material failure.

5.3.7 Comparison to established in-vitro microphysiological vascular phantoms

The way of fabricating the opto-/elastofluidic in-vitro phantoms is unique. Unlike the conventional fabrication procedure for e. g. PDMS or PMMA microfluidics, there is no existing sealing/finishing steps after embossing the microfluidic structure. No facility (such as the UV irradiance facility) or specific matrix material is needed for the lamination. The lamination of the opto-/elastofluidic phantoms is not deteriorated throughout the entire fabrication procedure. This enables the use of a variety of matrix materials and the insertion of the optical scatterers/absorbers into the matrices. In Tbl.7, the prepared opto-/elastofluidic phantoms are compared with other established in-vitro microphysiological vascular phantoms.

Table 7: Comparison of the features provided by the established tissue-equivalent microfluidics/phantoms with the elastofluidic in-vitro microphysiological vascular phantom proposed in this work is given.

Feature/Group	Turbid	Layers	Perfuse	Size	Elas/Acou
Wang et al. [30]	Yes	Yes	No	No	No
Sollier et al. [28]	No	No	Yes	Yes	Limited
Dabrowski et al. [50]	Yes	No	Yes	No	No
Samuel et al. [51]	No	Yes	No	Yes	No
Lim et al. [8]	No	No	Yes	Yes	Limited
Tuchin et al. [29]	Yes	Yes	Yes	No	No
Bykov et al. [7]	Yes	Yes	Yes	No	No
Parthasarathy et al. [10]	Limit	Limit	Yes	Yes	No
Chen et al. [P1]	Yes	Yes	Yes	Yes	No
Chen et al. [P4]	Yes	No	Yes	Limit	No
This work	Yes	Yes	Yes	Yes	Yes

The principal features of the vascularized skin tissue are categorized as following: the tunability in the optical turbidity, the tunability in the mechanical elasticity/acoustic properties, the multiple-layered anatomy, the possibility of perfusing liquid into the phantom, and the micron-scale fluidic structure. As the conclusion, the prepared elastofluidic in-vitro microphysiological vascular phantom possesses all mentioned features and is the most skin-equivalent among all phantoms established in the state of the art.
With the help of the unique fabrication process, the opto-/elastofluidic in-vitro microphysiological vascular phantoms can be further tailored within a wide range to gain more physical/biological characteristics during the customization of the phantoms to match researchers' needs. This involves the following details about the requirement changes that need to be addressed. They include the matrix material selection (among *Thermoset Polyester* (TPE), *Polyurethane Methacrylate* (PUMA). *Norland Adhesive 81* (NOA81), aqueous suspension, gelatin, agar gel, acrylic, hydrogel, epoxy resin, silicone rubber, polyester, natural polymer etc.), the absorbers/scatterers selection (among lipids, polymer microspheres, Al_2O_3 particles, organic/inorganic dyes etc.), and the selection of other possible additives (such as glucose fluorophore, glass microspheres etc.). By doing this, more functions can be assigned to the in-vitro phantom models, including e. g. the chemiluminescent reaction of the matrices to drugs/drug delivery, the topography modification in changes of cell adsorption/adhesion at the microfluidic walls, and the definition in the to-be-mimicked tissue types (carcinoma-on-a-chip, retina-on-a-chip, lung-on-a-chip etc.).

6 Translational studies of diffuse optics

6.1 Lesion analysis on optofluidic in-vitro phantoms

6.1.1 Optical path length measurements on optofluidic phantoms

The region around the 'vascular structure' in the optofluidic phantom is scanned. As the result, an image with a field of view of 1 × 1mm is given to illustrate the planar top view over the vessel channel (see Fig.48). In the image with the scanning step size of 10μm, the projected image contains 100 × 100 pixels to include the absorbance spectra in each single pixel. The grayscale grades the absorbance from high caliber in dark to low caliber in white, with no spatial filtering or smoothing applied.

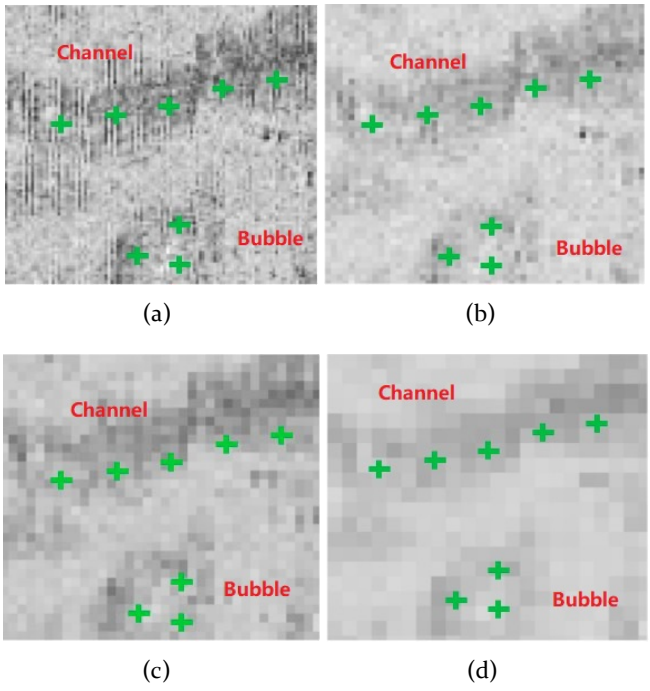

Figure 48: The reconstructed projection images of a single vessel embedded in the optofluidic phantom with the scanning step size of (a) 2, (b) 5, (c) 10, (d) 20μm are given.

Read from the image, a vessel channel horizontally perforating through the segmented regions is found with good contrast against the scattering back-

ground. Eminently, there is a dark spot denoting a higher absorbance than the scattering background in the image. This projection is caused by the liquid diffusion of the included hemoglobin dilution from the microchannel into the air bubble in the PU matrix, which is opened to the microchannel. This air bubble is coincidently a good target to test, whether the diffuse optical approach could capture the light attenuation from the micron-scale target within its illumination-detection pair. The outline of the dark spot is quite pellucidly given in the projection image with the scanning step size of 2, 5, and 10μm, while the projection image (see Fig. 48) enlarges this dark spot on the same position. With a scanning step length of 20μm, the reconstruction of the blood condensation is represented by only a few pixels, and the outline is not clear. It is suggested that the side length of the given FOV should be 50 times of the scanning step size to make micron-scale targets visible[P5].
After the initial tests on mapping the optofluidic pattern, the optical path length factors of the injected hemoglobin dilution are recovered from the registered spectra in the image pixels. The optical absorbance are obtained from 10 random sampling points in the projection image, which is regard as the 'vascular structure', and converted into the absolute f_{PFHbO2} and f_{PFRHb} values through the modified Beer-Lambert Law. To find the best optical sensitivity to the oxygenation status of the prepared hemoglobin dilutions during the diffuse optical measurement, wavelength selection is first decided. Two wavelengths of 537nm and 577nm around the isosbestic point of the hemoglobin spectra are first chose to achieve the highest differentiation rate in the absorbance of the oxy- and deoxygenated hemoglobin. This could also aid to yield the optical absorption from the pigmentations, such as the melanin in the skin/the inserted india ink in the phantom matrix. The concentration dependencies at 537 and 577nm are given.
For the oxygenated hemoglobin at 537nm, it shows an average f_{PFHbO2} value of 2.7 at 1 g/L hemoglobin concentration, with a deviation of $\pm$ 0.47. A descent of the average f_{PFHbO2} value to 2.07 at the concentration of 5 g/L is given. The deviation is getting more minuscule to $\pm$ 0.18. At the hemoglobin concentration of 20 g/L, the f_{PFHbO2} is approaching 1.33. For the oxygenated hemoglobin at 577nm, the deoxygenated hemoglobin at 537 and 577nm, the optical path length factors are given in Fig. 49(b), (c) and (d). In general, the f_{PF} values are descending from 3 at the concentration of 1 g/L to the value of 1.47 at the concentration of 20 g/L. Both types of hemoglobin dilutions show an exponential to the concentration in the power index of -1/2 (see Equ. 11).

$$f_{Pf}^{\lambda_i}(Ct) = \alpha \cdot Ct^{-0.5}; \alpha := const. \tag{11}$$

This exactly matches the propensity found in the spectrophotometric characterization of the f_{PF} of the hemoglobin dilutions in the cuvette (refer back to Tbl. 5). Regardless of the illumination-detection geometry, the f_{PF} value is partly decided by the hemoglobin concentration.

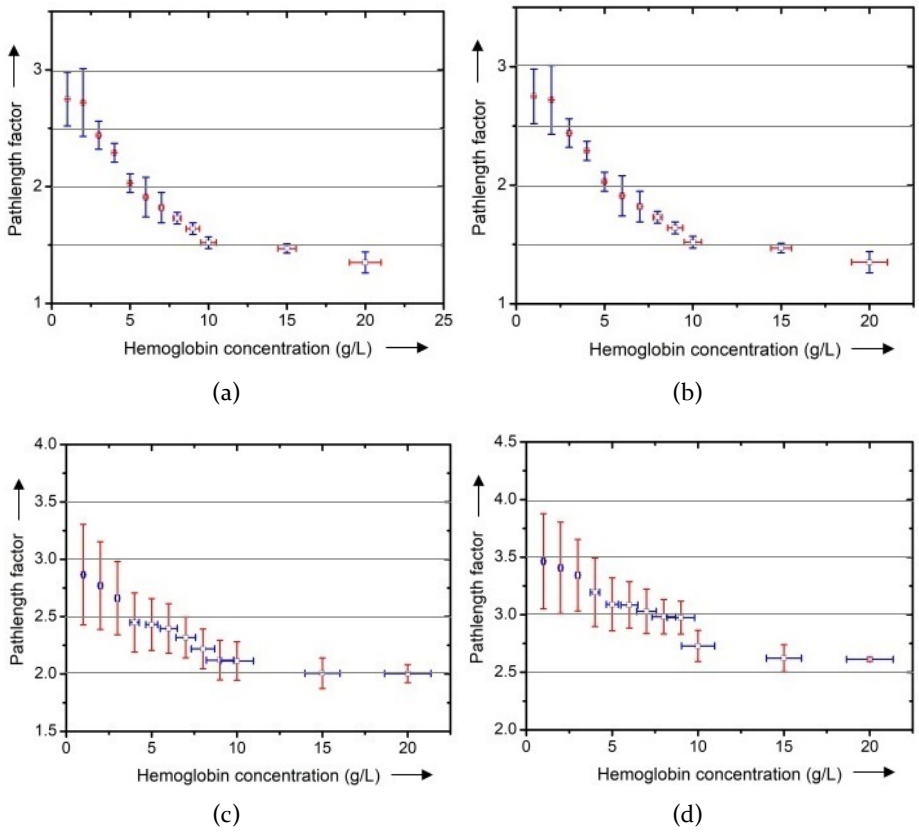

Figure 49: The recovered path length factors of (a) the oxygenated hemoglobin at 537nm, (b) the oxygenated hemoglobin at 577nm (c) the deoxygenated hemoglobin at 537nm, and (d) the deoxygenated hemoglobin at 577nm against the hemoglobin concentration are given. These measurements are done on one of the optofluidic phantoms with the mean values in the μ_a and μ_s' of the phantom matrices.

It is expected that the optical path length factor of the artificial hemoglobin dilution is the property of the sample itself, and its measured value does not change with different turbidities of the phantom matrices. To prove this, the optical path length factors of the oxy- and deoxygenated hemoglobin dilutions are quantified in a series of optofluidic phantoms at the wavelength

of 537 and 577nm. The μ_a and μ_s' of the optofluidic matrices range respectively from 0.12 mm^{-1} / 2.4 mm^{-1} to 0.51 mm^{-1} / 5.7 mm^{-1} (see Fig. 50).

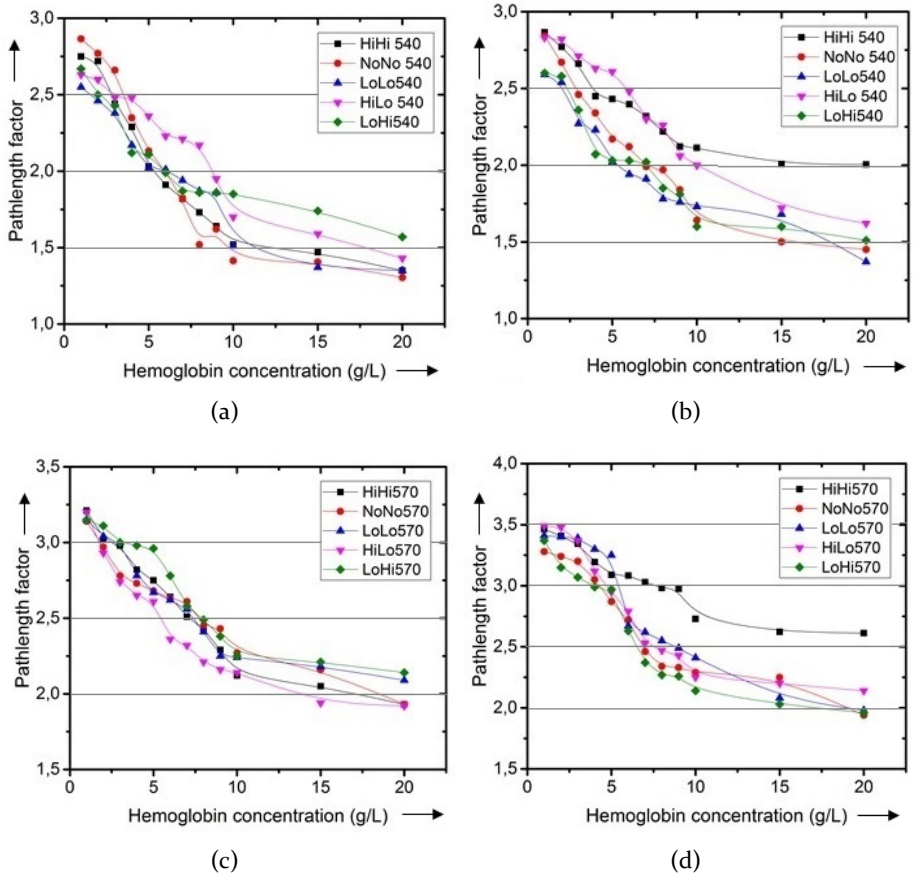

Figure 50: The recovered path length factors of (a) the oxygenated hemoglobin at 537nm, (b) the oxygenated hemoglobin at 577nm, (c) the deoxygenated hemoglobin at 537nm, and (d) the deoxygenated hemoglobin at 577nm against the hemoglobin concentration are given. These measurements are done on different optofluidic phantoms with different turbidities. The turbidities of the phantom matrices are named as HiHi (High scattering Hi Absorbing), MidMid, and LowLow etc.

As shown in Fig. 50, the concentration-dependent spectra of the optical path length factors are varying in an inhibited interval. For instance, when comparing the f_{PF} of the oxygenated hemoglobin (5 g/L concentration) in the HiHi (High scattering High absorbing) phantom to that in the LowLow phantom, the value is only slightly changing from 2.1 ± 0.21 to 2.3 ± 0.17. The same minor

change can be found in evaluating the f_{PF} of the hemoglobin in all other concentrations in phantoms with different turbidities. Overall, the registration of the optical path length factor of the artificial hemoglobin dilution is not influenced by the optical turbidity of the phantom. The only exception is found in one specifically prepared phantom, with the absorption coefficient two times higher than that of the HiHi phantom. In this phantom, the f_{PF} is not consistently given during the repetitive measurements. This is due to the fact that the light absorption in the phantom matrix is overwhelmingly dominating, and almost no light passes through the phantom matrix toward the detection core. This disrupts the acquisition of the optical signal or at least gives an extremely low signal-to-noise ratio. It means that the proposed diffuse optical biopsy might not be suitable for acquiring the light attenuation from highly absorbing tissue.

6.1.2 Oxygenation measurements on optofluidic phantoms

In the inverse measurements, the hemoglobin dilutions with random concentration (known and single blind to the investigator) are pumped into the optofluidic phantom. Based on the known ${}_PF$ values of the oxy- and deoxyhemoglobin dilutions and the estimation of their concentration dependencies as given by Equ. 11, the blood concentration is calculated. If the recovered blood concentration values match approximately to the concrete pre-defined concentration values, this inverse measurement is a success. To validate the reproducibility, phantoms with injected oxy-/deoxyhemoglobin is scanned thrice with a 5×5mm FOV to include the entire optofluidic structure, and the data is taken from 20 randomly chosen points in the images. The reconstructed images of the blood concentration distribution on the optofluidic phantom are shown in Fig. 51. Notice here the hemoglobin concentration $CtHbO2$ and $CtRHb$ are first recovered in the unit of grams and later converted to gram per molar mass-tissue considering the constancy in the tissue/phantom mass as assumed. The normalized values are calculated to represent the absolute blood oxygenation saturation SO_2 in percentage.
Figure 51 shows the reconstructed images of the $CtHbO_2$ and $CtRHb$ distribution with a scanning step size of 20μm. The image of the $CtHbO_2$ distribution (see Fig. 51(a)) designates very remote changes compared with the image of the $CtRHb$ distribution. The grayscale evaluates the concentration of the oxygenated and deoxygenated hemoglobin in the corresponding images, by which the outline of the optofluidic structure is drawn and matches the OCT top view (refer back to Fig. 34). In the projection image of the blood concentration in the phantom with the oxygenated hemoglobin, the $CtHbO_2$

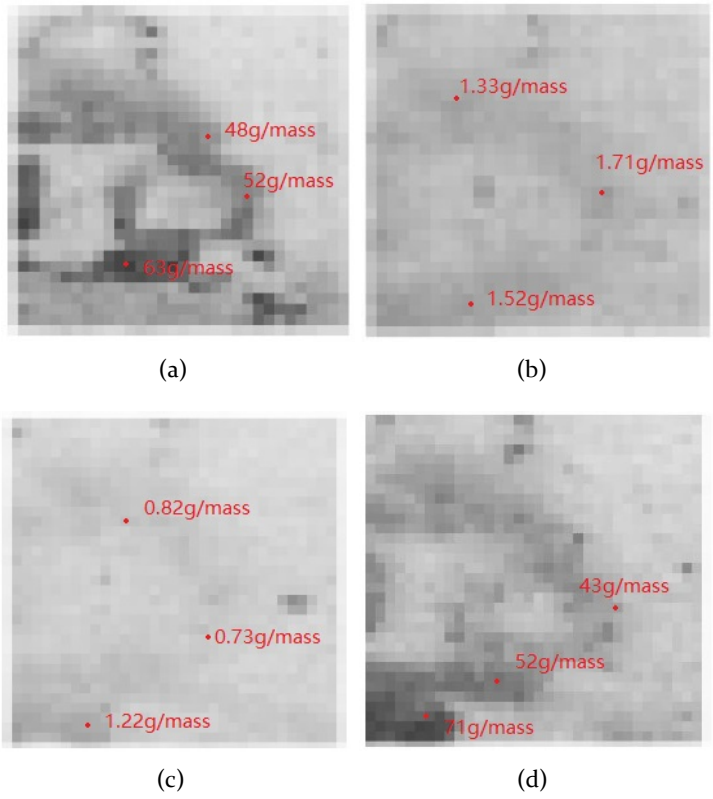

Figure 51: The mappings of the blood concentration are given to represent the distribution of (a) the $CtHbO_2$ and (b) $CtRHb$ when the oxygenated hemoglobin dilution is injected in the phantom; (c) the $CtHbO_2$ and (d) $CtRHb$ when the deoxygenated hemoglobin dilution is injected in the phantom.

shows an average value of 57 g/$mass_{tissue}$, meanwhile the $CtRHb$ in an average value of 1.3 g/$mass_{tissue}$. In the projection image of the blood concentration in the phantom with the deoxygenated hemoglobin, the image gives an antithesis demonstration as expected. In this case, the $CtHbO_2$ gives an average value of 1.27 g/$mass_{tissue}$, meanwhile the $CtRHb$ in an average value of 49.1 g/$mass_{tissue}$. All scans are culminated within 20 min. During this time, the oxygenation/deoxygenation status of the included hemoglobin dilution is not deteriorated, and the hemoglobin does not deposit either.
Figure 52 shows the calculated blood oxygenation saturation in the normalized value $SO_{2measured}/SO_{2real}$. These normalized values should be around 1 if the measured SO_2 values approach the exactly defined values. Seen from

the figure, an average normalized value of 1.32 is found for the deoxygenated hemoglobin and 1.42 for the oxygenated hemoglobin. There is a 20 - 30 % distinction between the calculated and the expected values. This means, the calculation of the SO_2 is not totally correct and has to be compensated (claimed in the later subsection).

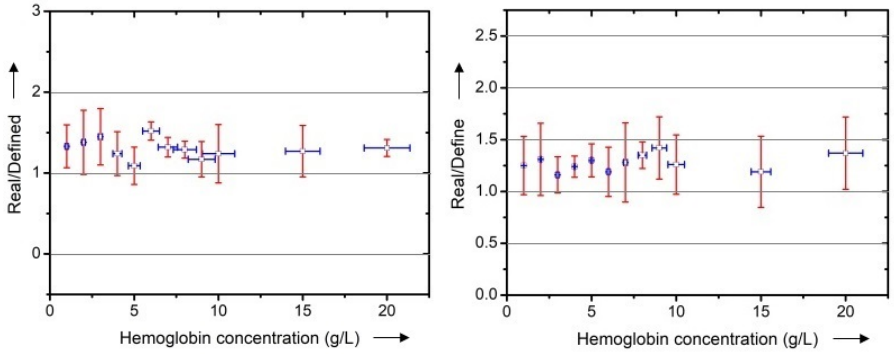

(a) (b)

Figure 52: The normalized $SO_{2measured}/SO_{2real}$ values of (a) the oxygenated and (b) the deoxygenated hemoglobin dilutions in different concentrations from 2 - 20 g/L are given. They are measured on the optofluidic phantoms with different turbidities in the matrices.

One should also notice that the parameter of SpO_2 has never been used to specify the oxygenation saturation in this work. The peripheral oxygen saturation (SpO_2) is an estimation of the oxygen saturation level usually measured with e. g. a pulse oximeter or homeostasis device. Healthy individuals usually exhibit a peripheral oxygen saturation value between 96% and 99%. A SpO_2 value below 90% could already indicate the hypoxia. The SpO_2 is a more global definition, while the SO_2 is more meaningful in this work because it indicates the oxygenation of the targeted tissue margin. In the common clinical case of e. g. measuring the tissue oxygenation saturation in muscle, the measured SO_2 values are normally 10 to 20 % lower than the SpO_2 values on the same test target at the same measuring site. A SO_2 value of 75-91% is considered as a normal range to represent the normoxia. It is assumed that the SO_2 value of 85% as the level for defining the normoxia in the case of the diffuse optical measurement[52].
It is also necessary to mention here the reason for not directly using the original unit of the $CtHbO_2$ and $CtRHb$ to represent the hemoglobin concentration. The dilemma is that the conversion of its unit shows an inconsis-

tency when calculating the molar mass of the oxygenated and deoxygenated hemoglobin. Taking the $CtHbO_2$ as the example, the unit is first recovered in mol to fit the unit of the molar extinction coefficient of the blood, with the unit in $1/cm.molarmass_{blood}$. For a better match of these oximetry parameters to the experimental implementation, it is purposefully re-calculated in grams and present it in grams per $mass_{tissue}$. Problem is then found during the calculation, that the molar mass of the used human hemoglobin product is reported differently in different technical brochure, mostly around 62330 - 65480 g/mol. The variance in the molar mass of the used human hemoglobin brings uncertainties in the actual molar mass of the hemoglobin regarding the unit of $CtHbO_2$ and $CtRHb$. For this reason, it is preferred not to use the original unit of the $CtHbO_2$ and $CtRHb$. The unit of the SO_2 is not affected because the molar mass/mass in the unit of the $CtHbO_2$ and $CtRHb$ are divided from the physical unit during the normalization[P3].

6.1.3 Factors affecting accuracy of measurements

By dissevering the characterizing apexes of the hemoglobin in the light attenuation spectra, the oximetry parameters $CtHbO_2$, $CtRHb$ and SO_2 can be inversely calculated. To convert the optical spectra into these oximetry parameters, the modified Beer-Lambert Law has been predominantly applied. The MBLL is described as a simple adding of the light attenuation from the absorption of the hemoglobin and the scattering of the tissue matrix within a certain light path. The MBLL is propitious over other algorithms because it has the least variables to solve. The most established diffuse optical approaches measure the δCt_{HbO_2} and δCt_{RHb} values instead of their absolute values, since the factor of the optode geometry and the scattering issue F_{scatt} are not calculated. However, it is beyond the boundary condition of the MBLL to calibrate the differential path length factor when the distance between the optodes exceeds about 2.5cm[53]. Also, when deriving the $CtHbO_2$ and $CtRHb$ through the MBLL with a global-change assumption (see Equ. 12), serious errors can arise if the focal change in the hemoglobin concentration is present[46]. Similarly for the scattering tissue matrix, using the global-change assumption causes a misrate of different turbidities among each single chromophore kind. For example, the collagen fiber has a totally different scattering level from that of the epidermal matrix. Also, the use of the diffuse optics comes with some other constraints.

$$OD^{\lambda_i} = [\varepsilon^{\lambda_i}_{HbO_2} \cdot CtHbO_2 \cdot d + \varepsilon^{\lambda_i}_{Hb} \cdot CtRHb \cdot d] \cdot f^{\lambda_i}_{PFblood} + F_{scatt} \qquad (12)$$

The path length factor in the scattering issue F_{scatt} is characterized through the variation of the diffusion equation. In this case, a mismatch in quantifying the μ_a and $\mu_s^{'}$ of the phantom matrices can cause a minor shift in the given F_{scatt} values compared to other established works. This is mainly due to the fact that other researchers mostly use Monte-Carlo-Inversion or four-flux-approximation to calculate the μ_a and $\mu_s^{'}$, which do not perfectly match our method. It is suggested to adopt the Inverse-Adding-Doubling for the conversion of the optical coefficients because it requests the least computational power for the calculation. Resultantly, the F_{scatt} shall no longer be a simple unchanged value. To address this, a compensation factor should be input in the MBLL to fine-tune the discrepancies brought by the minor misrate in the F_{scatt} within the vicissitude of the phantom types (see Equ. 13).

$$OD^{\lambda_i} = [\varepsilon_{HbO_2}^{\lambda_i} * C_{HbO_2} * f_{DPFHbO2}^{\lambda_i} + \varepsilon_{Hb}^{\lambda_i} * C_{Hb} * L * f_{DPFRHb}^{\lambda_i} + f_{compensate} + F_{scatt} \tag{13}$$

Measures are taken to make a better estimation of the F_{scatt} (actually the $f_{PFmatrix}$) of the phantom matrices regarding its scattering nature. Experimentally, the light attenuation is quantified when the optical probe is placed upon the regime with no fluidic pattern, or no 'vascular structure' underneath the surface. The OD values from this regime are compared to the calculated F_{scatt} values predicated on the known μ_a and μ_s' values. By following the reverse calculations and the tribulation-and-error method, compensation factors in the value of 0.15 at the wavelength of 537nm and the value of 0.173 for 577nm are given. These values are regarded as optimal to compensate the misrate in the F_{scatt} by a substantial extent (see Equ. 14).

$$F_{scatt} = (\mu_a + \mu_s) * f_{DPFRHb}^{\lambda_i} + 0.15(537nm)/0.173(577nm) \tag{14}$$

The $SO_{2measured}/SO_{2real}$ values are re-calculated based on the compensation. A comparison of the recovered oxygenation parameters before and after the compensation is given in Fig.53. The results are re-plotted based on the established raw data, where a 30% distinction between the $SO_{2measured}$ and the SO_{2real} is found before the compensation. After optimizing the calculation by inserting the compensation factors into the MBLL, a normalized value $SO_{2measured}/SO_{2real}$ around 1.07 is conclusively achieved, which is more proximate to the expected value of 1.

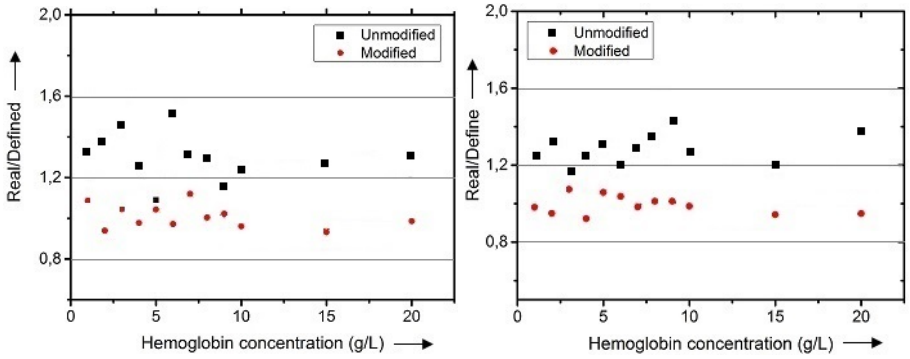

Figure 53: Comparison between the calculated $SO_{2measured}/SO_{2real}$ values before and after the compensation for (a) the oxygenated hemoglobin in the phantom (b) and the deoxygenated hemoglobin in the phantom, is given.

6.2 Lesion analysis on elastofluidic in-vitro phantoms

6.2.1 Light propagation shifts in elastofluidic phantoms

During the application case of the diffuse optical biopsy, the optical fiber probe is directly placed at the phantom/skin surface. The advantage of using the contact-based probe is that the optical signaling is not sensitive to factors like focusing or light phase matching. However, the induced mechanical stress could affect the light propagation because it changes the density and resultantly the refractive index of the tissue part at the contact site. To reflect the light propagation shift and investigate this in phantoms, optical elastography experiments are done on the PVCp slabs with the same Young's moduli as the elastofluidic phantom matrices (see Fig. 54).

As the result of the optical elastography studies, the fringe pattern is presented as black-white lines in a binary image. High order interference fringe pattern around the contact site between the optical fiber probe head and the superficial surface of the skin/phantom sample are shown, when the contact site undertakes the mechanical stress. In analysing the effect of the given normal load on the contact site between the modified optical probe and the phantom surface, a comparative analysis of the variance in different normal force (placed on the optical probe head) is performed. The modified probe head ensembles a transmutation (slightly concave from the cross-sectional view as seen in Fig.54(b)), where a marginal contact in the center of the probe is made. The intention for this design is that the concave structure

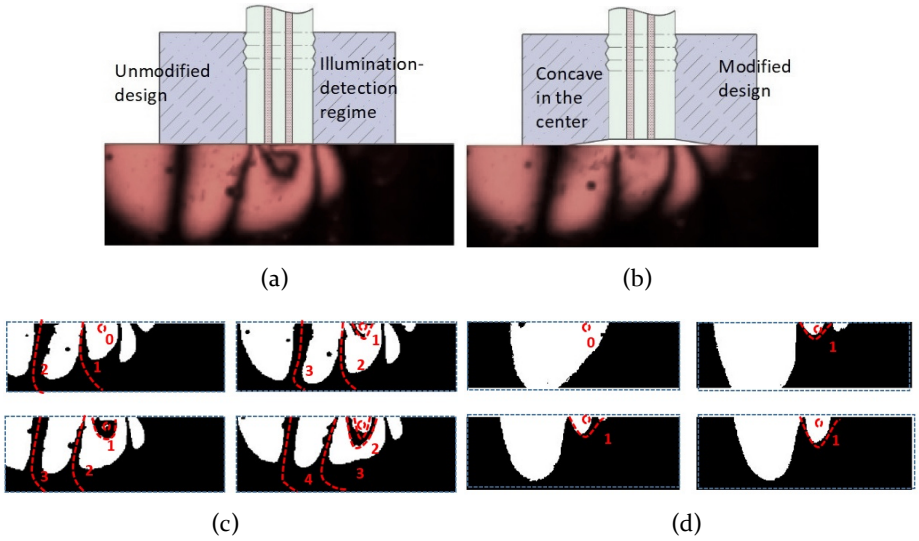

Figure 54: The recorded fringe patterns to represent the stress distribution in the PVCp phantom under the load from (a) the unmodified optical probe head and (b) the modified optical probe head are given. The binary fringe patterns under (c) 1, 2, 5, 10 N normal force from the unmodified probe head and (d) 1, 2, 5, 10 N normal force from the modified probe head are shown. The circle at the contact center represents the order 0, with each dash line representing one plus order in the fringe pattern.

commences all stress at the center of the optical probe head and disperses the stress toward the edge of the probe. As shown in Fig.54 (d), the fringe pattern with the highest intensity is found at the bottom of the contact site. An isochromatic pattern with a retardation phase of 1 is denoted around the contact site.

In the case of the unmodified optical probe head, it is seen in Fig.54 (c) that the 2nd fringe pattern starts to appear with the normal force increasing to 2 N. In the case of the modified optical probe head (see Fig.54 (d), the 1st order fringe pattern does not propagate further, even when the normal force increases from 1 to 10 N. When observing the fringe pattern with the highest order in the case of the modified probe head, the oblique loading induces a significantly less dense stress distribution compared to the contact between phantom and the unmodified probe head. It is seen in Fig. 54 (c) that the 4th order fringe pattern is about to be engendered in the case of the unmodified fiber probe. Compared to this, an isochromatic pattern with a lower retardation phase of 1 is denoted around the modified probe head at the contact site, within its change under the increasing mechanical load.

The primary stress remains rather constant with the normal force increasing from 1 to 10 N. As the optical elastography indicates, the mechanical stress distribution is concentrated at the contact site in the case of placing the unmodified optical probe head to the phantom surface. In contrast, more primary stress can be off-set at the contact site when the optical probe head is concave in the center. This fulfils the original intention of the modified design for the optical fiber probe head.
To verify the experimental results, as well as to quantitatively determine the magnitude of the stress in the tissue/phantom, a 2D FEM contact model is built by using COMSOL®(V5.2a, COMSOL Multiphysics; CPU:Intel(R) Core(TM) i7-6700HQ). The simulation includes the models to simulate the shape of the optical probe head as following: 1. SMA fiber head alone, 2. unmodified optical probe head, 3. modified optical probe head under the normal force as implemented during the optical elastography experiments. The geometry of the optical probe model is simplified from the real optical probe head in its cross-section. Domains for the phantom in its cross-section are defined as solid square-shaped patterns with the same geometry as the experimental PVCp phantom. A fine-tuned geometry edge (consummate load transfer) at the contact site is set over the entire interface. The designation for the Young's moduli of the phantom domain is obtained from the mechanical test on the PVCp slabs. The geometry of the reconstructed 2D model is meshed by triangular nets before the stationary study.

Table 8: The max. values of the primary stress at the near and far distance to the contact site center under the load of 1, 2, 5 and 10 N are given, including the cases of the SMA fiber head alone, the unmodified optical probe head, and the modified optical probe head.

	Modified contact	Unmodified contact	SMA head
Near 10 N	3.382 kPa	4.42 kPa	5.675 kPa
Near 5 N	1.56 kPa	2.53 kPa	3.18 kPa
Near 2 N	1.21 kPa	2.19 kPa	2.61 kPa
Near 1 N	0.49 kPa	1.54 kPa	2.12 kPa
Far 10 N	0.81 kPa	1.17 kPa	1.81 kPa
Far 5 N	0.23 kPa	0.975 kPa	1.35 kPa
Far 2 N	0.176 kPa	0.51 kPa	0.83 kPa
Far 1 N	0.161 kPa	0.482 kPa	0.639 kPa

Results can be plotted from the numerical simulation as shown in Tbl. 8. According to the simulation results, the max. primary stress is found at the bottom site of the unmodified probe head and reaches 4.42 KPa (at 10 N load force). In the modified probe head, a max. value of 3.38 KPa is found at the

same position, 24% lower than that of the unmodified probe head. Similar results can be found when plotting the primary stress at 1 centimeter to the center of the contact site. It gives a stress of 1.17 kPa at 10 N load force for the unmodified optical probe head against 0.81 kPa for the modified optical probe head. It is also noticed that the SMA fiber head alone generates the highest stress at the contact site, with a value 17 - 21% higher than that of the unmodified probe head even. This is due to the fact that it delivers the same normal force with a smaller contact area to the probe-sample interface. The conclusion is drawn that the modified optical fiber probe head with a concave cross-section helps to disperse the induced stress out of the central contact site. This minimizes the light propagation shifts at the area of the optical signaling during the diffuse optical measurements, which should be seen during the measurement on the real in-vivo skin tissue as well.

6.2.2 Oxygenation measurements on elastofluidic phantoms

The mapping of the hemoglobin concentration/oxygenation distribution in the elastofluidic phantom is done in the same way as the optofluidic phantom validation. The experiment is implemented by stitching 6 scanning schemes of 0.5cm by 0.5cm with a step size of 50μm, so as to give an entire view of the elastofluidic pattern within an acceptable time constrain. In this given scanning scheme, each stitch (or segmentation) should have 10 times 10 pixels. The experiments are conducted on 2 elastofluidic phantoms, by which the phantom matrices simulate the color tones/optical properties of the asian male and female volunteers respectively (namely OP6 and OP8). The image for the elastofluidic phantom (with OP6 recipe) with 10 g/L deoxygenated hemoglobin injection is shown in Fig. 55.
One factor has to be considered, that the soft PVCp matrices of the elastofluidic phantom deform when the hollow microchannels are perfused with the prepared hemoglobin dilution. The induced slight motion artifacts cause some pixel shifts in the projection image. The total mapping of the elastofluidic pattern is stitched out of 6 segmentations. After one scanning scheme is finished, the elastofluidic phantom is moved in XY-direction for the next scanning by tuning a manual micro-head stage placed under the phantom. The tolerance of the manual micro-head stage causes the complication in giving the missing components among each segmentation, although the missing part is very inhibited. Average contrast based on a prior estimation of the absorber location is given (see Fig. 55). It is shown that the absorber, which is more proximate to the broader edge of the elastofluidic structure, can be resolved with acceptable contrast. With the scanning step size of 50μm, the

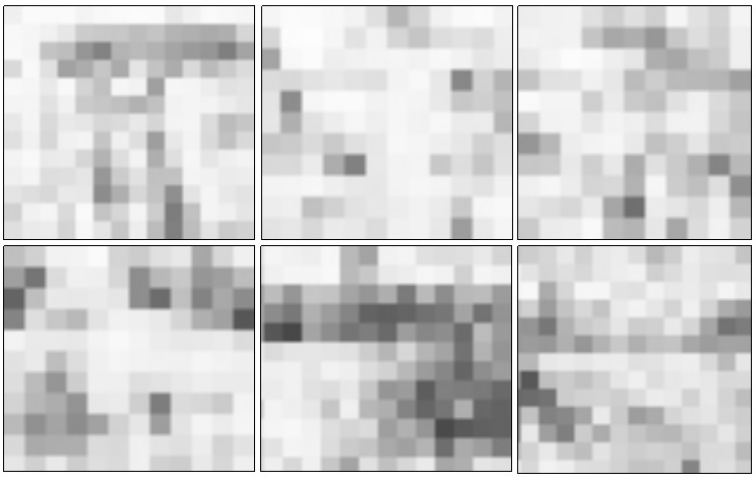

(a)

Figure 55: The mapping of the light absorbance on the elastofluidic phantom with the norm OP6, injected with 10 g/L deoxygenated hemoglobin, is stitched from 6 segmentations.

rhombus-shaped resolution target is lamentably reconstructed, because the size of the structure is already proximate to the step size.
Similar to the optofluidic phantom validation, it is also intended to make the projection of the light absorbance in the rhombus-shaped resolution target with the scanning step size of 1, 2, 5, and 10μm. Figure 56 shows a typical false-color-coded image of the elastofluidic pattern in the rhombus shape, where the outline of the proposed resolution target is found in the image acquired with a scanning step size of 5μm. From the projection images of the $CtHbO_2$ and $CtRHb$, 20 random sampling points are taken and an average from the measured values is made. After having the f_{PF} data of the major chromophores from the previous section[1], the tissue oximetry parameters are recovered. The $CtHbO_2$ gives an average value of 49.1 g/$mass_{tissue}$ at the dark regime, meanwhile the $CtHbO_2$ in an average value of 4.2 g/$mass_{tissue}$ at the light scattering background. The mapping of the deoxygenated hemoglobin gives an antithesis demonstration as expected. In the mapping of the hemo-

[1] Due to the similarity in the optical properties of the phantom matrices, it is preferred not to repeat the experiments of measuring the optical path length factors of the hemoglobin dilutions on the elastofluidic phantoms.

globin concentration on the phantom injected with deoxygenated blood, the mapping shows better contrast in the $CtRHb$ than that of the $CtHbO_2$. The $CtHbO_2$ gives an average value of 2.3 g/$mass_{tissue}$, meanwhile the $CtRHb$ in an average value of 51.7 g/$mass_{tissue}$.

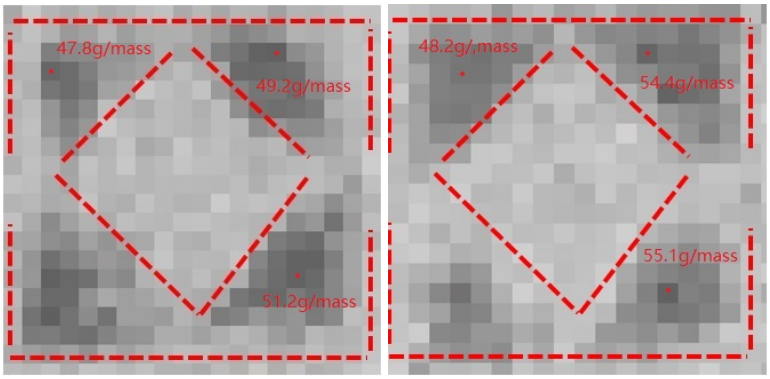

Figure 56: The reconstruction of the rhombus-shaped resolution target with the scanning step size of 5μm is given for the projection of (a) the $CtHbO_2$ in the phantom injected with the oxygenated hemoglobin dilution, and (b) the $CtRHb$ in the phantom injected with the deoxygenated hemoglobin dilution.

All recovered concentration values have a standard deviation of 7% as it is discerned from the error bars. One should notice that this standard deviation is registered from the elastofluidic phantom, which simply models the hypoxia and normoxia distribution of 'tissue' in separate sites. In the real in-vivo tissue, a transition zone exists between the hypoxia and normoxia tissue site and should indicate correspondingly a transition in the tissue oximetry. This means, a larger standard deviation is expected during the in-vivo experiments when registering the $CtHbO_2$ and $CtRHb$ values at different positions of the lesion site.
Figure 57 shows the calculated $SO_{2measured}/SO_{2real}$ values for the oxygenated and deoxygenated hemoglobin. Normalized values of 0.95 to 1.13 are given with a deviation of 5-10%. The reason for this is that the local heterogeneity in the spatial distribution of the scatterers in the elastofluidic matrices exists and brings random light scattering (refer to Fig. 44). When the diffusely reflected light in the elastofluidic phantom matrices is incident on the heterogeneous scatterers, backward scattering occurs, and more light is remitted back toward the detection core of the fiber instead of propagating forward. The heterogeneity in the spatial distribution of the scatterers, as well as the

generation of the backward scattering, are random. Such sophistications are purposefully made into the elastofluidic phantom matrices to forecast the possible deviation when recovering the tissue oximetry parameters during the in-vivo experiments.

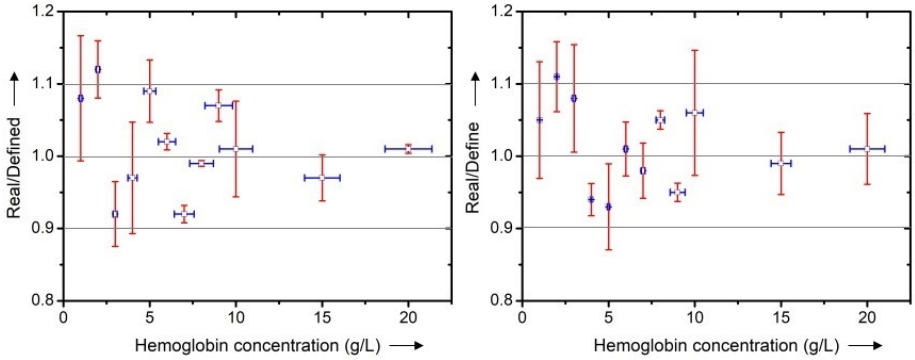

(a) (b)

Figure 57: The normalized values $SO_{2measured}/SO_{2real}$ of (a) the oxygenated and (b) deoxygenated blood dilutions are given to indicate their changes in different blood concentrations from 2 - 20 g/L. These values are measured on the elastofluidic phantoms with different turbidities in the matrices.

6.3 In-vivo studies on benign nevi lesion

Preliminary experiments by using the diffuse optical biopsy are done on the volar forearm at the palm of the asian female human volunteer to analyse the targeted spider nevi lesion. In this lesion, blood is localized in the superficial vasculature of the epidermis. Firstly, a projection image of the nevi lesion is given and compared to the photograph. The imaging strategy is to view the margin (2 -5mm in diameter) around the vascular spider and the swollen blood vessels, which are facilely located. The acquisition of the 3D OCT imaging of the lesion takes 15 minutes. The OCT imaging fails and therefore is not given due to the severe motion artifacts during the imaging process.
As shown in Fig. 58(a), the major closed margin includes the superficial swollen vessels which cross through the skin surface. One has a length of approx. 0.5cm, while the other one is curved in an inverse C-shape with a total length of 0.8cm. The co-registered images in Fig. 58(c) and (d) show the projection of the oximetry parameters $CtHbO_2$ and SO_2 of the margin around the inverse C-shaped swollen vessel. It is shown that in both photograph and diffuse

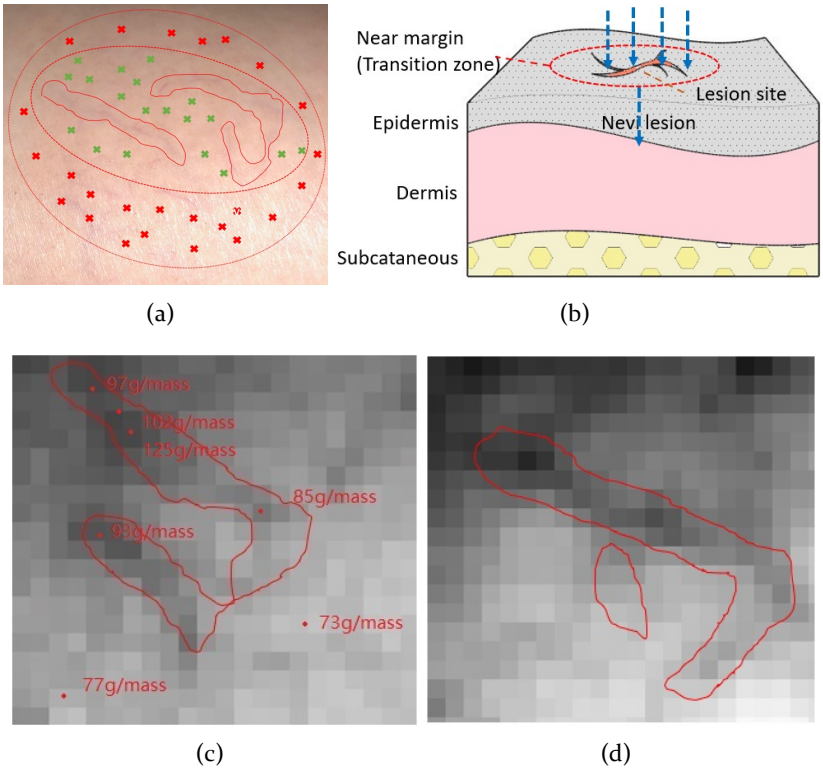

Figure 58: (a) The photographic top view of the near/far margin definition around the nevi lesion and (b) the demonstration of the light absorption at the swollen vessels in the nevi lesion are shown. The projection images of (c) the $CtHbO_2$ and (d) SO_2 in the margin around the lesion are given.

optical projection images, the entire morphology of the swollen vessels at the superficial skin are given. For the reconstruction of the blood concentration, high $CtHbO_2$ values of about 124 g/$mass_{tissue}$ on average are given at the lesion site. In the projection image of SO_2 (see 58(d)), a homogeneous pattern is found to represent the curved inverse C-shaped vessel with relatively high contrast to the background. For the projection of the vessel with a smaller scanning step length of 10μm, the conjunction of the swollen vessel (inverse C-shaped) to the nearby arteries are indicated with better depth discrimination.

To avoid the complication of the slow scanning procedure, probe studies are done in the near and far safety margins around the nevi lesion. The near safety margin includes the tissue margin in the radius distance of 1cm to the edger

of the nevi lesion. The far margin is defined as the regime in 2cm to the edge of the appearing lesion. The oxygenation status in the near margin around the lesion is taken and co-registered from 10 random sampling points (see Fig.58(a)). Also, an estimation of the $CtHbO_2$ is made from the measurement on an elastofluidic phantom with 50μm thickness superstrate. This phantom is supposed to simulate the condition of the superficial vessel distribution, like the case of the benign nevi lesion as indicated here. The co-registered values are given in Tbl.9.

Table 9: The recorded oxygenation saturation, the oxy-hemoglobin concentration values on each sampling point in the near and far margins around the nevi lesion, and the estimation from the corresponding elastofluidic in-vitro phantom are listed.

	Near n=3	Near n=10	Far n=3	Far n=10
Oxyhemo Conc.	97 g/L.ms	93 g/L.ms	75 g/L.ms	71 g/L.ms
Esti. Oxygnation	87%	87%	81%	81%
Blood oxygnation	89±2%	86±4%	83±1%	82±2%

As the result, an average value of 97 g/$mass_{tissue}$ is read, which is over-estimated compared to the values of 75 g/$mass_{tissue}$ registered from the far tissue margin . This is due to the fact that the spider nevi lesion are more superficial to the skin surface, compared to other vessels embedded in the deep dermis. This increases the share of the optical absorption of the blood in the swollen vessel in the total light attenuation when calculating through the MBLL (see Fig. 58 (b)). The depth of the capillary network in the near margin is 'transiting' from the superficial swollen vessels to the normal status and is therefore closer to the skin surface. This would also reduce the share of the light scattering of the ECM in the near margin, or the so-called 'transition zone' near the lesion site (see Fig.58(b)). For the SO_2 in the near margin, an estimated value of the SO_2 at 87% is given for the near margin due to the depth discrimination of the light absorption from the shallow vessel network in this tissue margin. The registered SO_2 values from the diffuse optical measurements are around 89±2%.
The far margin shows a drop in the blood concentration as well as the blood oxygenation. This drop comes, on one side, from the fact that the capillary network is more distributed in the deep dermal and absorbs less light. On the other side, the surrounding extracellular matrix is not any more clustered with a rich capillary network. Instead, a smaller dimension of the capillary vessels allows a more homogeneous adsorption/release of oxygenation from the hemoglobin to the surrounding tissue. Variations in the recovered values at the same site are within 5%. All measured values fulfil the expectation for

the full oxygenation status based on the normoxia metabolism of the nevi lesion.

6.4 In-vivo studies on potential cutaneous nodule lesion

The potential nodule lesion on the asian male volunteer is reconstructed. It gives in the photograph two light-dark lesion margins on the skin surface, which are more minuscule than that of the embedded scab under the skin epidermis. The scab of the nodule lesion has a hard boundary to the circumventing healthy tissue (see Fig. 59(a) and (b)). In this case, the incident light is diffusely reflected in the scattering-dominant epidermis and depth of the embedded scab exceeds the effective penetration depth of the OCT used. Combined with the severe motion artifacts, the OCT imaging of the embedded scab underneath the nodule lesion site fails.
The major complication of performing the contact-based experiment over the embedded scab is that the scab is a relatively hard tissue conjugated to the surrounding ECM. Its position in the skin can be labelled by the dark superficial lesion margins at the skin surface, although the shape of the lesion does not equal to the shape of scab itself. To address this, a bigger scanning scheme is given. The co-registered image in Fig. 59(d) shows the distribution of the oximetry parameter SO_2 at the lesion site. The SO_2 values at the lesion site are around 87% on average. These values are slightly above the average value that normally represents the normoxia metabolism. Both photograph and diffuse optical approach attest the morphology of the superficial nodule lesion. For the reconstruction of the blood concentration, high $CtHbO_2$ values of about 117 g/$mass_{tissue}$ on average are given at the lesion site. This again proves that the light brown color of the superficial nodule lesion is not caused by the condensation of the skin pigmentation. Instead, the angiogenesis activities at the lesion site are active, and the blood content in the lesion induces the light absorption.

Table 10: The recorded oxygenation saturation, the oxy-hemoglobin concentration values on each sampling point in the near and far margins around the nodule lesion, and the estimation from the corresponding elastofluidic in-vitro phantom are listed.

	Near n=3	Near n=10	Far n=3	Far n=10
Oxyhemo Conc.	76 g/L.ms	78 g/L.ms	79 g/L.ms	74 g/L.ms
Esti. Oxygnation	81%	81%	81%	81%
Blood oxygnation	83±4%	84±2%	82±3%	83±2%

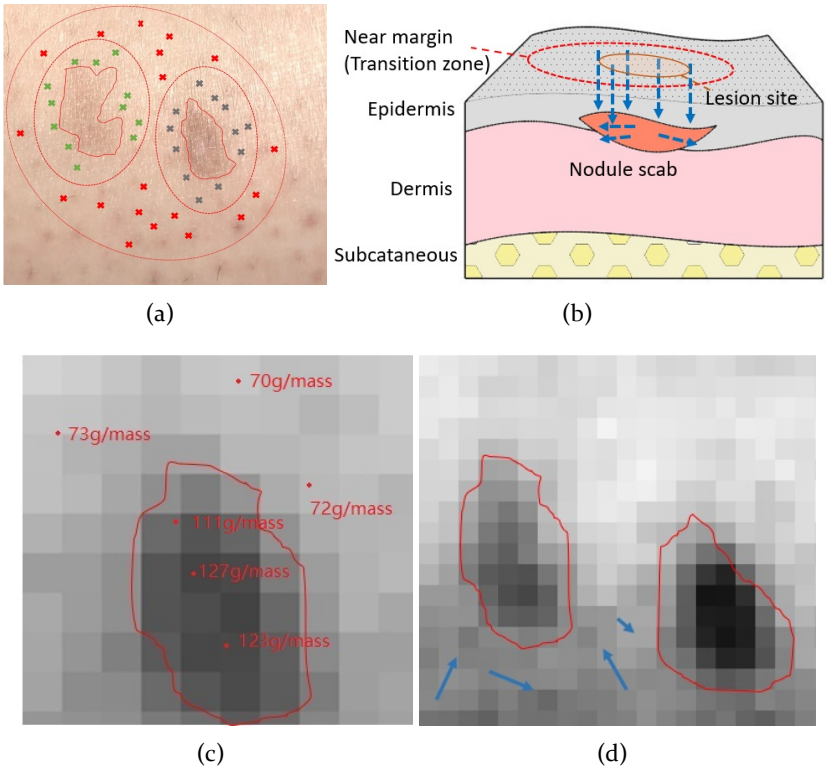

Figure 59: (a) The photographic top view of the near/far margin definition around the nodule lesion and (b) the demonstration of the light scattering at the scab in the nodule lesion are shown. The projection images of (c) the $CtHbO_2$ and (d) SO_2 in the margin around the lesion are given, with the blue arrows pointing to the the reconstruction of the keratosis pilaris.

The SO_2 values in the near and far margins range from 82 - 83%. These values show the normoxia metabolism of the nodule lesion margin as expected. In principle, the recovered values of the tissue oxygenation in the near and far safety margins around the superficial nodule lesion fulfil the estimated values. However, an error in recovering the blood concentration at the lesion site is found. The hemoglobin concentration in the near margin around the nodule lesion varies from 77 - 78 g/$mass_{tissue}$ (see Tbl.10). It shows a totally different situation from the pilot study on the superficial nevi lesion. The $CtHbO_2$ values at the blood-rich nodule lesion margin are not overestimated toward the value of 90 g/$mass_{tissue}$, like that of the 'transition zone' around the nevi lesion on the female volunteer. This is due to the fact that the incident light is scattered at the embedded scab along the orientation of the fiberized

tissue. The diffusely reflected light registers the hemoglobin concentration above the scab only and hardly propagates forward into the deeper light absorbing tissue matrix (see Fig. 59(b)).
In the case of the nodule lesion analysis, the male volunteer is carrying keratosis pilaris, which is a genetic condition of skin's hair follicles. This is normally accompanied by the over-activated angiogenesis around the follicles, where the clustered blood capillary around the follicles absorbs more light. The existence of the keratosis pilaris and the induced light absorption at the site are seen as the complication during the diffuse optical measurement because they can be visually mistaken as the lesion sites. It is found that the keratosis pilaris sites are reconstructed in the 2D projection imaging in their proper positions to the nodule lesion site (see Fig. 59(c)). However, during the probe study, inappropriate positioning of the optical probe at the keratosis pilaris might mistakenly recover the tissue oxygenation saturation of the keratosis pilaris instead of the nodule lesion. Consequently, erroneous high SO_2 values could be given in the case of the nodule lesion analysis when the scab is embedded under the keratosis pilaris and the incident light is absorbed by the blood content around the pilaris. Fortunately, this does not happen during the preliminary experiments. It is recommended to use the diffuse optical approach in the form of an optical probe, before the major complication of giving projection images (with large FOV), namely the prolonged scanning duration, is solved.

6.5 Uses of microphysiological phantoms in other applications

It is beneficial to conduct the same phantom validation on the opto-/elastofluidic phantoms during the research on other optical angiographies/optical probes (see Fig. 60) as that of the diffuse optical biopsy introduced in this work. In the case of the epidemiological lesion analysis of the melanoma site by using the LOT, the tumor malignancy is determined by the oxy-saturation SO_2 merged in the image. The imaging accuracy can be validated by evaluating the sensitivities/specificities of measuring the SO_2 of the prepared blood on the elastofluidic phantom. The existence/non-existence of the to-be-simulated melanoma site can be defined by perfusing the oxy-/deoxygenated hemoglobin dilutions into the elastofluidic phantom, which reflect the hypoxia/normoxia metabolism.
For the application case in validating the PAT imaging reconstruction, the softener concentration in the plastisol matrices can be tailored in absolute

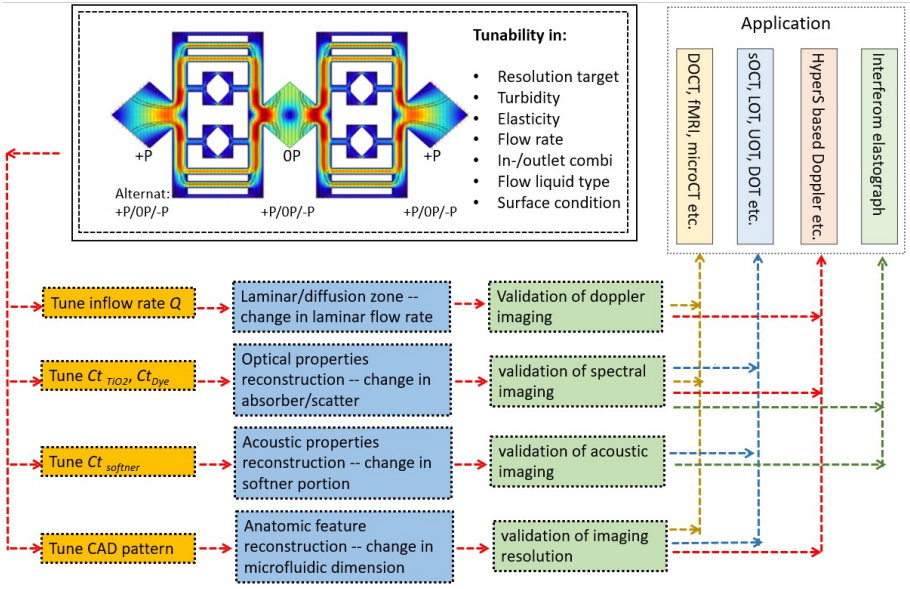

Figure 6o: A suggested routine of using the opto-/elastofluidic phantoms to discipline the translational studies in the research on multi-modal angiographies/optical probe approaches is given.

quantities to tune the acoustic impedance of the phantom matrices. This helps to understand the influences on the thermal generation of the acoustic wave from the incident laser stimulation. It is also suggested to reconstruct the velocity field of the liquid flow via the doppler OCT on the elastofluidic phantom. Here, calibrating the flowmetry parameter *velocity v* through the turbid media of the phantom can be one of the perspectives. Calibrating the doppler OCT by comparing the recovered flow dynamics in the high/low velocity flow channels could also be one of the application cases. Researchers could alternatively choose to define the flow rate and manipulate the blood hydraulic in the 'vasculature' by placing plus/minus/zero liquid pressure at the in-/outlets. All these features can be initialized in numbers and given by a numerical simulation model based on the Navier-Stokes equation to check the recovery correctness.

Application cases in non-optical imaging approaches are suggested as well, including the micro-CT, the CT-angiogram, the functional MRI, and the molecular radiography etc. The in-vitro microphysiological vascular phantom models can also be used as the reproducible, tunable imaging targets to improve/accelerate the data training process during the research on AI-

assisted pattern recognitions. They help to reduce the amount of human/animal targets needed, simplify the ethical conduction of clinical studies, and provide better variance in defining the anatomic/biological specifications in the training datasets.

7 Summary and outlook

In the medical application of using tissue equivalent models to calibration variant medical skin imaging approaches, discrepancies between the established in-vitro phantoms and the in-vivo skin obstacle their uses as the validation test charts during the translational studies, and therefore, must be addressed. Motivated by this, unique prototypes of opto-/elastofluidic in-vitro microphysiological vascular phantom models are investigated to simultaneously replicate the skin equivalent light/sound-tissue-interaction and the blood perfusion of the vascularized human skin.

In this work, optofluidics with the optical insertion of nano-spheres and molecular dyes in the sub- and superstrate matrices are laminated through the partial diffusion of the chemical monomer bonds at the interface. This enables the manipulation of the optical turbidities of the phantom matrices. To assign the in-vitro phantoms with the same randomness in the heterogeneous propagation of light/sound wave as that in the elastic skin tissue, plastisol is used and laminated directly into elastofluidics without any polar/medium-polar adhesive. Lastly, artificial whole blood is prepared to replicate the optical path length factor f_{PF} of all major chromophores in the real human whole blood in their global distribution to achieve their equivalences in the optical absorbance.

As the outcome, the optofluidic in-vitro microphysiological vascular phantoms are constructed of the castable PU with the TiO_2/ink/molecular dye insertions in the matrices. The optical absorption coefficient μ_a and the reduced scattering coefficient μ_s' of the phantom matrices are tailored and approach the ex-vivo/in-vivo results from the human skin tissue with different color tones. The same μ_a and μ_s' are replicated in the PVCp matrices of the elastofluidic phantom matrices. Besides, the elastofluidic phantom can withstand high liquid pressure up to 6 bar and high flow rate of 10 mL/min for up to 96 h. The Young's moduli E and the sound velocity are tailored to approach those of the real skin. The speed of sound propagating through the PVCp matrices is found at 1350 to 1500 m/s, which is close to that of the in-vivo skin tissue. The artificial whole blood is prepared and converted to the oxygenated and deoxygenated status by tuning the PH value of the prepared dilutions. It is proved through the spectrophotometric measurements, that they replicate the wavelength dependent spectral features as the real human whole blood in the α and β peaks. The oxygenation and deoxygenation status of the artificial blood stays stable over time at a total hemoglobin concentration of 20 g/L for 30 min.

The use of the opto-/elastofluidic microphysiological in-vitro vascular phantoms is first given within the application case on a fiber-based diffuse optical biopsy to register the oximetry parameters of the blood included in the opto-/elastofluidic phantoms. For both oxy- and deoxygenated hemoglobin, the concentration dependencies of the optical path length factors $f_{Pf}(Ct)$ and the absolute values of the oxygenation saturation SO_2 are characterized. The technical routine of using the opto-/elastofluidic microphysiological phantoms for validating other optical biopsies is suggested.
The opto-/elastofluidic in-vitro microphysiological vascular phantom models simultaneously imitate the vascularization anatomy, the multiple-layered structure, the light-tissue interaction, the sound-tissue-interaction, the light-blood-interaction, the skin mechanical elasticity, and the heterogeneity in the chromophores' distribution of the vascularized skin tissue. They can still be tailored within a wide biophysical range to reflect other bionic features of different tissue types. These in-vitro phantoms can aid to address current issues of uncertainties of the in-vivo experiments, allow more precise system validations without any concern on medical ethics, and consequently simplify the clinical affairs management during the pre-clinical research on the optical biopsies of all kinds.

8 Zusammenfassung und Ausblick

Bei der medizinischen Anwendung der Verwendung von gewebeäquivalenten künstlichen Modellen zur Kalibrierung verschiedener medizinischer Hautbildgebungsverfahren stehen Diskrepanzen zwischen den etablierten In-vitro-Phantomen und der In-vivo-Haut ihrer Verwendung als Validierungstestcharts während der translationalen Studien im Wege und müssen daher angegangen werden. Aus diesem Grund werden einzigartige Prototypen von opto-/elastofluidischen mikrophysiologischen In-vitro-Gefäßphantommodellen untersucht, um gleichzeitig die hautäquivalente Licht-/Schall-Gewebe-Wechselwirkung und die Blutperfusion der vaskularisierten menschlichen Haut nachzubilden.
In dieser Arbeit werden die gewebeäquivalenten opto-/elastofluidischen mikrophysiologische Modelle dargestellt. Optofluidiken mit der Einfügung von Nanosphären und molekularen Farbstoffen in die Sub- und Supermatrizen durch die partielle Diffusion der chemischen Monomerbindungen an der Grenzfläche laminiert. Dies ermöglicht die gezielte Beeinflussung der optischen Trübungen der Phantommatrizen. Um die In-vitro-Phantome mit der gleichen Zufälligkeit in der heterogenen Ausbreitung der Licht-/Schallwelle wie im elastischen Hautgewebe zuzuordnen, wird Plastisol verwendet und ohne polaren/mittelpolaren Klebstoff direkt in Elastofluidik laminiert. Schließlich wird künstliches Vollblut vorbereitet, um den optischen Weglängenfaktor f_{PF} aller wichtigen Chromophore im realen menschlichen Blut in ihrer globalen Verteilung zu replizieren, um ihre Entsprechungen in der optischen Absorption zu erreichen.
Als Ergebnis werden die optofluidischen In-vitro-Gefäßphantome aus dem gießbaren PU mit den TiO_2/Tinte/Molekularfarbstoff Einbettungen in den Matrizen hergestellt. Der optische Absorptionskoeffizient μ_a und der reduzierte Streukoeffizient μ_s' der Phantommatrizen sind angepasst und nähern sich den ex-vivo/in-vivo-Ergebnissen aus dem menschlichen Hautgewebe mit unterschiedlichen Farbtönen an. Dieselben μ_a und μ_s' werden in den PVCp-Matrizen der elastofluidischen Phantom-Matrizen repliziert. Außerdem kann das elastofluidische Phantom einem hohen Flüssigkeitsdruck von bis zu 6 bar und einer hohen Durchflussrate von 10 mL/min bis zu 96 h standhalten. Die Young'schen Module E und die Schallgeschwindigkeit sind so ausgelegt, dass sie denen der realen Haut nahe kommen. Die Schallgeschwindigkeit, die sich durch die PVCp-Matrizen ausbreitet, liegt bei 1350 bis 1500 m/s, was nahe an der des in-vivo-Hautgewebes liegt. Das künstliche Vollblut wird präpariert und durch Abstimmung des PH-Wertes der

hergestellten Verdünnungen in den sauerstoffreichen und sauerstoffarmen Zustand überführt. Durch die spektrophotometrischen Messungen wird nachgewiesen, dass sie die wellenlängenabhängigen spektralen Merkmale wie das reale menschliche Blut in den α- und β-Peaks reproduzieren. Der Oxygenierungs- und Desoxygenierungsstatus des künstlichen Blutes bleibt bei einer Gesamthämoglobinkonzentration von 20 g/L für 30 min über die Zeit stabil.

Der Einsatz der opto-/elastofluidischen mikrophysiologischen In-vitro-Gefäßphantome erfolgt zunächst im Rahmen des Anwendungsfalles an einer faserbasierten diffus-optischen Biopsie zur Erfassung der Oximetrieparameter des in den opto-/elastofluidischen Phantomen enthaltenen Blutes. Sowohl für das oxygenierte als auch für das deoxygenierte Hämoglobin werden die Konzentrationsabhängigkeiten der optischen Weglängenfaktoren $f_{Pf}(Ct)$ und die Absolutwerte der Sauerstoffsättigung SO_2 charakterisiert. Es wird eine technische Routine zur Verwendung der opto-/elastofluidischen mikrophysiologischen Phantome zur Validierung anderer optischer Biopsien vorgeschlagen.

Die opto-/elastofluidischen mikrophysiologischen In-vitro-Gefäßphantommodelle imitieren gleichzeitig die Anatomie der Vaskularisierung, die mehrschichtige Struktur, die Lichtgewebewechselwirkung, die Schallgewebewechselwirkung, die Lichtblutwechselwirkung, die mechanische Elastizität und die Heterogenität in der Verteilung der Chromophoren des vaskularisierten Hautgewebes. Sie können immer noch in einem weiten biophysikalischen Bereich auf andere bionische Merkmale verschiedener Gewebetypen zugeschnitten werden. Diese In-vitro-Phantome können dazu beitragen, aktuelle Fragen der Unsicherheiten der In-vivo-Experimente anzugehen, präzisere Systemvalidierungen ohne Bedenken in Bezug auf die ethischen Aspekte der Medizin zu ermöglichen und folglich die Verwaltung der klinischen Angelegenheiten während der präklinischen Forschung an optischen Biopsien aller Art zu vereinfachen.

9 Appendix

Drawing of the diffuse optical biopsy

- A bifurcated fiber with 65 µm core separation is used as the illumination-detection pair
- Programmable motorized stages carry the fiber probe and generate TTL (5V square) signal to trigger spectrometer

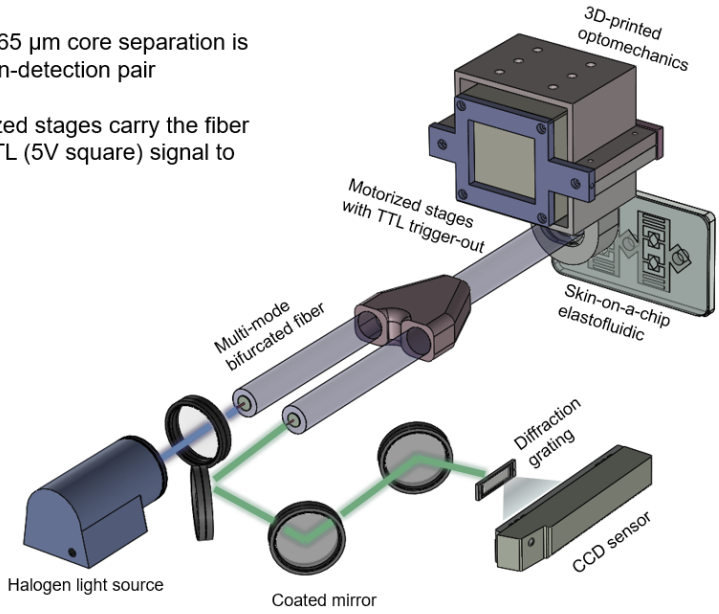

Modification in the scanning scheme of diffuse optical biopsy

The primary problem during the diffuse optical measurement is that the scanning procedure must be accelerated, so as to provide an efficiently sizeable FOV within a shorter duration. As described in the methodology section, a delay of at least 30 ms is needed upon each sampling point in the scanning scheme. Despite the dead/rise time of the compact spectrometer, the most time is spent on reading the GCS command (a delay of min. 10 ms is needed for reading each command line) from the software panel onto the motion controller. In this case, the PositionDistance mode is quoted to trigger the spectrometer during each motion pause. In this mode, a trigger pulse is indicted whenever the axis has covered the TriggerStep distance (CTO Parameter ID 1). As the alternative, the StartThreshold and StopThreshold mode can be defined to enable the trigger output for a constrained position range and a certain direction of motion only (either negative or positive, see Fig. 61)

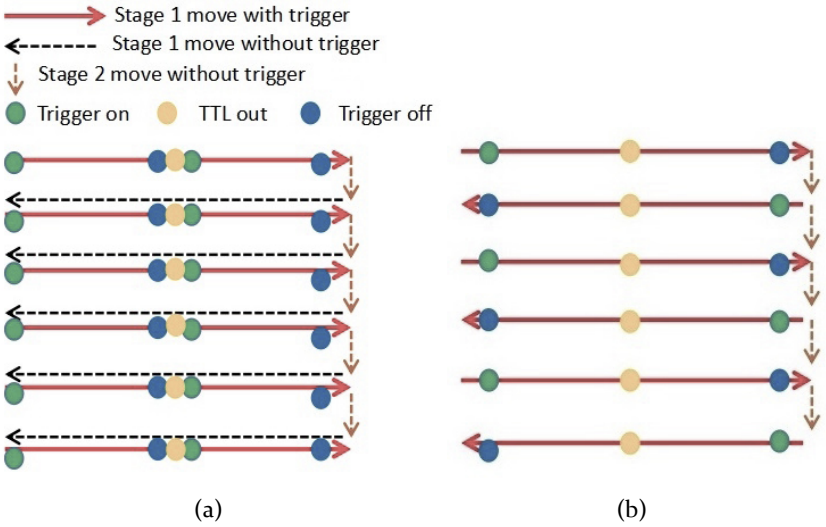

Figure 61: (a) The original scanning scheme and (b) the modified bidirectional scanning scheme with the notification of Triggering mode on, TTL out and Triggering mode off, are given in the sketch.

In the PositionDistance mode, the motion direction turns around before the axis position reaches the end. The reference of the motion stage is set to the middle position of the motion range to eschew the erroneous TTL triggering output. This could bring a prolonged scanning duration. For a 100 X 100 scanning scheme, it could take more than 20 min to finish the entire scanning.

During the time, the optical properties of the high concentration oxy-/deoxy-hemoglobin dilutions in the phantom might have a chance to alter. To address this, the GCS command for the scanning scheme is modified, whereby major transmutations in the scanning mode and the triggering activation mode are made. Bi-directional scanning is first programmed to supersede the previously used single directional scanning (see Fig. 61). By doing this, the delay for the stage referencing during each skip (into the next line) is preserved. Additionally, the triggering activation between each move is omitted from the scanning to modify the efficiency of the GCS command read-in. By doing this, the scanning duration for i.e. a 100 X 100 scanning scheme can be reduced to 5 - 6 min[S2]. Also, the GCS command can be written as the DLL files, which are directly extracted by using MATLAB. By doing this, the default delay for reading the GCS commands through the software panel is saved. In the latest test for a 100 x 100 scanning scheme, the duration can be reduced to 2 - 3 min based on the set GCS coding.

Quality assurance and conformity rate

It is suggested to mass manufacture the optofluidic phantoms for the lab research rather than the elastofluidic phantoms, because the rigid PU matrices are better resistant to the fraction and more cost-efficient to prepare. The conformity rate of the optofluidic phantom fabrication should be considered and is influenced by the dimension of the microchannels, the recipe of the scatterers/absorbers, and subjectively by the operational skill during the fabrication. Tbl. 11 shows the conformity rate of the optofluidic phantom fabrication correlated to these factors. 150 phantoms are prepared to obtain enough pre-prepared parts for the statistical investigation of the conformity rate, and a conformity rate of 30% is finally recorded.

Table 11: Conformity rate correlated to the phantom recipe and the dimension of the microchannels in different fabrication stages are listed[P4].

	Phantom recipe	Microchannel size	Fabricate
Prepare mold ①		Dia. 50 μm: 17 / 20 Dia. 20 μm: 3 / 15	
Prepare PU slab ②	Caucasian: 73 / 100		
Embed mold			8 / 10
Drillg holes			6 / 8
Etch mold ③			3 / 6
Connect to pump			3 / 3
In total ④			3 / 10

It is noticed that producing a copper mold in the size of 20 - 30μm is challenging. The beam diameter of the ps-laser used is about 10μm and changes slightly in the actual work distance between the lens and the copper film surface. The changing laser beam kerf can cause a closed outline of the ablated mold compared to that of the DXF drawing. The mechanical air bubbles are created by stirring during the preparation of the viscous PU component. The generated air bubble is in a spherical size of 50μm to 1mm. To reduce the mechanical air bubbles, a vacuum autoclave is used to extract the air bubbles from the viscous PU component. The chemical (or reactive) air bubbles come from the solidification reaction of the 2-components polyurethane, where micro CO_2 bubbles are released when the PU touches with the water molecules around it. To address this problem, the solidification procedure is executed at 47 °C in a convection chamber (BINDER GmbH, Germany) to isolating the PU from the moisture.

Ethical permission: Attachment I, Application

FRIEDRICH-ALEXANDER
UNIVERSITÄT
ERLANGEN-NÜRNBERG

MEDIZINISCHE FAKULTÄT

Eingang
24. Okt. 2017
LPT Uni Erlangen

Ethik-Kommission der FAU • Krankenhausstr. 12 • 91054 Erlangen

Herrn
Prof. Dr.-Ing. Michael Schmidt
Lehrstuhl für Photonische Technologien
Konrad-Zuse-Straße 3-5
D-91052 Erlangen

Ethik-Kommission

Vorsitzender:
Prof. Dr. med. Renke Maas
Stellv. Vorsitzende:
Prof. Dr. med. Kerstin Amann

Geschäftsstelle:
Krankenhausstr. 12, 91054 Erlangen
Telefon: +49 9131 85-22270 (V. Kreiß)
+49 9131 85-26210 (R. Kauschke)
Fax: +49 9131 85-26021
E-Mail: ethikkommission@fau.de
Internet: www.ethikkommission.fau.de

Erlangen, 18.10.2017/VK

Antrag Nr.: **292_17 B** (bitte bei Schriftwechsel angeben)

Beratung gemäß § 2 Abs. (1) der Satzung

Studientitel:	Bestimmung der optischen Eigenschaften von menschlichem Hautgewebe mit Diffuse Reflectance Spectroscopy
Antragsteller:	Prof. Dr.-Ing. Michael Schmidt, Lehrstuhl für Photonische Technologien, Konrad-Zuse-Straße 3-5, D-91052 Erlangen

Sehr geehrter Herr Prof. Schmidt,

die Ethik-Kommission hat Ihren Antrag vom 26.09.2017 auf der Basis der Unterlagen in Anhang 1 geprüft und in der Sitzung am 10.10.2017 beraten.

Die Ethik-Kommission erhebt keine Einwände gegen die Durchführung der Studie.

Allerdings empfiehlt sie, folgende Hinweise zu beachten:

- Die Patienteninformation sollte dahingehend konkretisiert werden, dass das Risiko für den Studienteilnehmer nicht bekannt ist, anstelle, dass es keines gibt. Zudem sollte aufgenommen werden, dass ein Rücktritt von der Teilnahme jeder Zeit ohne Nachteile möglich ist.
- Im Studienprotokoll sollten veraltete Begriffe (mongolid) für die unterschiedlichen Hautfarben nicht mehr verwendet werden.
- Im Studienprotokoll sollten die ISO/DIN-Normen angeführt werden, aus den sich die Unbedenklichkeit der entsprechenden Lichtstrahlen ergibt.

Die Ethik-Kommission geht von einem rein wissenschaftlichen Projekt aus. Sollten die Daten für die Zertifizierung eines Medizinprodukts Verwendung finden bzw. für ein Konformitäts-Bewertungs-Verfahren in Deutschland verwendet werden, könnte sich ggf. die Einstufung der Studie ändern und die entsprechenden gesetzlichen Vorgaben zum Tragen kommen.

Der Ethik-Kommission sind ggf. geänderte Unterlagen in einfacher elektronischer Form vorzulegen. Hierbei ist darauf zu achten, dass mit den geänderten Unterlagen eine Version vorgelegt wird, aus der alle Änderungen (Streichungen/Änderungen/Ergänzungen) klar hervorgehen.

Allgemeine Hinweise:

FRIEDRICH-ALEXANDER
UNIVERSITÄT
ERLANGEN-NÜRNBERG

Auch bei einer positiven Beurteilung des Vorhabens durch die Ethik-Kommission der Medizinischen Fakultät der Friedrich-Alexander-Universität Erlangen-Nürnberg verbleibt die ärztliche und juristische Verantwortung für die Durchführung des Projekts uneingeschränkt bei Ihnen und Ihren Mitarbeitern/innen. Sollten sich zu diesem Projekt ethisch relevante Nachträge ergeben, bitte ich Sie, diese der Ethik-Kommission unverzüglich zusammen mit einer Bewertung der Nutzen-Risiko-Relation bekannt zu geben. Änderungen in den Dokumenten sind zum Zweck einer beschleunigten Bearbeitung deutlich zu kennzeichnen. Das Ende der Studie ist anzuzeigen und das Ergebnis zu gegebener Zeit in angemessener Form der Ethik-Kommission mitzuteilen.
Die Geschäftsstelle der Ethik-Kommission leitet folgende Daten des beratenen Antrags an eine Datenbank der Medizinischen Fakultät weiter: Antragsteller, Studientitel, Einrichtung, ggf. Sponsor und EudraCT-Nr. bzw. Eudamed-Nr. Dies erfolgt im Einklang mit dem Datenschutzgesetz und in Absprache mit dem örtlichen Datenschutzbeauftragten.

Die Gültigkeit des Votums der Ethik-Kommission ist an die im Antrag angegebene Laufzeit der Studie gebunden. Wird keine Laufzeit angegeben, ist die Gültigkeit des Votums auf fünf Jahre begrenzt.

Mit freundlichen Grüßen

Prof. Dr. med. Renke Maas
Vorsitzender der Ethik-Kommission

Anhang 1
Antrag vom 26.09.2017
1_Begleitschreiben.pdf
3_Datenschutzerklaerung.pdf
3_ICF_Erwachsene.pdf
4_Studienplan.pdf
4_Synopsis.pdf
5_Angaben zur Projektleitung.pdf
6_Zustimmung KD.pdf
Berufsrechtlicher+Antrag+-+27.09.2017.pdf

Anhang 2 - an der Beratung beteiligte EK-Mitglieder
Prof. Dr. Kerstin U. Amann, Frauenbeauftragte der Medizinischen Fakultät, Fachgebiet Pathologie, Leiterin der Nephropathologischen Abteilung
Dietmar Klieber, Vorsitzender Richter am OLG Nürnberg a.D.
Prof. Dr. Renke Maas, Vorsitzender der Ethik-Kommission, Fachgebiet Klinische Pharmakologie und Klinische Toxikologie, Institut für Experimentelle und Klinische Pharmakologie und Toxikologie
Prof. Dr. Dieter Harms, Fachgebiet Kinderheilkunde, ehem. Leitender Oberarzt an der Kinder- und Jugendklinik
Prof. Dr. Matthias Berking, Leiter des Instituts für Psychologie, Lehrstuhl für Klinische Psychologie und Psychotherapie
Dr. Eva-Maria Rüth, Fachgebiet Pädiatrie, Kinder- und Jugendklinik
Prof. Dr. Olaf Gefeller, Direktor des Instituts für Biometrie

Ethical permission: Attachment II, Technical info

An die Geschäftsstelle der
Ethik-Kommission
der Medizinischen Fakultät
der FAU Erlangen-Nürnberg
Krankenhausstr. 12
91054 Erlangen

Studienplan
an die Ethik-Kommission
der Medizinischen Fakultät

*Bitte **in deutscher Sprache** ausfüllen,*
Zutreffendes bitte ankreuzen.
Für multizentrische Studien mit Vorvotum einer nach Landesrecht gebildeten zuständigen Ethik-Kommission können Sie das verkürzte Antragsformular verwenden, abzurufen unter: http://www.ethik.med.uni-erlangen.de (Anschlussvotum)

Studientitel, Versionsnummer, Versionsdatum
Bestimmung der optischen Eigenschaften von menschlichem Hautgewebe mit *Diffuse Reflectance Spectroscopy*
Version: 2, Versionsdatum: 24. Okt. 2017

Zusammenfassung des Projekts (max. eine Seite)
Siehe Anhang (4_Synopsis)

Verantwortlichkeiten

1. Studienleiter/in

Name der/des verantwortlichen Studienleiterin/s:
Prof. Dr.-Ing. Michael Schmidt
Ordinarius des Lehrstuhls für Photonische Technologien (LPT) der FAU
Tel: 09131 85-23456
Fax: 09131 85-23234
E-Mail: : michael.schmidt@fau.de

Angaben über die Qualifikation der/des Studienleiterin/s:
Der Studienleiter ist durch seine langjährige Tätigkeit im Gebiet der photonischen Technologien vertraut und geschult im Umgang mit Lichtstrahlen.

Weitere Teilnehmer/innen vor Ort:

Chen Chen, M.Sc. [1,2], Doktorand Bereich photonische Medizintechnik

[1] SAOT (Erlangen Graduate School in Advanced Optical Technologies)
[2] LPT (Lehrstuhl für photonische Technologien der FAU)

Weitere Studienzentren (bei multizentrischen Studien): nein

2. ggf. beteiligte Einrichtungen (z.B. Labor, Bildgebung o.ä.)

Clinical Photonics Lab (CPL) des Lehrstuhls für Photonische Technologien (LPT) der FAU

3. Geldgeber

Lehrstuhls für Photonische Technologien (LPT) der FAU

Wissenschaftlicher Hintergrund

4. Hintergrund

Bei der Analyse von Hautläsionen, wie sie im Falle von Tumoren, Metastasen und dem paraneoplastischen Syndrom vorkommen, treten charakteristische Muster in der Vaskularisierung des Gewebes auf, die mit den gängigen Technologien wie der Auflichtmikroskope schwer darstellbar sind. Weiterhin ist die Gewebeoximetrie ein wichtiges Merkmal zur Charakterisierung einer Hypoxie und damit der Malignität eines Hauttumors. Hierfür wird ein multimodales bildgebendes Verfahren vorgeschlagen, welches anatomische und funktionale Bildgebung kombiniert und welches auf der Diffuse Reflectance Spectroscopy basiert. Es wird ein neuer Ansatz zur Messung der absoluten Werte der Oxy- und Deoxy-hämoglobinkonzentration untersucht. Dabei soll durch Einsatz einer gegabelten Lichtfaser, welche die Oberfläche abrastert, eine Auflösung von 50 µm erreicht werden. Im Rahmen des Humanversuchs soll eine in-vivo Messung der optischen Eigenschaften am Hautgewebe durchgeführt werden.

Studienziele

5. primäre/sekundäre Ziele und/oder Hypothesen

Durch die Möglichkeit einer nichtinvasiven optischen Biopsie von Hautläsionen kann die Diagnose von z. B. Melanomen sowie andere Hauterkrankung erleichtert werden. Das Ziel dieser Studie ist die Bestimmung der optischen Eigenschaften unterschiedlicher Hauttypen. Die Bestimmung der optischen Eigenschaften des Hautgewebes ist allgemein sinnvoll für alle Forschungsprojekte auf die biomedizinische Bildgebung. Es wird als den Übergang zwischen die Phantomstudien und die in-vivo Versuche behandelt.

6. konfirmatorisch/explorativ

Entfällt

Zielgrößen

7. primäre/sekundäre Zielgrößen

Eine Datenbank der optischen Eigenschaften (Absorptionskoeffizient μ_a und reduzierter Streukoeffizient μ_s') in Abhängigkeit unterschiedlicher Hautfarben wird erstellt.

Studiendesign

8. monozentrisch/multizentrisch

Bei dieser Studie handelt es sich um eine monozentrische Untersuchung.

9. Studienarme:

Zuerst wird eine Klassifikation der Personengruppen anhand der Hautfarbe durchgeführt. Die Hautfarbe wird mit dem Absorptionskoeffizient μ_a und dem reduzierten Streukoeffizient μ_s' korreliert. Hierfür wird die Fitzpatrick-Skala verwendet, wobei eine dunklere Hautfarbe einer höheren Fitzpatrick-Score entspricht. Die menschlichen Studienobjekte werden somit anhand der Fitzpatrick-Score gruppiert. Dieser Versuch ist als nichtinvasives Verfahren vorgesehen.
Bei weiteren Experimenten an menschlichen Studienobjekten werden die optischen Parameter μ_a und μ_s' des Hautgewebes (in-vivo) untersucht. In dieser Studie sollen die Messungen mithilfe einer fasergekoppelten Halogenlampe durchgeführt werden (die

Lichtfaser sieht Abb.1). Die Lichtfaser wird direkt in Kontakt zu der Hautoberfläche gebracht, sodass das schwache Licht (sichtbar bis nahes Infrarot) durch die Beleuchtungsfaser in die Haut eindringt. Das reflektierte Licht wird danach mit der Detektionsfaser gesammelt. Anhand der Abschwächung des reflektierten werden die optischen Parameter μ_a und μ_s' berechnet. Ein interner Vergleich dieser optischen Parameter zwischen den Personengruppen findet statt und es wird eine reguläre Berechnung des Primärprobenumfangs durchgeführt.

10. Randomisierung

Entfällt

11. Verblindung

Entfällt

12. graphische Darstellung des Studiendesigns

Experimentales Vorhaben:

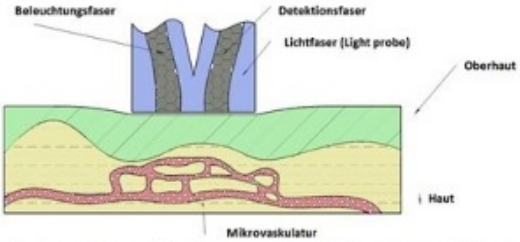

Abb. 1 Skizze des Hautgewebes mit einer zweischichtigen Geometrie, in die das Licht eindringt. Es sind die Epidermis (Oberhaut) und die Dermis (Haut) dargestellt.

Studienpopulation

13. Ein- und Ausschlusskriterien

Die Teilnehmer dürfen an keine Hauterkrankungen leiden. Hauterkrankungen sind ein Ausschlusskriterium. Ansonsten ist kein anderes Ausschluss Kriterium vorhanden.

14. Anzahl

Es soll verschiedene Personen (max. 50 Teilnehmer) untersucht werden, die nach ihrem Alter, Geschlecht sowie Hautfarbe gruppiert werden.

Alter: Jünger als 40 Jahre, älter als 20 Jahre
Geschlecht: möglichst 50% Männlich und 50% Weiblich

	1	10			19	28	
	2	11			20	29	
	3	12			21	30	
	4	13			22	31	
	5	14			23	32	
	6	15			24	33	
	7	16			25	34	
	8	17			26	35	
	9	18			27	36	

Abb. 2 Eine Tabelle der Hautfarbe nach dem Fitzpatrick-Score mit Farbcode. Die Personengruppen sind nach europäisch, asiatisch und indisch benannt. Hier würden wir die Personengruppen nach dem Fitzpatrick-Score mit der Hautfarbe korrelieren. Links ist der Fitzpatrick-Score dargestellt, wobei die Europäischen der Hautfarbe von Nummer 5 bis 15 entsprechen, die Asiatischen von 16 bis 25 und die Indischen von 26 bis 29.

Personengruppen: wenn möglich, 50% europäisch, 30% asiatisch und 20% indisch (siehe Abb. 2)

15. Rekrutierungswege und –maßnahmen

Mit Unterstützung von Prof. Dr. med. Maximilian Waldner (Medizin 1 der FAU, medizinischer Leiter des CPL) werden die Teilnehmer rekrutiert.

Studienablauf

16. Verfahren zur Aufklärung und Einholung der Einwilligung

Siehe Anhang (3_ICF_Erwachsene)

17. Maßnahmen

Bei dieser Studie handelt es sich um eine nichtinvasive Untersuchung. Die Lichtfaser wird jedoch direkt in Kontakt zur Hautoberfläche angebracht. Die Hygiene wird durch Hautreinigung (mit ärztlicher Waschlotion) und Reinigung der Lichtfaser (mit Ethanol 70%) sichergestellt.

18. Erfassung der Zielgrößen

Die ermittelten optischen Eigenschaften werden in einer Datenbank abgelegt und zusammengestellt. Die Datenbank wird später von der Software für die optische Biopsie verwendet.

19. zeitlicher Ablauf (Termine) und Studiendauer für den einzelnen Probanden/Patienten

Dauer der Studienteilnahme für den einzelnen Studienteilnehmer:
10 Tests pro Teilnehmer (ca. 1 Arbeitstag für jeden Teilnehmer)

20. Gesamtdauer der Studie

Geplanter Beginn der Studie: 01.01.2018
voraussichtliches Ende: 31.12.2019

Nutzen-Risiko-Abwägung (Sicherheitsaspekte)

21. alle studienbedingten Risiken

Die Messungen werden mit einer fasergekoppelten Halogenlampe (5 W, Ocean Optics) durchgeführt. Die Intensität am Faserausgang beträgt 1 – 2 mW/cm^2. Weiterhin wird das Licht aus der Faser ohne Fokussierung genutzt, sodass am Faserende die maximale Intensität vorliegt. Damit ist die genutzte Intensität weit unterhalb eines sonnigen Tages (ca. 70 mW/cm^2). Die Messungen finden hauptsächlich im Bereich von 500 bis 900 nm statt, um unter anderem Beschädigung des Hautgewebes durch blaues oder UV-Licht zu auszuschließen. Bei dieser Studie handelt es sich um die Messungen mit niedrigen Lichtintensitäten, sodass keine bekannten Risiken bestehen. Schmerzen, Unannehmlichkeiten oder Verletzungen der persönlichen sind auszuschließen. Hygienische Probleme aufgrund des Kontakts mit der Lichtleitfaser können durch Hautreinigung (vor und nach der Messung) abgelöst werden.

22. mit der Studie verbundener Nutzen

Bei der Studie handelt sich um eine Pilotstudie für die Untersuchung einer nichtinvasiven optischen Biopsie. Durch die Möglichkeit einer nichtinvasiven optischen Biopsie für Hautläsionen kann z. B. die Diagnose von Melanomen sowie andere Hauterkrankung erleichtert werde.

23. Abbruchkriterien (für den individuellen Teilnehmer bzw. für die gesamte Studie)

Entfällt

24. Statement zur ärztlichen Vertretbarkeit

Die Intensität am Faserende beträgt 1-2 mW/cm^2. Jede einzelne Messung dauert ca. 10 bis 30 Sekunden. Laut DIN-EN-62471 ist unter einer Intensität bis 10 mW/cm^2 eine Bestrahlungsdauer von ca. 10000 s sicher für die Netzhaut und eine Dauer von ca. 100000 s für das Hautgewebe. Es wird innerhalb einer gesamten Arbeitszeit von ca. 300 Sekunden keine photochemische oder thermische Wirkung in dem Hautgewebe induziert. Laut ANSI ist eine Intensität von 200 mW/cm^2 sicher fürs Hautgewebe. Die benutzte Lichtfaser ist leider nicht kontaktfrei. Die möglichen Hygieneprobleme können durch Hautreinigung (mit ärztlicher Waschlotion) und Reinigung der Lichtfaser (mit Ethanol 70%) gelöst werden. Deswegen ist das mögliche Risiko in Anbetracht der zu erwartenden Nutzung der Ansicht nach vertretbar.

Biometrie

25. konfirmatorische Studie: Fallzahlschätzung anhand der primären Zielgröße und der relevanten Effektstärke, geplante statistische Testverfahren

Entfällt

26. explorative Studie: Erläuterung zur statistischen Methodik, Begründung der gewählten Fallzahl

Entfällt

Datenmanagement und Datenschutz

27. Datenerfassung, -speicherung

Die medizinischen Ergebnisse unterliegen der ärztlichen Schweigepflicht, die dazu notwendigen Datenschutzbestimmungen beachtet werden.

anonymisiert/pseudonymisiert
Die medizinischen Ergebnisse werden anonymisiert gespeichert

28. Datenweitergabe

Bei dieser Studie wird eine vollständige Datenbank der optischen Eigenschaften (Absorptionskoeffizient und reduzierter Streukoeffizient) in Abhängigkeit unterschiedlicher Hautfarben erstellt. Die Datenbank wird später zur Programmierung des Algorithmus für die optische Biopsie verwendet.

29. Widerruf, Datenlöschung

Siehe Anhang (3_Datenschutzerklärung)

Umgang mit Biomaterialien

Entfällt

Probandenversicherung (sofern zutreffend)
Es wird zugunsten der Studienteilnehmer keine Versicherung abgeschlossen

Bitte überprüfen Sie anhand der folgenden Liste die Vollständigkeit der Anlagen zum Antrag:

- ☐ CV des/der Studienleiter/s/in (nur bei erstmaliger Antragstellung)
- ☐ Begleitschreiben
- ☐ Zusammenfassung des Antrags
- ☐ ~~Versicherungsnachweis (sofern zutreffend)~~
- ☐ Patienteninformation /für Erwachsene /~~für Jugendliche (sofern zutreffend) / für Kinder (sofern zutreffend) / für Betreuer (sofern zutreffend)~~
- ☐ Einwilligungserklärung ~~/ Zustimmungserklärung für Kinder u. Jugendliche (sofern zutreffend)~~
- ☐ Datenschutzrechtliche Einwilligungserklärung
- ☐ ~~Fragebögen (soweit zutreffend und soweit speziell für die Studie entwickelt)~~
- ☐ Unterschriftsblatt zum Antrag

Ethical permission: Attachment III, Patient info

Probandenaufklärung
Bestimmung der optischen Eigenschaften von menschlichem Hautgewebe mit Diffuse Reflectance Spectroscopy

Prof. Dr.-Ing. Michael Schmidt

Hintergrund der Studie

Bei der Analyse von Hautläsionen, wie sie im Falle von Tumoren, Metastasen und dem paraneoplastischen Syndrom vorkommen, treten charakteristische Muster in der Vaskularisierung des Gewebes auf, die mit den gängigen Technologien wie der Auflichtmikroskope schwer darstellbar sind. Weiterhin ist die Gewebeoximetrie ein wichtiges Merkmal zur Charakterisierung einer Hypoxie und damit der Malignität eines Hauttumors. Hierfür wird ein multimodales bildgebendes Verfahren vorgeschlagen, welches anatomische und funktionale Bildgebung kombiniert und welches auf der Diffuse Reflectance Spectroscopy basiert. Es wird ein neuer Ansatz zur Messung der absoluten Werte der Oxy- und Deoxy-hämoglobinkonzentration untersucht. Es soll durch Einsatz einer gegabelten Lichtfaser, die die Oberfläche abrastert, eine Auflösung von 50 µm erreicht werden. Im Rahmen des Humanversuchs soll eine in-vivo Messung der optischen Eigenschaften am Hautgewebe durchgeführt werden.

Ziele der Studie

Das Ziel dieser Studie ist zur Bestimmung der optischen Eigenschaften unterschiedlicher Hautfarben.

Methoden der Studie

Die Messungen werden mit einer fasergekoppelten Halogenlampe (5W, Ocean Optics) durchgeführt. Die Intensität am Faserausgang beträgt 1 – 2 mW/cm^2. Weiterhin wird das Licht aus der Faser ohne Fokussierung genutzt, sodass am Faserende die maximale Intensität vorliegt. Damit ist die genutzte Intensität weit unterhalb eines sonnigen Tages (ca. 70 mW/cm^2). Die Messungen finden hauptsächlich im Bereich von 500 bis 900 nm statt, um unter anderem Beschädigung des Hautgewebes durch blaues oder UV-Licht zu auszuschließen.

Nutzen und Risiko der Studie

Es handelt sich um die Messungen mit niedrigen Lichtintensitäten. Laut DIN-EN-62471 ist unter einer Intensität bis 10 mW/cm^2 eine Bestrahlungsdauer von ca. 100000 s sicher für das Hautgewebe. Schmerzen, Unannehmlichkeiten oder Verletzungen der persönlichen sind auszuschließen. Hygienische Probleme aufgrund des Kontakts mit der Lichtleitfaser könne durch Hautreinigung (vor und nach der Messung) abgelöst werden.

Bekannte und möglicherweise zu erwartende Wirkungen und Nebenwirkungen von Medikamenten

Es werden keine Medikamente verabreicht.

Widerruflichkeit einer Einwilligung

Die Einwilligung kann jederzeit widerrufen werden. Ein Rücktritt von der Teilnahme ist jeder Zeit ohne Nachteile möglich

Probandenversicherung

Da keine Medikamente verabreicht und lediglich non-invasive optische Messungen durchgeführt werden, erfolgt keine Probandenversicherung.

Name und Telefon des Ansprechpartners vor Ort

Chen Chen, Doktorand Bereich photonische Medizintechnik, Tel: 09131 85-23242

Ich weiß, daß auch bei einer positiven Beurteilung des Vorhabens durch die Ethik-Kommission der Medizinischen Fakultät der FAU Erlangen-Nürnberg die ärztliche und juristische Verantwortung für die Durchführung des Projektes uneingeschränkt bei der Leiterin/dem Leiter verbleibt.

Erlangen/~~Nürnberg~~

Datum 06.09.2017

Unterschrift des/der Antragstellers/in

Prof. Dr.-Ing. Michael Schmidt

(Name in Druckbuchstaben)

Unterschrift der/des Leiterin/Leiters der Einrichtung, in der das Vorhaben durchgeführt werden soll.
Mit der Durchführung des Forschungsvorhabens einverstanden:

Datum 06.09.2017

Prof. Dr.-Ing. Michael Schmidt

(Name in Druckbuchstaben)

Ethical permission: Attachment III, Patient agreement

Einverständnis

Hiermit erkläre ich -

Chang Chun (Name des Probanden) Fang (Vorname des Probanden) 25.12.1986 (geb.)

- mich einverstanden bei der Studie

Bestimmung der optischen Eigenschaften vom menschlichen Hautgewebe mit der Diffuse Reflectance Spectroscopy

als Proband mitzuwirken. Ich bestätige, dass ich keine Erkrankung bzw. Beschwerden (z.B. Allergie, Neurodermitis, Ekzem, Schuppenflechte, Nesselsucht, Tumoren) der Haut leide.

Erlangen, den 26.01.2018 Unterschrift 方长春

Einverständnis

Hiermit erkläre ich -

CHEN CHEN 28.05.1988

Name des Probanden Vorname des Probanden geb.

- mich einverstanden bei der Studie

Bestimmung der optischen Eigenschaften vom menschlichen Hautgewebe mit der Diffuse Reflectance Spectroscopy

als Proband mitzuwirken. Ich bestätige, dass ich keine Erkrankung bzw. Beschwerden (z.B. Allergie, Neurodermitis, Ekzem, Schuppenflechte, Nesselsucht, Tumoren) der Haut leide.

Erlangen, den 27.01.2018 Unterschrift

Ethical permission: Attachment III, Data privacy

Datenschutzrechtliche Einwilligungserklärung
Bestimmung der optischen Eigenschaften von menschlichem Hautgewebe mit Diffuse Reflectance Spectroscopy

Prof. Dr.-Ing. Michael Schmidt

Hiermit bin ich -

Chang Chun (Name des Probanden) Tony (Vorname des Probanden) 25.12.1986 (geb.)

damit einverstanden, dass die einleitend genannte Person bzw. ein Mitarbeiter des Lehrstuhls für Photonische Technologien Einblick in meine Daten einschließlich der Daten über Gesundheitszustand, Krankengeschichte, Geschlecht, Alter, Gewicht, Körpergröße usw., falls für die Studie erforderlich, nimmt. Ich stimme zu, dass Daten, die meine Person betreffen, unter der Verantwortung der oben genannten Institution in verschlüsselter Form für Studien gespeichert und verarbeitet werden.

Widerruf der Zustimmung zur Datenverwendung
Ich weiß, dass ich meine Zustimmung zur Verwendung meiner Daten jederzeit und ohne Angabe von Gründen gegenüber der einleitend genannten Institution bzw. Person widerrufen kann und dass dies keinen Einfluss auf meine etwaige weitere ärztliche Behandlung hat. Im Falle des Widerrufs bin ich damit einverstanden, dass meine Daten zu Kontrollzwecken weiterhin gespeichert bleiben. Ich habe jedoch das Recht, deren Löschung zu verlangen, sofern gesetzliche Bestimmungen der Löschung nicht entgegenstehen. Ich bin mir bewusst, dass im Falle einer anonymisierten Speicherung meiner Daten deren Löschung auf meinen Wunsch nicht möglich ist.

Erlangen, den 26.01.2016 Unterschrift [signature]

Datenschutzrechtliche Einwilligungserklärung
Bestimmung der optischen Eigenschaften von menschlichem Hautgewebe mit Diffuse Reflectance Spectroscopy

Prof. Dr.-Ing. Michael Schmidt

Hiermit bin ich -

CHEN CHEN 28.05.1988
Name des Probanden Vorname des Probanden geb.

damit einverstanden, dass die einleitend genannte Person bzw. ein Mitarbeiter des Lehrstuhls für Photonische Technologien Einblick in meine Daten einschließlich der Daten über Gesundheitszustand, Krankengeschichte, Geschlecht, Alter, Gewicht, Körpergröße usw., falls für die Studie erforderlich, nimmt. Ich stimme zu, dass Daten, die meine Person betreffen, unter der Verantwortung der oben genannten Institution in verschlüsselter Form für Studien gespeichert und verarbeitet werden.

Widerruf der Zustimmung zur Datenverwendung
Ich weiß, dass ich meine Zustimmung zur Verwendung meiner Daten jederzeit und ohne Angabe von Gründen gegenüber der einleitend genannten Institution bzw. Person widerrufen kann und dass dies keinen Einfluss auf meine etwaige weitere ärztliche Behandlung hat. Im Falle des Widerrufs bin ich damit einverstanden, dass meine Daten zu Kontrollzwecken weiterhin gespeichert bleiben. Ich habe jedoch das Recht, deren Löschung zu verlangen, sofern gesetzliche Bestimmungen der Löschung nicht entgegenstehen. Ich bin mir bewusst, dass im Falle einer anonymisierten Speicherung meiner Daten deren Löschung auf meinen Wunsch nicht möglich ist.

Erlangen, den 27.01.2018 Unterschrift

Bibliography

[1] Sadowski, T. ; Klose, C. ; Gerl, M. J. ; Wójcik-Maciejewicz, A. ; Herzog, R. ; Simons, K. ; Reich, A. ; Surma, M. A.: Large-scale human skin lipidomics by quantitative, high-throughput shotgun mass spectrometry. In: *Scientific Reports* 7 (2017), S. 43761

[2] Morgner, U. ; Li, W. D. X. ; Pitris, C. ; Fujimoto, J.: Spectroscopic optical coherence tomography. In: *Optics letters* 25 (2000), Nr. 2, S. 111–113

[3] Beard, P.: Biomedical photoacoustic imaging. In: *Interface focus* (2011), S. rsfs20110028

[4] Han, J. H. ; Moon, Y. ; Lee, J. J. ; Choi, S. ; Kim, Y.-C. ; Jeong, S.: Differentiation of cutaneous melanoma from surrounding skin using laser-induced breakdown spectroscopy. In: *Biomedical optics express* 7 (2016), Nr. 1, S. 57–66

[5] Förster, M. ; Bolzinger, M.-A. ; Montagnac, G. ; Briançon, S.: Confocal Raman microspectroscopy of the skin. In: *European Journal of Dermatology* 21 (2012), Nr. 6, S. 851–863

[6] Beard, P. C.: Photoacoustic imaging of blood vessel equivalent phantoms. In: *International Symposium on Biomedical Optics* International Society for Optics and Photonics, 2002, S. 54–62

[7] Bykov, A. V. ; Popov, A. P. ; Priezzhev, A. V. ; Myllylä, R.: Multilayer tissue phantoms with embedded capillary system for OCT and DOCT imaging. In: *European Conference on Biomedical Optics* Optical Society of America, 2011, S. 80911R

[8] L.Daniel ; K.Yoko ; C., B. ; Shuichi, T.: Fabrication of microfluidic mixers and artificial vasculatures using a high-brightness diode-pumped Nd: YAG laser direct write method. In: *Lab on a Chip* 3 (2003), Nr. 4, S. 318–323

[9] Melania, P. ; Andrea, F. ; Pasquale, M. ; Pietro, F.: Microscopy imaging and quantitative phase contrast mapping in turbid microfluidic channels by digital holography. In: *Lab Chip* 12 (2012), Nr. 17, S. 3073–3076

[10] B, P. A. ; Gyu, S. W. ; Zhang, X. ; Dunn, A.: Laser speckle contrast imaging of flow in a microfluidic device. In: *Biomedical Optics (BiOS) 2007* International Society for Optics and Photonics, 2007, S. 644604–644604

[11] Konecky, S. ; Choe, R.: Comparison of diffuse optical tomography of human breast with whole-body and breast-only positron emission tomography. In: *Medical physics* 35 (2008), S. 446

[12] Hillman, E. ; Devor, A. ; Dunn, A. ; Boas, D.: Laminar optical tomography: high-resolution 3D functional imaging of superficial tissues. In: *Medical Imaging* International Society for Optics and Photonics, 2006, S. 61431M–61431M

[13] Kanawade, R. ; Sayko, G. ; Schmidt, M. ; Douplik, A.: In vivo monitoring of vessel density pattern in skin phantoms for the application of early sign of shock detection by using diffuse reflectance spectroscopy. In: *Advanced Biomedical and Clinical Diagnostic Systems IX* Bd. 7890 International Society for Optics and Photonics, 2011, S. 789009

[14] Singh, M. K. A.: Identification and elimination of reflection artifacts in biomedical photoacoustic imaging. (2016)

[15] MC, H. E. ; Anna, D. ; K, D. A. ; A, B. D.: Laminar optical tomography: high-resolution 3D functional imaging of superficial tissues. In: *Medical Imaging* International Society for Optics and Photonics, 2006, S. 61431M–61431M

[16] Royston, D. D. ; Poston, R. S. ; Prahl, S. A.: Optical properties of scattering and absorbing materials used in the development of optical phantoms at 1064 nm. In: *Journal of biomedical optics* 1 (1996), Nr. 1, S. 110–116

[17] Bashkatov, A. N. ; Genina, E. A. ; Tuchin, V. V.: Optical properties of skin, subcutaneous, and muscle tissues: a review. In: *Journal of Innovative Optical Health Sciences* 4 (2011), Nr. 01, S. 9–38

[18] Prahl, S. A. ; Gemert, M. J. ; Welch, A. J.: Determining the optical properties of turbid media by using the adding–doubling method. In: *Applied optics* 32 (1993), Nr. 4, S. 559–568

[19] Guy, L. ; F, K. B. ; D, S. D.: Review of tissue simulating phantoms with controllable optical, mechanical and structural properties for use in optical coherence tomography. In: *Biomedical optics express* 3 (2012), Nr. 6, S. 1381–1398

[20] Nischal, U. ; Nischal, K. ; Khopkar, U.: Techniques of skin biopsy and practical considerations. In: *Journal of cutaneous and aesthetic surgery* 1 (2008), Nr. 2, S. 107

[21] Ranjan, R. ; Singh, L. ; Arava, S. K. ; Singh, M. K.: Margins in skin excision biopsies: Principles and guidelines. In: *Indian journal of dermatology* 59 (2014), Nr. 6, S. 567

[22] Carboni, I. ; Specchio, F. ; Nisticò, S. ; Campione, E. ; Bavetta, M. ; Dianzani, C. ; Chimenti, S. ; Ambrogi, V.: Skin Lesion: unexpected uptake PET/CT. In: *Journal of Clinical & Experimental Dermatology Research* 2015 (2015)

[23] Louie, D. C. ; Tchvialeva, L. ; Lee, T. K.: Proof of principle of a stokes polarimetry probe for skin lesion evaluation. In: *Student Conference (ISC), 2016 IEEE EMBS International* IEEE, 2016, S. 1–4

[24] Folkman, J.: Angiogenesis in cancer, vascular, rheumatoid and other disease. In: *Nature medicine* 1 (1995), Nr. 1, S. 27–30

[25] Caspers, P. ; Lucassen, G. ; Puppels, G.: Combined in vivo confocal Raman spectroscopy and confocal microscopy of human skin. In: *Biophysical journal* 85 (2003), Nr. 1, S. 572–580

[26] Zhen, Y. ; Qizhi, Z. ; Huabei, J.: Simultaneous reconstruction of acoustic and optical properties of heterogeneous media by quantitative photoacoustic tomography. In: *Optics express* 14 (2006), Nr. 15, S. 6749–6754

[27] Sun, Q. ; Tran, M. ; Smith, B. W. ; Winefordner, J. D.: Zinc analysis in human skin by laser induced-breakdown spectroscopy. In: *Talanta* 52 (2000), Nr. 2, S. 293–300

[28] Elodie, S. ; Coleman, M. ; Pietro, M. ; Dino, D.: Rapid prototyping polymers for microfluidic devices and high pressure injections. In: *Lab on a Chip* 11 (2011), Nr. 22, S. 3752–3765

[29] Tuchin, V. ; Bashkatov, A. ; Oh, H. u. a.: Finger tissue model and blood perfused skin tissue phantom. In: *SPIE BiOS* International Society for Optics and Photonics, 2011, S. 78980Z–78980Z

[30] Wang, J. ; Ghassemi, P. ; Pfefer, J.: 3D printed biomimetic vascular phantoms for assessment of hyperspectral imaging systems. In: *SPIE BiOS* International Society for Optics and Photonics, 2015, S. 932508–932508

[31] Larry, K. ; Gadi, W. ; S, S. J.: Spectral oximetry assessed with high-speed ultra-high-resolution optical coherence tomography. In: *Journal of biomedical optics* 12 (2007), Nr. 4, S. 041212–041212

[32] Sri-Rajasekhar, K. ; Lihong, W.: Ultrasound-modulated optical microscopy. In: *Journal of biomedical optics* 13 (2008), Nr. 5, S. 054046–054046

[33] Pogue, B. W. ; Patterson, M. S.: Review of tissue simulating phantoms for optical spectroscopy, imaging and dosimetry. In: *Journal of biomedical optics* 11 (2006), Nr. 4, S. 041102–041102

[34] Sia, S. K. ; Whitesides, G. M.: Microfluidic devices fabricated in poly (dimethylsiloxane) for biological studies. In: *Electrophoresis* 24 (2003), Nr. 21, S. 3563–3576

[35] Folkman, J.: Angiogenesis in cancer, vascular, rheumatoid and other disease. In: *Nature medicine* 1 (1995), Nr. 1, S. 27–30

[36] J, S. P. ; Beasley, G. ; Betty, J. ; S, T.: Hypoxia in melanoma: using optical spectroscopy and EF5 to assess tumor oxygenation before and during regional chemotherapy for melanoma. In: *Annals of surgical oncology* 21 (2014), Nr. 5, S. 1435–1440

[37] Finlay, J. ; Foster, T.: Hemoglobin oxygen saturations in phantoms and in vivo from measurements of steady-state diffuse reflectance at a single, short source-detector separation. In: *Medical physics* 31 (2004), S. 1949

[38] Tromberg, B. ; Cerussi, A. ; Shah, N. ; Durkin, A. ; Hsiang, D. ; Butler, J. ; Mehta, R.: Imaging in breast cancer: diffuse optics in breast cancer: detecting tumors in pre-menopausal women and monitoring neoadjuvant chemotherapy. In: *Breast Cancer Research* 7 (2005), Nr. 6, S. 279

[39] Durduran, T. ; Durning, C. Z. S. ; Mason, S.: Optical measurement of cerebral hemodynamics and oxygen metabolism in neonates with congenital heart defects. In: *Journal of biomedical optics* 15 (2010), Nr. 3, S. 037004–037004

[40] Boas, D. ; Brooks, D. ; Miller, E. ; Marzio, C. D. ; Kilmer, M. ; R.J.Gaudette ; Zhang, Q.: Imaging the body with diffuse optical tomography. In: *Signal Processing Magazine, IEEE* 18 (2001), Nr. 6, S. 57–75

[41] P, N. K. ; Lu, Z. ; J, S. J. ; Knut, S. ; Johan, M.: The optics of human skin: Aspects important for human health. In: *Nor. Acad. Sci. Lett* 2008 (2008), S. 35–46

[42] Madsen, S. J. ; Wyss, P. ; Tromberg, B. J.: Determination of the optical properties of the human uterus using frequency-domain photon migration and steady-state techniques. In: *Physics in medicine and biology* 39 (1994), Nr. 8, S. 1191

[43] Jacques, S. L.: Optical properties of biological tissues: a review. In: *Physics in medicine and biology* 58 (2013), Nr. 11, S. R37

[44] Tom, L. ; A, W. P. ; H, C. P.: Optical properties of human skin. In: *Journal of biomedical optics* 17 (2012), Nr. 9, S. 0909011–09090115

[45] Sheng-Hao, T. ; Alexander, G. ; J, D. A.: In vivo determination of skin near-infrared optical properties using diffuse optical spectroscopy. In: *Journal of biomedical optics* 13 (2008), Nr. 1, S. 014016–014016

[46] Strangman, G. ; Franceschini, M. ; Boas, D.: Factors affecting the accuracy of near-infrared spectroscopy concentration calculations for focal changes in oxygenation parameters. In: *Neuroimage* 18 (2003), Nr. 4, S. 865–879

[47] Talukdar, T. ; Moore, J. ; Diamond, S.: Continuous correction of differential path length factor in near-infrared spectroscopy. In: *Journal of biomedical optics* 18 (2013), Nr. 5, S. 056001–056001

[48] Draghici, A. E. ; Potart, D. ; Hollmann, J. L. ; Pera, V. ; Fang, Q. ; DiMarzio, C. A. ; Andrew Taylor, J. ; Niedre, M. J. ; Shefelbine, S. J.: Near infrared spectroscopy for measuring changes in bone hemoglobin content after exercise in individuals with spinal cord injury. In: *Journal of Orthopaedic Research®* 36 (2018), Nr. 1, S. 183–191

[49] Zell, K. ; Sperl, J. ; Vogel, M. ; Niessner, R. ; Haisch, C.: Acoustical properties of selected tissue phantom materials for ultrasound imaging. In: *Physics in medicine and biology* 52 (2007), Nr. 20, S. N475

[50] Dabrowski, W. ; Dunmore-Buyze, J. ; Rankin, R. ; Holdsworth, D. ; Fenster, A.: A real vessel phantom for imaging experimentation. In: *Medical physics* 24 (1997), Nr. 5, S. 687–693

[51] Raheel, S. ; J, S. H. ; Fangxiang, J. ; Johnson, C. R. ; Gale, B. K.: Fabrication of a MRI Standardization Device From Stacking Highly Patterned Thin PDMS Layers. (2010)

[52] Kim, M. ; Durduran, T. ; Frangos, S. ; Edlow, B. ; Buckley, E. ; Moss, H. ; Choe, R.: Noninvasive measurement of cerebral blood flow and blood oxygenation using near-infrared and diffuse correlation spectroscopies in critically brain-injured adults. In: *Neurocritical care* 12 (2010), Nr. 2, S. 173–180

[53] Robles, F. ; Chowdhury, S. ; Wax, A.: Assessing hemoglobin concentration using spectroscopic optical coherence tomography for feasibility of tissue diagnostics. In: *Biomedical optics express* 1 (2010), Nr. 1, S. 310–317

Own publications referring to this work

[P1] Chen, C., Ahmed, M., Häfner, T., Klämpfl, F., Stelzle, F., & Schmidt, M.: Fabrication of a turbid optofluidic phantom device with tunable μ_a and μ_s' to simulate cutaneous vascular perfusion. In: Scientific reports (2016), Nr. 6, 30567.

[P2] Chen, C., Ahmed, M., Klämpfl, F., Stelzle, F., & Schmidt, M.: A novel microfluidic model to mimic the turbid nature and microvasculature of cutaneous tissue for optical imaging experiments. In: Biophotonics Japan (2015), Vol. 9792, p. 97920J. International Society for Optics and Photonics.

[P3] Chen, C., Klämpfl, F., Kanawade, R., Riemann, M., Knipfer, C., Stelzle, F., & Schmidt, M.: Recovering the superficial microvascular pattern via diffuse reflection imaging: phantom validation. In: Biomedical engineering online (2015), Nr. 14(1), 87.

[P4] Chen, C., Klämpfl, F., Knipfer, C., Riemann, M., Kanawade, R., Stelzle, F., & Schmidt, M.: Preparation of a skin equivalent phantom with interior micron-scale vessel structures for optical imaging experiments. In: Biomedical optics express (2014), Nr. 5(9), 3140-3149.

[P5] Chen, C., Klämpfl, F., Stelzle, F., & Schmidt, M.: Mapping the microvascular and the associated absolute values of oxy-hemoglobin concentration through turbid media via local off-set diffuse optical imaging. In: Optics in Health Care and Biomedical Optics VI (2014), Vol. 9268, p. 92680V. International Society for Optics and Photonics.

Students' theses referring to this work

[S1] Ahmed, M.: Fabrication of a microfluidic based phantom to mimick the microvasculature of human skin. Master thesis. 2014. LPT -Erlangen

[S2] Mulugeta Kumneger D.: Modify scanning scheme and imaging reconstruction based on MATLAB and GSC language. Master thesis. 2014. LPT -Erlangen

Reihenübersicht

Koordination der Reihe (Stand 2021):
Geschäftsstelle Maschinenbau, Dr.-Ing. Oliver Kreis, www.mb.fau.de/diss/

Im Rahmen der Reihe sind bisher die nachfolgenden Bände erschienen.

Band 1 – 52
Fertigungstechnik – Erlangen
ISSN 1431-6226
Carl Hanser Verlag, München

Band 53 – 307
Fertigungstechnik – Erlangen
ISSN 1431-6226
Meisenbach Verlag, Bamberg

ab Band 308
FAU Studien aus dem Maschinenbau
ISSN 2625-9974
FAU University Press, Erlangen

Die Zugehörigkeit zu den jeweiligen Lehrstühlen ist wie folgt gekennzeichnet:

Lehrstühle:

FAPS	Lehrstuhl für Fertigungsautomatisierung und Produktionssystematik
FMT	Lehrstuhl für Fertigungsmesstechnik
KTmfk	Lehrstuhl für Konstruktionstechnik
LFT	Lehrstuhl für Fertigungstechnologie
LPT	Lehrstuhl für Photonische Technologien
REP	Lehrstuhl für Ressourcen- und Energieeffiziente Produktionsmaschinen

Band 1: Andreas Hemberger
Innovationspotentiale in der rechnerintegrierten Produktion durch wissensbasierte Systeme
FAPS, 208 Seiten, 107 Bilder. 1988.
ISBN 3-446-15234-2.

Band 2: Detlef Classe
Beitrag zur Steigerung der Flexibilität automatisierter Montagesysteme durch Sensorintegration und erweiterte Steuerungskonzepte
FAPS, 194 Seiten, 70 Bilder. 1988.
ISBN 3-446-15529-5.

Band 3: Friedrich-Wilhelm Nolting
Projektierung von Montagesystemen
FAPS, 201 Seiten, 107 Bilder, 1 Tab. 1989.
ISBN 3-446-15541-4.

Band 4: Karsten Schlüter
Nutzungsgradsteigerung von Montagesystemen durch den Einsatz der Simulationstechnik
FAPS, 177 Seiten, 97 Bilder. 1989.
ISBN 3-446-15542-2.

Band 5: Shir-Kuan Lin
Aufbau von Modellen zur Lageregelung von Industrierobotern
FAPS, 168 Seiten, 46 Bilder. 1989.
ISBN 3-446-15546-5.

Band 6: Rudolf Nuss
Untersuchungen zur Bearbeitungsqualität im Fertigungssystem Laserstrahlschneiden
LFT, 206 Seiten, 115 Bilder, 6 Tab. 1989.
ISBN 3-446-15783-2.

Band 7: Wolfgang Scholz
Modell zur datenbankgestützten Planung automatisierter Montageanlagen
FAPS, 194 Seiten, 89 Bilder. 1989.
ISBN 3-446-15825-1.

Band 8: Hans-Jürgen Wißmeier
Beitrag zur Beurteilung des Bruchverhaltens von Hartmetall-Fließpreßmatrizen
LFT, 179 Seiten, 99 Bilder, 9 Tab. 1989.
ISBN 3-446-15921-5.

Band 9: Rainer Eisele
Konzeption und Wirtschaftlichkeit von Planungssystemen in der Produktion
FAPS, 183 Seiten, 86 Bilder. 1990.
ISBN 3-446-16107-4.

Band 10: Rolf Pfeiffer
Technologisch orientierte Montageplanung am Beispiel der Schraubtechnik
FAPS, 216 Seiten, 102 Bilder, 16 Tab. 1990.
ISBN 3-446-16161-9.

Band 11: Herbert Fischer
Verteilte Planungssysteme zur Flexibilitätssteigerung der rechnerintegrierten Teilefertigung
FAPS, 201 Seiten, 82 Bilder. 1990.
ISBN 3-446-16105-8.

Band 12: Gerhard Kleineidam
CAD/CAP: Rechnergestützte Montagefeinplanung
FAPS, 203 Seiten, 107 Bilder. 1990.
ISBN 3-446-16112-0.

Band 13: Frank Vollertsen

Pulvermetallurgische Verarbeitung eines übereutektoiden verschleißfesten Stahls

LFT, XIII u. 217 Seiten, 67 Bilder, 34 Tab. 1990. ISBN 3-446-16133-3.

Band 14: Stephan Biermann

Untersuchungen zur Anlagen- und Prozeßdiagnostik für das Schneiden mit CO_2-Hochleistungslasern

LFT, VIII u. 170 Seiten, 93 Bilder, 4 Tab. 1991. ISBN 3-446-16269-0.

Band 15: Uwe Geißler

Material- und Datenfluß in einer flexiblen Blechbearbeitungszelle

LFT, 124 Seiten, 41 Bilder, 7 Tab. 1991.

ISBN 3-446-16358-1.

Band 16: Frank Oswald Hake

Entwicklung eines rechnergestützten Diagnosesystems für automatisierte Montagezellen

FAPS, XIV u. 166 Seiten, 77 Bilder. 1991.

ISBN 3-446-16428-6.

Band 17: Herbert Reichel

Optimierung der Werkzeugbereitstellung durch rechnergestützte Arbeitsfolgenbestimmung

FAPS, 198 Seiten, 73 Bilder, 2 Tab. 1991.

ISBN 3-446-16453-7.

Band 18: Josef Scheller

Modellierung und Einsatz von Softwaresystemen für rechnergeführte Montagezellen

FAPS, 198 Seiten, 65 Bilder. 1991.

ISBN 3-446-16454-5.

Band 19: Arnold vom Ende

Untersuchungen zum Biegeumforme mit elastischer Matrize

LFT, 166 Seiten, 55 Bilder, 13 Tab. 1991. ISBN 3-446-16493-6.

Band 20: Joachim Schmid

Beitrag zum automatisierten Bearbeiten von Keramikguß mit Industrierobotern

FAPS, XIV u. 176 Seiten, 111 Bilder, 6 Tab. 1991. ISBN 3-446-16560-6.

Band 21: Egon Sommer

Multiprozessorsteuerung für kooperierende Industrieroboter in Montagezellen

FAPS, 188 Seiten, 102 Bilder. 1991.

ISBN 3-446-17062-6.

Band 22: Georg Geyer

Entwicklung problemspezifischer Verfahrensketten in der Montage

FAPS, 192 Seiten, 112 Bilder. 1991.

ISBN 3-446-16552-5.

Band 23: Rainer Flohr

Beitrag zur optimalen Verbindungstechnik in der Oberflächenmontage (SMT)

FAPS, 186 Seiten, 79 Bilder. 1991.

ISBN 3-446-16568-1.

Band 24: Alfons Rief

Untersuchungen zur Verfahrensfolge Laserstrahlschneiden und -schweißen in der Rohkarosseriefertigung

LFT, VI u. 145 Seiten, 58 Bilder, 5 Tab. 1991. ISBN 3-446-16593-2.

Band 25: Christoph Thim
Rechnerunterstützte Optimierung von Materialflußstrukturen in der Elektronikmontage durch Simulation
FAPS, 188 Seiten, 74 Bilder. 1992.
ISBN 3-446-17118-5.

Band 26: Roland Müller
CO_2 -Laserstrahlschneiden von kurzglasverstärkten Verbundwerkstoffen
LFT, 141 Seiten, 107 Bilder, 4 Tab. 1992.
ISBN 3-446-17104-5.

Band 27: Günther Schäfer
Integrierte Informationsverarbeitung bei der Montageplanung
FAPS, 195 Seiten, 76 Bilder. 1992.
ISBN 3-446-17117-7.

Band 28: Martin Hoffmann
Entwicklung einer CAD/CAM-Prozeßkette für die Herstellung von Blechbiegeteilen
LFT, 149 Seiten, 89 Bilder. 1992.
ISBN 3-446-17154-1.

Band 29: Peter Hoffmann
Verfahrensfolge Laserstrahlschneiden und –schweißen: Prozeßführung und Systemtechnik in der 3D-Laserstrahlbearbeitung von Blechformteilen
LFT, 186 Seiten, 92 Bilder, 10 Tab. 1992.
ISBN 3-446-17153-3.

Band 30: Olaf Schrödel
Flexible Werkstattsteuerung mit objektorientierten Softwarestrukturen
FAPS, 180 Seiten, 84 Bilder. 1992.
ISBN 3-446-17242-4.

Band 31: Hubert Reinisch
Planungs- und Steuerungswerkzeuge zur impliziten Geräteprogrammierung in Roboterzellen
FAPS, XI u. 212 Seiten, 112 Bilder. 1992.
ISBN 3-446-17380-3.

Band 32: Brigitte Bärnreuther
Ein Beitrag zur Bewertung des Kommunikationsverhaltens von Automatisierungsgeräten in flexiblen Produktionszellen
FAPS, XI u. 179 Seiten, 71 Bilder. 1992.
ISBN 3-446-17451-6.

Band 33: Joachim Hutfless
Laserstrahlregelung und Optikdiagnostik in der Strahlführung einer CO_2-Hochleistungslaseranlage
LFT, 175 Seiten, 70 Bilder, 17 Tab. 1993.
ISBN 3-446-17532-6.

Band 34: Uwe Günzel
Entwicklung und Einsatz eines Simulationsverfahrens für operative und strategische Probleme der Produktionsplanung und –steuerung
FAPS, XIV u. 170 Seiten, 66 Bilder, 5 Tab. 1993. ISBN 3-446-17604-7.

Band 35: Bertram Ehmann
Operatives Fertigungscontrolling durch Optimierung auftragsbezogener Bearbeitungsabläufe in der Elektronikfertigung
FAPS, XV u. 167 Seiten, 114 Bilder. 1993.
ISBN 3-446-17658-6.

Band 36: Harald Kolléra
Entwicklung eines benutzerorientierten Werkstattprogrammiersystems für das Laserstrahlschneiden
LFT, 129 Seiten, 66 Bilder, 1 Tab. 1993.
ISBN 3-446-17719-1.

Band 37: Stephanie Abels
Modellierung und Optimierung von Montageanlagen in einem integrierten Simulationssystem
FAPS, 188 Seiten, 88 Bilder. 1993.
ISBN 3-446-17731-0.

Band 38: Robert Schmidt-Hebbel
Laserstrahlbohren durchflußbestimmender Durchgangslöcher
LFT, 145 Seiten, 63 Bilder, 11 Tab. 1993.
ISBN 3-446-17778-7.

Band 39: Norbert Lutz
Oberflächenfeinbearbeitung keramischer Werkstoffe mit XeCl-Excimerlaserstrahlung
LFT, 187 Seiten, 98 Bilder, 29 Tab. 1994.
ISBN 3-446-17970-4.

Band 40: Konrad Grampp
Rechnerunterstützung bei Test und Schulung an Steuerungssoftware von SMD-Bestücklinien
FAPS, 178 Seiten, 88 Bilder. 1995.
ISBN 3-446-18173-3.

Band 41: Martin Koch
Wissensbasierte Unterstützung der Angebotsbearbeitung in der Investitionsgüterindustrie
FAPS, 169 Seiten, 68 Bilder. 1995.
ISBN 3-446-18174-1.

Band 42: Armin Gropp
Anlagen- und Prozeßdiagnostik beim Schneiden mit einem gepulsten Nd:YAG-Laser
LFT, 160 Seiten, 88 Bilder, 7 Tab. 1995.
ISBN 3-446-18241-1.

Band 43: Werner Heckel
Optische 3D-Konturerfassung und on-line Biegewinkelmessung mit dem Lichtschnittverfahren
LFT, 149 Seiten, 43 Bilder, 11 Tab. 1995.
ISBN 3-446-18243-8.

Band 44: Armin Rothhaupt
Modulares Planungssystem zur Optimierung der Elektronikfertigung
FAPS, 180 Seiten, 101 Bilder. 1995.
ISBN 3-446-18307-8.

Band 45: Bernd Zöllner
Adaptive Diagnose in der Elektronikproduktion
FAPS, 195 Seiten, 74 Bilder, 3 Tab. 1995.
ISBN 3-446-18308-6.

Band 46: Bodo Vormann
Beitrag zur automatisierten Handhabungsplanung komplexer Blechbiegeteile
LFT, 126 Seiten, 89 Bilder, 3 Tab. 1995.
ISBN 3-446-18345-0.

Band 47: Peter Schnepf
Zielkostenorientierte Montageplanung
FAPS, 144 Seiten, 75 Bilder. 1995.
ISBN 3-446-18397-3.

Band 48: Rainer Klotzbücher
Konzept zur rechnerintegrierten Materialversorgung in flexiblen Fertigungssystemen
FAPS, 156 Seiten, 62 Bilder. 1995.
ISBN 3-446-18412-0.

Band 49: Wolfgang Greska
Wissensbasierte Analyse und Klassifizierung von Blechteilen
LFT, 144 Seiten, 96 Bilder. 1995.
ISBN 3-446-18462-7.

Band 50: Jörg Franke
Integrierte Entwicklung neuer Produkt- und Produktionstechnologien für räumliche spritzgegossene Schaltungsträger (3-D MID)
FAPS, 196 Seiten, 86 Bilder, 4 Tab. 1995.
ISBN 3-446-18448-1.

Band 51: Franz-Josef Zeller
Sensorplanung und schnelle Sensorregelung für Industrieroboter
FAPS, 190 Seiten, 102 Bilder, 9 Tab. 1995.
ISBN 3-446-18601-8.

Band 52: Michael Solvie
Zeitbehandlung und Multimedia-Unterstützung in Feldkommunikationssystemen
FAPS, 200 Seiten, 87 Bilder, 35 Tab. 1996.
ISBN 3-446-18607-7.

Band 53: Robert Hopperdietzel
Reengineering in der Elektro- und Elektronikindustrie
FAPS, 180 Seiten, 109 Bilder, 1 Tab. 1996.
ISBN 3-87525-070-2.

Band 54: Thomas Rebhahn
Beitrag zur Mikromaterialbearbeitung mit Excimerlasern - Systemkomponenten und Verfahrensoptimierungen
LFT, 148 Seiten, 61 Bilder, 10 Tab. 1996.
ISBN 3-87525-075-3.

Band 55: Henning Hanebuth
Laserstrahlhartlöten mit Zweistrahltechnik
LFT, 157 Seiten, 58 Bilder, 11 Tab. 1996.
ISBN 3-87525-074-5.

Band 56: Uwe Schönherr
Steuerung und Sensordatenintegration für flexible Fertigungszellen mit kooperierenden Robotern
FAPS, 188 Seiten, 116 Bilder, 3 Tab. 1996.
ISBN 3-87525-076-1.

Band 57: Stefan Holzer
Berührungslose Formgebung mit Laserstrahlung
LFT, 162 Seiten, 69 Bilder, 11 Tab. 1996.
ISBN 3-87525-079-6.

Band 58: Markus Schultz
Fertigungsqualität beim 3D-Laserstrahlschweißen von Blechformteilen
LFT, 165 Seiten, 88 Bilder, 9 Tab. 1997.
ISBN 3-87525-080-X.

Band 59: Thomas Krebs
Integration elektromechanischer CA-Anwendungen über einem STEP-Produktmodell
FAPS, 198 Seiten, 58 Bilder, 8 Tab. 1997.
ISBN 3-87525-081-8.

Band 60: Jürgen Sturm
Prozeßintegrierte Qualitätssicherung in der Elektronikproduktion
FAPS, 167 Seiten, 112 Bilder, 5 Tab. 1997.
ISBN 3-87525-082-6.

Band 61: Andreas Brand
Prozesse und Systeme zur Bestückung räumlicher elektronischer Baugruppen (3D-MID)
FAPS, 182 Seiten, 100 Bilder. 1997.
ISBN 3-87525-087-7.

Band 62: Michael Kauf
Regelung der Laserstrahlleistung und der Fokusparameter einer CO_2-Hochleistungslaseranlage
LFT, 140 Seiten, 70 Bilder, 5 Tab. 1997.
ISBN 3-87525-083-4.

Band 63: Peter Steinwasser
Modulares Informationsmanagement in der integrierten Produkt- und Prozeßplanung
FAPS, 190 Seiten, 87 Bilder. 1997.
ISBN 3-87525-084-2.

Band 64: Georg Liedl
Integriertes Automatisierungskonzept für den flexiblen Materialfluß in der Elektronikproduktion
FAPS, 196 Seiten, 96 Bilder, 3 Tab. 1997.
ISBN 3-87525-086-9.

Band 65: Andreas Otto
Transiente Prozesse beim Laserstrahlschweißen
LFT, 132 Seiten, 62 Bilder, 1 Tab. 1997.
ISBN 3-87525-089-3.

Band 66: Wolfgang Blöchl
Erweiterte Informationsbereitstellung an offenen CNC-Steuerungen zur Prozeß- und Programmoptimierung
FAPS, 168 Seiten, 96 Bilder. 1997.
ISBN 3-87525-091-5.

Band 67: Klaus-Uwe Wolf
Verbesserte Prozeßführung und Prozeßplanung zur Leistungs- und Qualitätssteigerung beim Spulenwickeln
FAPS, 186 Seiten, 125 Bilder. 1997.
ISBN 3-87525-092-3.

Band 68: Frank Backes
Technologieorientierte Bahnplanung für die 3D-Laserstrahlbearbeitung
LFT, 138 Seiten, 71 Bilder, 2 Tab. 1997.
ISBN 3-87525-093-1.

Band 69: Jürgen Kraus
Laserstrahlumformen von Profilen
LFT, 137 Seiten, 72 Bilder, 8 Tab. 1997.
ISBN 3-87525-094-X.

Band 70: Norbert Neubauer
Adaptive Strahlführungen für CO_2-Laseranlagen
LFT, 120 Seiten, 50 Bilder, 3 Tab. 1997.
ISBN 3-87525-095-8.

Band 71: Michael Steber
Prozeßoptimierter Betrieb flexibler Schraubstationen in der automatisierten Montage
FAPS, 168 Seiten, 78 Bilder, 3 Tab. 1997.
ISBN 3-87525-096-6.

Band 72: Markus Pfestorf
Funktionale 3D-Oberflächenkenngrößen in der Umformtechnik
LFT, 162 Seiten, 84 Bilder, 15 Tab. 1997.
ISBN 3-87525-097-4.

Band 73: Volker Franke
Integrierte Planung und Konstruktion von Werkzeugen für die Biegebearbeitung
LFT, 143 Seiten, 81 Bilder. 1998.
ISBN 3-87525-098-2.

Band 74: Herbert Scheller
Automatisierte Demontagesysteme und recyclinggerechte Produktgestaltung elektronischer Baugruppen
FAPS, 184 Seiten, 104 Bilder, 17 Tab. 1998.
ISBN 3-87525-099-0.

Band 75: Arthur Meßner
Kaltmassivumformung metallischer Kleinstteile – Werkstoffverhalten, Wirkflächenreibung, Prozeßauslegung
LFT, 164 Seiten, 92 Bilder, 14 Tab. 1998.
ISBN 3-87525-100-8.

Band 76: Mathias Glasmacher
Prozeß- und Systemtechnik zum Laserstrahl-Mikroschweißen
LFT, 184 Seiten, 104 Bilder, 12 Tab. 1998.
ISBN 3-87525-101-6.

Band 77: Michael Schwind
Zerstörungsfreie Ermittlung mechanischer Eigenschaften von Feinblechen mit dem Wirbelstromverfahren
LFT, 124 Seiten, 68 Bilder, 8 Tab. 1998.
ISBN 3-87525-102-4.

Band 78: Manfred Gerhard
Qualitätssteigerung in der Elektronikproduktion durch Optimierung der Prozeßführung beim Löten komplexer Baugruppen
FAPS, 179 Seiten, 113 Bilder, 7 Tab. 1998.
ISBN 3-87525-103-2.

Band 79: Elke Rauh
Methodische Einbindung der Simulation in die betrieblichen Planungs- und Entscheidungsabläufe
FAPS, 192 Seiten, 114 Bilder, 4 Tab. 1998.
ISBN 3-87525-104-0.

Band 80: Sorin Niederkorn
Meßeinrichtung zur Untersuchung der Wirkflächenreibung bei umformtechnischen Prozessen
LFT, 99 Seiten, 46 Bilder, 6 Tab. 1998.
ISBN 3-87525-105-9.

Band 81: Stefan Schuberth
Regelung der Fokuslage beim Schweißen mit CO_2-Hochleistungslasern unter Einsatz von adaptiven Optiken
LFT, 140 Seiten, 64 Bilder, 3 Tab. 1998.
ISBN 3-87525-106-7.

Band 82: Armando Walter Colombo
Development and Implementation of Hierarchical Control Structures of Flexible Production Systems Using High Level Petri Nets
FAPS, 216 Seiten, 86 Bilder. 1998.
ISBN 3-87525-109-1.

Band 83: Otto Meedt
Effizienzsteigerung bei Demontage und Recycling durch flexible Demontagetechnologien und optimierte Produktgestaltung
FAPS, 186 Seiten, 103 Bilder. 1998.
ISBN 3-87525-108-3.

Band 84: Knuth Götz
Modelle und effiziente Modellbildung zur Qualitätssicherung in der Elektronikproduktion
FAPS, 212 Seiten, 129 Bilder, 24 Tab. 1998.
ISBN 3-87525-112-1.

Band 85: Ralf Luchs
Einsatzmöglichkeiten leitender Klebstoffe zur zuverlässigen Kontaktierung elektronischer Bauelemente in der SMT
FAPS, 176 Seiten, 126 Bilder, 30 Tab. 1998.
ISBN 3-87525-113-7.

Band 86: Frank Pöhlau
Entscheidungsgrundlagen zur Einführung räumlicher spritzgegossener Schaltungsträger (3-D MID)
FAPS, 144 Seiten, 99 Bilder. 1999.
ISBN 3-87525-114-8.

Band 87: Roland T. A. Kals
Fundamentals on the miniaturization of sheet metal working processes
LFT, 128 Seiten, 58 Bilder, 11 Tab. 1999.
ISBN 3-87525-115-6.

Band 88: Gerhard Luhn
Implizites Wissen und technisches Handeln am Beispiel der Elektronikproduktion
FAPS, 252 Seiten, 61 Bilder, 1 Tab. 1999.
ISBN 3-87525-116-4.

Band 89: Axel Sprenger
Adaptives Streckbiegen von Aluminium-Strangpreßprofilen
LFT, 114 Seiten, 63 Bilder, 4 Tab. 1999.
ISBN 3-87525-117-2.

Band 90: Hans-Jörg Pucher
Untersuchungen zur Prozeßfolge Umformen, Bestücken und Laserstrahllöten von Mikrokontakten
LFT, 158 Seiten, 69 Bilder, 9 Tab. 1999.
ISBN 3-87525-119-9.

Band 91: Horst Arnet
Profilbiegen mit kinematischer Gestalterzeugung
LFT, 128 Seiten, 67 Bilder, 7 Tab. 1999.
ISBN 3-87525-120-2.

Band 92: Doris Schubart
Prozeßmodellierung und Technologieentwicklung beim Abtragen mit CO_2-Laserstrahlung
LFT, 133 Seiten, 57 Bilder, 13 Tab. 1999.
ISBN 3-87525-122-9.

Band 93: Adrianus L. P. Coremans
Laserstrahlsintern von Metallpulver - Prozeßmodellierung, Systemtechnik, Eigenschaften laserstrahlgesinterter Metallkörper
LFT, 184 Seiten, 108 Bilder, 12 Tab. 1999.
ISBN 3-87525-124-5.

Band 94: Hans-Martin Biehler
Optimierungskonzepte für Qualitätsdatenverarbeitung und Informationsbereitstellung in der Elektronikfertigung
FAPS, 194 Seiten, 105 Bilder. 1999.
ISBN 3-87525-126-1.

Band 95: Wolfgang Becker
Oberflächenausbildung und tribologische Eigenschaften excimerlaserstrahlbearbeiteter Hochleistungskeramiken
LFT, 175 Seiten, 71 Bilder, 3 Tab. 1999.
ISBN 3-87525-127-X.

Band 96: Philipp Hein
Innenhochdruck-Umformen von Blechpaaren: Modellierung, Prozeßauslegung und Prozeßführung
LFT, 129 Seiten, 57 Bilder, 7 Tab. 1999.
ISBN 3-87525-128-8.

Band 97: Gunter Beitinger
Herstellungs- und Prüfverfahren für thermoplastische Schaltungsträger
FAPS, 169 Seiten, 92 Bilder, 20 Tab. 1999.
ISBN 3-87525-129-6.

Band 98: Jürgen Knoblach
Beitrag zur rechnerunterstützten verursachungsgerechten Angebotskalkulation von Blechteilen mit Hilfe wissensbasierter Methoden
LFT, 155 Seiten, 53 Bilder, 26 Tab. 1999.
ISBN 3-87525-130-X.

Band 99: Frank Breitenbach
Bildverarbeitungssystem zur Erfassung der Anschlußgeometrie elektronischer SMT-Bauelemente
LFT, 147 Seiten, 92 Bilder, 12 Tab. 2000.
ISBN 3-87525-131-8.

Band 100: Bernd Falk
Simulationsbasierte Lebensdauervorhersage für Werkzeuge der Kaltmassivumformung
LFT, 134 Seiten, 44 Bilder, 15 Tab. 2000.
ISBN 3-87525-136-9.

Band 101: Wolfgang Schlögl
Integriertes Simulationsdaten-Management für Maschinenentwicklung und Anlagenplanung
FAPS, 169 Seiten, 101 Bilder, 20 Tab. 2000.
ISBN 3-87525-137-7.

Band 102: Christian Hinsel
Ermüdungsbruchversagen hartstoffbeschichteter Werkzeugstähle in der Kaltmassivumformung
LFT, 130 Seiten, 80 Bilder, 14 Tab. 2000.
ISBN 3-87525-138-5.

Band 103: Stefan Bobbert
Simulationsgestützte Prozessauslegung für das Innenhochdruck-Umformen von Blechpaaren
LFT, 123 Seiten, 77 Bilder. 2000.
ISBN 3-87525-145-8.

Band 104: Harald Rottbauer
Modulares Planungswerkzeug zum Produktionsmanagement in der Elektronikproduktion
FAPS, 166 Seiten, 106 Bilder. 2001.
ISBN 3-87525-139-3.

Band 105: Thomas Hennige
Flexible Formgebung von Blechen durch Laserstrahlumformen
LFT, 119 Seiten, 50 Bilder. 2001.
ISBN 3-87525-140-7.

Band 106: Thomas Menzel
Wissensbasierte Methoden für die rechnergestützte Charakterisierung und Bewertung innovativer Fertigungsprozesse
LFT, 152 Seiten, 71 Bilder. 2001.
ISBN 3-87525-142-3.

Band 107: Thomas Stöckel
Kommunikationstechnische Integration der Prozeßebene in Produktionssysteme durch Middleware-Frameworks
FAPS, 147 Seiten, 65 Bilder, 5 Tab. 2001.
ISBN 3-87525-143-1.

Band 108: Frank Pitter
Verfügbarkeitssteigerung von Werkzeugmaschinen durch Einsatz mechatronischer Sensorlösungen
FAPS, 158 Seiten, 131 Bilder, 8 Tab. 2001.
ISBN 3-87525-144-X.

Band 109: Markus Korneli
Integration lokaler CAP-Systeme in einen globalen Fertigungsdatenverbund
FAPS, 121 Seiten, 53 Bilder, 11 Tab. 2001.
ISBN 3-87525-146-6.

Band 110: Burkhard Müller
Laserstrahljustieren mit Excimer-Lasern - Prozeßparameter und Modelle zur Aktorkonstruktion
LFT, 128 Seiten, 36 Bilder, 9 Tab. 2001.
ISBN 3-87525-159-8.

Band 111: Jürgen Göhringer
Integrierte Telediagnose via Internet zum effizienten Service von Produktionssystemen
FAPS, 178 Seiten, 98 Bilder, 5 Tab. 2001.
ISBN 3-87525-147-4.

Band 112: Robert Feuerstein
Qualitäts- und kosteneffiziente Integration neuer Bauelementetechnologien in die Flachbaugruppenfertigung
FAPS, 161 Seiten, 99 Bilder, 10 Tab. 2001.
ISBN 3-87525-151-2.

Band 113: Marcus Reichenberger
Eigenschaften und Einsatzmöglichkeiten alternativer Elektroniklote in der Oberflächenmontage (SMT)
FAPS, 165 Seiten, 97 Bilder, 18 Tab. 2001.
ISBN 3-87525-152-0.

Band 114: Alexander Huber
Justieren vormontierter Systeme mit dem Nd:YAG-Laser unter Einsatz von Aktoren
LFT, 122 Seiten, 58 Bilder, 5 Tab. 2001.
ISBN 3-87525-153-9.

Band 115: Sami Krimi
Analyse und Optimierung von Montagesystemen in der Elektronikproduktion
FAPS, 155 Seiten, 88 Bilder, 3 Tab. 2001.
ISBN 3-87525-157-1.

Band 116: Marion Merklein
Laserstrahlumformen von Aluminiumwerkstoffen - Beeinflussung der Mikrostruktur und der mechanischen Eigenschaften
LFT, 122 Seiten, 65 Bilder, 15 Tab. 2001.
ISBN 3-87525-156-3.

Band 117: Thomas Collisi
Ein informationslogistisches Architekturkonzept zur Akquisition simulationsrelevanter Daten
FAPS, 181 Seiten, 105 Bilder, 7 Tab. 2002.
ISBN 3-87525-164-4.

Band 118: Markus Koch
Rationalisierung und ergonomische Optimierung im Innenausbau durch den Einsatz moderner Automatisierungstechnik
FAPS, 176 Seiten, 98 Bilder, 9 Tab. 2002.
ISBN 3-87525-165-2.

Band 119: Michael Schmidt
Prozeßregelung für das Laserstrahl-Punktschweißen in der Elektronikproduktion
LFT, 152 Seiten, 71 Bilder, 3 Tab. 2002.
ISBN 3-87525-166-0.

Band 120: Nicolas Tiesler
Grundlegende Untersuchungen zum Fließpressen metallischer Kleinstteile
LFT, 126 Seiten, 78 Bilder, 12 Tab. 2002.
ISBN 3-87525-175-X.

Band 121: Lars Pursche
Methoden zur technologieorientierten Programmierung für die 3D-Lasermikrobearbeitung
LFT, 111 Seiten, 39 Bilder, 0 Tab. 2002.
ISBN 3-87525-183-0.

Band 122: Jan-Oliver Brassel
Prozeßkontrolle beim Laserstrahl-Mikroschweißen
LFT, 148 Seiten, 72 Bilder, 12 Tab. 2002.
ISBN 3-87525-181-4.

Band 123: Mark Geisel
Prozeßkontrolle und -steuerung beim Laserstrahlschweißen mit den Methoden der nichtlinearen Dynamik
LFT, 135 Seiten, 46 Bilder, 2 Tab. 2002.
ISBN 3-87525-180-6.

Band 124: Gerd Eßer
Laserstrahlunterstützte Erzeugung metallischer Leiterstrukturen auf Thermoplastsubstraten für die MID-Technik
LFT, 148 Seiten, 60 Bilder, 6 Tab. 2002.
ISBN 3-87525-171-7.

Band 125: Marc Fleckenstein
Qualität laserstrahl-gefügter Mikroverbindungen elektronischer Kontakte
LFT, 159 Seiten, 77 Bilder, 7 Tab. 2002.
ISBN 3-87525-170-9.

Band 126: Stefan Kaufmann
Grundlegende Untersuchungen zum Nd:YAG- Laserstrahlfügen von Silizium für Komponenten der Optoelektronik
LFT, 159 Seiten, 100 Bilder, 6 Tab. 2002.
ISBN 3-87525-172-5.

Band 127: Thomas Fröhlich
Simultanes Löten von Anschlußkontakten elektronischer Bauelemente mit Diodenlaserstrahlung
LFT, 143 Seiten, 75 Bilder, 6 Tab. 2002.
ISBN 3-87525-186-5.

Band 128: Achim Hofmann
Erweiterung der Formgebungsgrenzen beim Umformen von Aluminiumwerkstoffen durch den Einsatz prozessangepasster Platinen
LFT, 113 Seiten, 58 Bilder, 4 Tab. 2002.
ISBN 3-87525-182-2.

Band 129: Ingo Kriebitzsch
3 - D MID Technologie in der Automobilelektronik
FAPS, 129 Seiten, 102 Bilder, 10 Tab. 2002.
ISBN 3-87525-169-5.

Band 130: Thomas Pohl
Fertigungsqualität und Umformbarkeit laserstrahlgeschweißter Formplatinen aus Aluminiumlegierungen
LFT, 133 Seiten, 93 Bilder, 12 Tab. 2002.
ISBN 3-87525-173-3.

Band 131: Matthias Wenk
Entwicklung eines konfigurierbaren Steuerungssystems für die flexible Sensorführung von Industrierobotern
FAPS, 167 Seiten, 85 Bilder, 1 Tab. 2002.
ISBN 3-87525-174-1.

Band 132: Matthias Negendanck

Neue Sensorik und Aktorik für Bearbeitungsköpfe zum Laserstrahlschweißen

LFT, 116 Seiten, 60 Bilder, 14 Tab. 2002.

ISBN 3-87525-184-9.

Band 133: Oliver Kreis

Integrierte Fertigung - Verfahrensintegration durch Innenhochdruck-Umformen, Trennen und Laserstrahlschweißen in einem Werkzeug sowie ihre tele- und multimediale Präsentation

LFT, 167 Seiten, 90 Bilder, 43 Tab. 2002.

ISBN 3-87525-176-8.

Band 134: Stefan Trautner

Technische Umsetzung produktbezogener Instrumente der Umweltpolitik bei Elektro- und Elektronikgeräten

FAPS, 179 Seiten, 92 Bilder, 11 Tab. 2002.

ISBN 3-87525-177-6.

Band 135: Roland Meier

Strategien für einen produktorientierten Einsatz räumlicher spritzgegossener Schaltungsträger (3-D MID)

FAPS, 155 Seiten, 88 Bilder, 14 Tab. 2002.

ISBN 3-87525-178-4.

Band 136: Jürgen Wunderlich

Kostensimulation - Simulationsbasierte Wirtschaftlichkeitsregelung komplexer Produktionssysteme

FAPS, 202 Seiten, 119 Bilder, 17 Tab. 2002.

ISBN 3-87525-179-2.

Band 137: Stefan Novotny

Innenhochdruck-Umformen von Blechen aus Aluminium- und Magnesiumlegierungen bei erhöhter Temperatur

LFT, 132 Seiten, 82 Bilder, 6 Tab. 2002.

ISBN 3-87525-185-7.

Band 138: Andreas Licha

Flexible Montageautomatisierung zur Komplettmontage flächenhafter Produktstrukturen durch kooperierende Industrieroboter

FAPS, 158 Seiten, 87 Bilder, 8 Tab. 2003.

ISBN 3-87525-189-X.

Band 139: Michael Eisenbarth

Beitrag zur Optimierung der Aufbau- und Verbindungstechnik für mechatronische Baugruppen

FAPS, 207 Seiten, 141 Bilder, 9 Tab. 2003.

ISBN 3-87525-190-3.

Band 140: Frank Christoph

Durchgängige simulationsgestützte Planung von Fertigungseinrichtungen der Elektronikproduktion

FAPS, 187 Seiten, 107 Bilder, 9 Tab. 2003.

ISBN 3-87525-191-1.

Band 141: Hinnerk Hagenah

Simulationsbasierte Bestimmung der zu erwartenden Maßhaltigkeit für das Blechbiegen

LFT, 131 Seiten, 36 Bilder, 26 Tab. 2003.

ISBN 3-87525-192-X.

Band 142: Ralf Eckstein

Scherschneiden und Biegen metallischer Kleinstteile - Materialeinfluss und Materialverhalten

LFT, 148 Seiten, 71 Bilder, 19 Tab. 2003.

ISBN 3-87525-193-8.

Band 143: Frank H. Meyer-Pittroff

Excimerlaserstrahlbiegen dünner metallischer Folien mit homogener Lichtlinie

LFT, 138 Seiten, 60 Bilder, 16 Tab. 2003.

ISBN 3-87525-196-2.

Band 144: Andreas Kach
Rechnergestützte Anpassung von Laserstrahlschneidbahnen an Bauteilabweichungen
LFT, 139 Seiten, 69 Bilder, 11 Tab. 2004.
ISBN 3-87525-197-0.

Band 145: Stefan Hierl
System- und Prozeßtechnik für das simultane Löten mit Diodenlaserstrahlung von elektronischen Bauelementen
LFT, 124 Seiten, 66 Bilder, 4 Tab. 2004.
ISBN 3-87525-198-9.

Band 146: Thomas Neudecker
Tribologische Eigenschaften keramischer Blechumformwerkzeuge- Einfluss einer Oberflächenendbearbeitung mittels Excimerlaserstrahlung
LFT, 166 Seiten, 75 Bilder, 26 Tab. 2004.
ISBN 3-87525-200-4.

Band 147: Ulrich Wenger
Prozessoptimierung in der Wickeltechnik durch innovative maschinenbauliche und regelungstechnische Ansätze
FAPS, 132 Seiten, 88 Bilder, 0 Tab. 2004.
ISBN 3-87525-203-9.

Band 148: Stefan Slama
Effizienzsteigerung in der Montage durch marktorientierte Montagestrukturen und erweiterte Mitarbeiterkompetenz
FAPS, 188 Seiten, 125 Bilder, 0 Tab. 2004.
ISBN 3-87525-204-7.

Band 149: Thomas Wurm
Laserstrahljustieren mittels Aktoren-Entwicklung von Konzepten und Methoden für die rechnerunterstützte Modellierung und Optimierung von komplexen Aktorsystemen in der Mikrotechnik
LFT, 122 Seiten, 51 Bilder, 9 Tab. 2004.
ISBN 3-87525-206-3.

Band 150: Martino Celeghini
Wirkmedienbasierte Blechumformung: Grundlagenuntersuchungen zum Einfluss von Werkstoff und Bauteilgeometrie
LFT, 146 Seiten, 77 Bilder, 6 Tab. 2004.
ISBN 3-87525-207-1.

Band 151: Ralph Hohenstein
Entwurf hochdynamischer Sensor- und Regelsysteme für die adaptive Laserbearbeitung
LFT, 282 Seiten, 63 Bilder, 16 Tab. 2004.
ISBN 3-87525-210-1.

Band 152: Angelika Hutterer
Entwicklung prozessüberwachender Regelkreise für flexible Formgebungsprozesse
LFT, 149 Seiten, 57 Bilder, 2 Tab. 2005.
ISBN 3-87525-212-8.

Band 153: Emil Egerer
Massivumformen metallischer Kleinstteile bei erhöhter Prozesstemperatur
LFT, 158 Seiten, 87 Bilder, 10 Tab. 2005.
ISBN 3-87525-213-6.

Band 154: Rüdiger Holzmann
Strategien zur nachhaltigen Optimierung von Qualität und Zuverlässigkeit in der Fertigung hochintegrierter Flachbaugruppen
FAPS, 186 Seiten, 99 Bilder, 19 Tab. 2005.
ISBN 3-87525-217-9.

Band 155: Marco Nock
Biegeumformen mit Elastomerwerkzeugen Modellierung, Prozessauslegung und Abgrenzung des Verfahrens am Beispiel des Rohrbiegens
LFT, 164 Seiten, 85 Bilder, 13 Tab. 2005.
ISBN 3-87525-218-7.

Band 156: Frank Niebling
Qualifizierung einer Prozesskette zum Laserstrahlsintern metallischer Bauteile
LFT, 148 Seiten, 89 Bilder, 3 Tab. 2005.
ISBN 3-87525-219-5.

Band 157: Markus Meiler
Großserientauglichkeit trockenschmierstoffbeschichteter Aluminiumbleche im Presswerk Grundlegende Untersuchungen zur Tribologie, zum Umformverhalten und Bauteilversuche
LFT, 104 Seiten, 57 Bilder, 21 Tab. 2005.
ISBN 3-87525-221-7.

Band 158: Agus Sutanto
Solution Approaches for Planning of Assembly Systems in Three-Dimensional Virtual Environments
FAPS, 169 Seiten, 98 Bilder, 3 Tab. 2005.
ISBN 3-87525-220-9.

Band 159: Matthias Boiger
Hochleistungssysteme für die Fertigung elektronischer Baugruppen auf der Basis flexibler Schaltungsträger
FAPS, 175 Seiten, 111 Bilder, 8 Tab. 2005.
ISBN 3-87525-222-5.

Band 160: Matthias Pitz
Laserunterstütztes Biegen höchstfester Mehrphasenstähle
LFT, 120 Seiten, 73 Bilder, 11 Tab. 2005.
ISBN 3-87525-223-3.

Band 161: Meik Vahl
Beitrag zur gezielten Beeinflussung des Werkstoffflusses beim Innenhochdruck-Umformen von Blechen
LFT, 165 Seiten, 94 Bilder, 15 Tab. 2005.
ISBN 3-87525-224-1.

Band 162: Peter K. Kraus
Plattformstrategien - Realisierung einer varianz- und kostenoptimierten Wertschöpfung
FAPS, 181 Seiten, 95 Bilder, 0 Tab. 2005.
ISBN 3-87525-226-8.

Band 163: Adrienn Cser
Laserstrahlschmelzabtrag - Prozessanalyse und -modellierung
LFT, 146 Seiten, 79 Bilder, 3 Tab. 2005.
ISBN 3-87525-227-6.

Band 164: Markus C. Hahn
Grundlegende Untersuchungen zur Herstellung von Leichtbauverbundstrukturen mit Aluminiumschaumkern
LFT, 143 Seiten, 60 Bilder, 16 Tab. 2005.
ISBN 3-87525-228-4.

Band 165: Gordana Michos
Mechatronische Ansätze zur Optimierung von Vorschubachsen
FAPS, 146 Seiten, 87 Bilder, 17 Tab. 2005.
ISBN 3-87525-230-6.

Band 166: Markus Stark
Auslegung und Fertigung hochpräziser Faser-Kollimator-Arrays
LFT, 158 Seiten, 115 Bilder, 11 Tab. 2005.
ISBN 3-87525-231-4.

Band 167: Yurong Zhou
Kollaboratives Engineering Management in der integrierten virtuellen Entwicklung der Anlagen für die Elektronikproduktion
FAPS, 156 Seiten, 84 Bilder, 6 Tab. 2005.
ISBN 3-87525-232-2.

Band 168: Werner Enser
Neue Formen permanenter und lösbarer elektrischer Kontaktierungen für mechatronische Baugruppen
FAPS, 190 Seiten, 112 Bilder, 5 Tab. 2005.
ISBN 3-87525-233-0.

Band 169: Katrin Melzer
Integrierte Produktpolitik bei elektrischen und elektronischen Geräten zur Optimierung des Product-Life-Cycle
FAPS, 155 Seiten, 91 Bilder, 17 Tab. 2005.
ISBN 3-87525-234-9.

Band 170: Alexander Putz
Grundlegende Untersuchungen zur Erfassung der realen Vorspannung von armierten Kaltfließpresswerkzeugen mittels Ultraschall
LFT, 137 Seiten, 71 Bilder, 15 Tab. 2006.
ISBN 3-87525-237-3.

Band 171: Martin Prechtl
Automatisiertes Schichtverfahren für metallische Folien - System- und Prozesstechnik
LFT, 154 Seiten, 45 Bilder, 7 Tab. 2006.
ISBN 3-87525-238-1.

Band 172: Markus Meidert
Beitrag zur deterministischen Lebensdauerabschätzung von Werkzeugen der Kaltmassivumformung
LFT, 131 Seiten, 78 Bilder, 9 Tab. 2006.
ISBN 3-87525-239-X.

Band 173: Bernd Müller
Robuste, automatisierte Montagesysteme durch adaptive Prozessführung und montageübergreifende Fehlerprävention am Beispiel flächiger Leichtbauteile
FAPS, 147 Seiten, 77 Bilder, 0 Tab. 2006.
ISBN 3-87525-240-3.

Band 174: Alexander Hofmann
Hybrides Laserdurchstrahlschweißen von Kunststoffen
LFT, 136 Seiten, 72 Bilder, 4 Tab. 2006.
ISBN 978-3-87525-243-9.

Band 175: Peter Wölflick
Innovative Substrate und Prozesse mit feinsten Strukturen für bleifreie Mechatronik-Anwendungen
FAPS, 177 Seiten, 148 Bilder, 24 Tab. 2006.
ISBN 978-3-87525-246-0.

Band 176: Attila Komlodi
Detection and Prevention of Hot Cracks during Laser Welding of Aluminium Alloys Using Advanced Simulation Methods
LFT, 155 Seiten, 89 Bilder, 14 Tab. 2006.
ISBN 978-3-87525-248-4.

Band 177: Uwe Popp
Grundlegende Untersuchungen zum Laserstrahlstrukturieren von Kaltmassivumformwerkzeugen
LFT, 140 Seiten, 67 Bilder, 16 Tab. 2006.
ISBN 978-3-87525-249-1.

Band 178: Veit Rückel
Rechnergestützte Ablaufplanung und Bahngenerierung Für kooperierende Industrieroboter
FAPS, 148 Seiten, 75 Bilder, 7 Tab. 2006.
ISBN 978-3-87525-250-7.

Band 179: Manfred Dirscherl
Nicht-thermische Mikrojustiertechnik mittels ultrakurzer Laserpulse
LFT, 154 Seiten, 69 Bilder, 10 Tab. 2007.
ISBN 978-3-87525-251-4.

Band 180: Yong Zhuo
Entwurf eines rechnergestützten integrierten Systems für Konstruktion und Fertigungsplanung räumlicher spritzgegossener Schaltungsträger (3D-MID)
FAPS, 181 Seiten, 95 Bilder, 5 Tab. 2007.
ISBN 978-3-87525-253-8.

Band 181: Stefan Lang
Durchgängige Mitarbeiterinformation zur Steigerung von Effizienz und Prozesssicherheit in der Produktion
FAPS, 172 Seiten, 93 Bilder. 2007.
ISBN 978-3-87525-257-6.

Band 182: Hans-Joachim Krauß
Laserstrahlinduzierte Pyrolyse präkeramischer Polymere
LFT, 171 Seiten, 100 Bilder. 2007.
ISBN 978-3-87525-258-3.

Band 183: Stefan Junker
Technologien und Systemlösungen für die flexibel automatisierte Bestückung permanent erregter Läufer mit oberflächenmontierten Dauermagneten
FAPS, 173 Seiten, 75 Bilder. 2007.
ISBN 978-3-87525-259-0.

Band 184: Rainer Kohlbauer
Wissensbasierte Methoden für die simulationsgestützte Auslegung wirkmedienbasierter Blechumformprozesse
LFT, 135 Seiten, 50 Bilder. 2007.
ISBN 978-3-87525-260-6.

Band 185: Klaus Lamprecht
Wirkmedienbasierte Umformung tiefgezogener Vorformen unter besonderer Berücksichtigung maßgeschneiderter Halbzeuge
LFT, 137 Seiten, 81 Bilder. 2007.
ISBN 978-3-87525-265-1.

Band 186: Bernd Zolleiß
Optimierte Prozesse und Systeme für die Bestückung mechatronischer Baugruppen
FAPS, 180 Seiten, 117 Bilder. 2007.
ISBN 978-3-87525-266-8.

Band 187: Michael Kerausch
Simulationsgestützte Prozessauslegung für das Umformen lokal wärmebehandelter Aluminiumplatinen
LFT, 146 Seiten, 76 Bilder, 7 Tab. 2007.
ISBN 978-3-87525-267-5.

Band 188: Matthias Weber
Unterstützung der Wandlungsfähigkeit von Produktionsanlagen durch innovative Softwaresysteme
FAPS, 183 Seiten, 122 Bilder, 3 Tab. 2007.
ISBN 978-3-87525-269-9.

Band 189: Thomas Frick
Untersuchung der prozessbestimmenden Strahl-Stoff-Wechselwirkungen beim Laserstrahlschweißen von Kunststoffen
LFT, 104 Seiten, 62 Bilder, 8 Tab. 2007.
ISBN 978-3-87525-268-2.

Band 190: Joachim Hecht
Werkstoffcharakterisierung und Prozessauslegung für die wirkmedienbasierte Doppelblech-Umformung von Magnesiumlegierungen
LFT, 107 Seiten, 91 Bilder, 2 Tab. 2007.
ISBN 978-3-87525-270-5.

Band 191: Ralf Völkl
Stochastische Simulation zur Werkzeuglebensdaueroptimierung und Präzisionsfertigung in der Kaltmassivumformung
LFT, 178 Seiten, 75 Bilder, 12 Tab. 2008.
ISBN 978-3-87525-272-9.

Band 192: Massimo Tolazzi
Innenhochdruck-Umformen verstärkter Blech-Rahmenstrukturen
LFT, 164 Seiten, 85 Bilder, 7 Tab. 2008.
ISBN 978-3-87525-273-6.

Band 193: Cornelia Hoff
Untersuchung der Prozesseinflussgrößen beim Presshärten des höchstfesten Vergütungsstahls 22MnB5
LFT, 133 Seiten, 92 Bilder, 5 Tab. 2008.
ISBN 978-3-87525-275-0.

Band 194: Christian Alvarez
Simulationsgestützte Methoden zur effizienten Gestaltung von Lötprozessen in der Elektronikproduktion
FAPS, 149 Seiten, 86 Bilder, 8 Tab. 2008.
ISBN 978-3-87525-277-4.

Band 195: Andreas Kunze
Automatisierte Montage von makromechatronischen Modulen zur flexiblen Integration in hybride Pkw-Bordnetzsysteme
FAPS, 160 Seiten, 90 Bilder, 14 Tab. 2008.
ISBN 978-3-87525-278-1.

Band 196: Wolfgang Hußnätter
Grundlegende Untersuchungen zur experimentellen Ermittlung und zur Modellierung von Fließortkurven bei erhöhten Temperaturen
LFT, 152 Seiten, 73 Bilder, 21 Tab. 2008.
ISBN 978-3-87525-279-8.

Band 197: Thomas Bigl
Entwicklung, angepasste Herstellungsverfahren und erweiterte Qualitätssicherung von einsatzgerechten elektronischen Baugruppen
FAPS, 175 Seiten, 107 Bilder, 14 Tab. 2008.
ISBN 978-3-87525-280-4.

Band 198: Stephan Roth
Grundlegende Untersuchungen zum Excimerlaserstrahl-Abtragen unter Flüssigkeitsfilmen
LFT, 113 Seiten, 47 Bilder, 14 Tab. 2008.
ISBN 978-3-87525-281-1.

Band 199: Artur Giera
Prozesstechnische Untersuchungen zum Rührreibschweißen metallischer Werkstoffe
LFT, 179 Seiten, 104 Bilder, 36 Tab. 2008.
ISBN 978-3-87525-282-8.

Band 200: Jürgen Lechler
Beschreibung und Modellierung des Werkstoffverhaltens von presshärtbaren Bor-Manganstählen
LFT, 154 Seiten, 75 Bilder, 12 Tab. 2009.
ISBN 978-3-87525-286-6.

Band 201: Andreas Blankl
Untersuchungen zur Erhöhung der Prozessrobustheit bei der Innenhochdruck-Umformung von flächigen Halbzeugen mit vor- bzw. nachgeschalteten Laserstrahlfügeoperationen
LFT, 120 Seiten, 68 Bilder, 9 Tab. 2009.
ISBN 978-3-87525-287-3.

Band 202: Andreas Schaller

Modellierung eines nachfrageorientierten Produktionskonzeptes für mobile Telekommunikationsgeräte

FAPS, 120 Seiten, 79 Bilder, 0 Tab. 2009.

ISBN 978-3-87525-289-7.

Band 203: Claudius Schimpf

Optimierung von Zuverlässigkeitsuntersuchungen, Prüfabläufen und Nacharbeitsprozessen in der Elektronikproduktion

FAPS, 162 Seiten, 90 Bilder, 14 Tab. 2009.

ISBN 978-3-87525-290-3.

Band 204: Simon Dietrich

Sensoriken zur Schwerpunktslagebestimmung der optischen Prozessemissionen beim Laserstrahltiefschweißen

LFT, 138 Seiten, 70 Bilder, 5 Tab. 2009.

ISBN 978-3-87525-292-7.

Band 205: Wolfgang Wolf

Entwicklung eines agentenbasierten Steuerungssystems zur Materialflussorganisation im wandelbaren Produktionsumfeld

FAPS, 167 Seiten, 98 Bilder. 2009.

ISBN 978-3-87525-293-4.

Band 206: Steffen Polster

Laserdurchstrahlschweißen transparenter Polymerbauteile

LFT, 160 Seiten, 92 Bilder, 13 Tab. 2009.

ISBN 978-3-87525-294-1.

Band 207: Stephan Manuel Dörfler

Rührreibschweißen von walzplattiertem Halbzeug und Aluminiumblech zur Herstellung flächiger Aluminiumschaum-Sandwich-Verbundstrukturen

LFT, 190 Seiten, 98 Bilder, 5 Tab. 2009.

ISBN 978-3-87525-295-8.

Band 208: Uwe Vogt

Seriennahe Auslegung von Aluminium Tailored Heat Treated Blanks

LFT, 151 Seiten, 68 Bilder, 26 Tab. 2009.

ISBN 978-3-87525-296-5.

Band 209: Till Laumann

Qualitative und quantitative Bewertung der Crashtauglichkeit von höchstfesten Stählen

LFT, 117 Seiten, 69 Bilder, 7 Tab. 2009.

ISBN 978-3-87525-299-6.

Band 210: Alexander Diehl

Größeneffekte bei Biegeprozessen- Entwicklung einer Methodik zur Identifikation und Quantifizierung

LFT, 180 Seiten, 92 Bilder, 12 Tab. 2010.

ISBN 978-3-87525-302-3.

Band 211: Detlev Staud

Effiziente Prozesskettenauslegung für das Umformen lokal wärmebehandelter und geschweißter Aluminiumbleche

LFT, 164 Seiten, 72 Bilder, 12 Tab. 2010.

ISBN 978-3-87525-303-0.

Band 212: Jens Ackermann

Prozesssicherung beim Laserdurchstrahlschweißen thermoplastischer Kunststoffe

LPT, 129 Seiten, 74 Bilder, 13 Tab. 2010.

ISBN 978-3-87525-305-4.

Band 213: Stephan Weidel

Grundlegende Untersuchungen zum Kontaktzustand zwischen Werkstück und Werkzeug bei umformtechnischen Prozessen unter tribologischen Gesichtspunkten

LFT, 144 Seiten, 67 Bilder, 11 Tab. 2010.

ISBN 978-3-87525-307-8.

Band 214: Stefan Geißdörfer
Entwicklung eines mesoskopischen Modells zur Abbildung von Größeneffekten in der Kaltmassivumformung mit Methoden der FE-Simulation
LFT, 133 Seiten, 83 Bilder, 11 Tab. 2010.
ISBN 978-3-87525-308-5.

Band 215: Christian Matzner
Konzeption produktspezifischer Lösungen zur Robustheitssteigerung elektronischer Systeme gegen die Einwirkung von Betauung im Automobil
FAPS, 165 Seiten, 93 Bilder, 14 Tab. 2010.
ISBN 978-3-87525-309-2.

Band 216: Florian Schüßler
Verbindungs- und Systemtechnik für thermisch hochbeanspruchte und miniaturisierte elektronische Baugruppen
FAPS, 184 Seiten, 93 Bilder, 18 Tab. 2010.
ISBN 978-3-87525-310-8.

Band 217: Massimo Cojutti
Strategien zur Erweiterung der Prozessgrenzen bei der Innhochdruck-Umformung von Rohren und Blechpaaren
LFT, 125 Seiten, 56 Bilder, 9 Tab. 2010.
ISBN 978-3-87525-312-2.

Band 218: Raoul Plettke
Mehrkriterielle Optimierung komplexer Aktorsysteme für das Laserstrahljustieren
LFT, 152 Seiten, 25 Bilder, 3 Tab. 2010.
ISBN 978-3-87525-315-3.

Band 219: Andreas Dobroschke
Flexible Automatisierungslösungen für die Fertigung wickeltechnischer Produkte
FAPS, 184 Seiten, 109 Bilder, 18 Tab. 2011.
ISBN 978-3-87525-317-7.

Band 220: Azhar Zam
Optical Tissue Differentiation for Sensor-Controlled Tissue-Specific Laser Surgery
LPT, 99 Seiten, 45 Bilder, 8 Tab. 2011.
ISBN 978-3-87525-318-4.

Band 221: Michael Rösch
Potenziale und Strategien zur Optimierung des Schablonendruckprozesses in der Elektronikproduktion
FAPS, 192 Seiten, 127 Bilder, 19 Tab. 2011.
ISBN 978-3-87525-319-1.

Band 222: Thomas Rechtenwald
Quasi-isothermes Laserstrahlsintern von Hochtemperatur-Thermoplasten - Eine Betrachtung werkstoff-prozessspezifischer Aspekte am Beispiel PEEK
LPT, 150 Seiten, 62 Bilder, 8 Tab. 2011.
ISBN 978-3-87525-320-7.

Band 223: Daniel Craiovan
Prozesse und Systemlösungen für die SMT-Montage optischer Bauelemente auf Substrate mit integrierten Lichtwellenleitern
FAPS, 165 Seiten, 85 Bilder, 8 Tab. 2011.
ISBN 978-3-87525-324-5.

Band 224: Kay Wagner
Beanspruchungsangepasste Kaltmassivumformwerkzeuge durch lokal optimierte Werkzeugoberflächen
LFT, 147 Seiten, 103 Bilder, 17 Tab. 2011.
ISBN 978-3-87525-325-2.

Band 225: Martin Brandhuber
Verbesserung der Prognosegüte des Versagens von Punktschweißverbindungen bei höchstfesten Stahlgüten
LFT, 155 Seiten, 91 Bilder, 19 Tab. 2011.
ISBN 978-3-87525-327-6.

Band 226: Peter Sebastian Feuser
Ein Ansatz zur Herstellung von pressgehärteten Karosseriekomponenten mit maßgeschneiderten mechanischen Eigenschaften: Temperierte Umformwerkzeuge. Prozessfenster, Prozesssimuation und funktionale Untersuchung
LFT, 195 Seiten, 97 Bilder, 60 Tab. 2012.
ISBN 978-3-87525-328-3.

Band 227: Murat Arbak
Material Adapted Design of Cold Forging Tools Exemplified by Powder Metallurgical Tool Steels and Ceramics
LFT, 109 Seiten, 56 Bilder, 8 Tab. 2012.
ISBN 978-3-87525-330-6.

Band 228: Indra Pitz
Beschleunigte Simulation des Laserstrahlumformens von Aluminiumblechen
LPT, 137 Seiten, 45 Bilder, 27 Tab. 2012.
ISBN 978-3-87525-333-7.

Band 229: Alexander Grimm
Prozessanalyse und -überwachung des Laserstrahlhartlötens mittels optischer Sensorik
LPT, 125 Seiten, 61 Bilder, 5 Tab. 2012.
ISBN 978-3-87525-334-4.

Band 230: Markus Kaupper
Biegen von höhenfesten Stahlblechwerkstoffen - Umformverhalten und Grenzen der Biegbarkeit
LFT, 160 Seiten, 57 Bilder, 10 Tab. 2012.
ISBN 978-3-87525-339-9.

Band 231: Thomas Kroiß
Modellbasierte Prozessauslegung für die Kaltmassivumformung unter Brücksichtigung der Werkzeug- und Pressenauffederung
LFT, 169 Seiten, 50 Bilder, 19 Tab. 2012.
ISBN 978-3-87525-341-2.

Band 232: Christian Goth
Analyse und Optimierung der Entwicklung und Zuverlässigkeit räumlicher Schaltungsträger (3D-MID)
FAPS, 176 Seiten, 102 Bilder, 22 Tab. 2012.
ISBN 978-3-87525-340-5.

Band 233: Christian Ziegler
Ganzheitliche Automatisierung mechatronischer Systeme in der Medizin am Beispiel Strahlentherapie
FAPS, 170 Seiten, 71 Bilder, 19 Tab. 2012.
ISBN 978-3-87525-342-9.

Band 234: Florian Albert
Automatisiertes Laserstrahllöten und -reparaturlöten elektronischer Baugruppen
LPT, 127 Seiten, 78 Bilder, 11 Tab. 2012.
ISBN 978-3-87525-344-3.

Band 235: Thomas Stöhr
Analyse und Beschreibung des mechanischen Werkstoffverhaltens von presshärtbaren Bor-Manganstählen
LFT, 118 Seiten, 74 Bilder, 18 Tab. 2013.
ISBN 978-3-87525-346-7.

Band 236: Christian Kägeler
Prozessdynamik beim Laserstrahlschweißen verzinkter Stahlbleche im Überlappstoß
LPT, 145 Seiten, 80 Bilder, 3 Tab. 2013.
ISBN 978-3-87525-347-4.

Band 237: Andreas Sulzberger
Seriennahe Auslegung der Prozesskette zur wärmeunterstützten Umformung von Aluminiumblechwerkstoffen
LFT, 153 Seiten, 87 Bilder, 17 Tab. 2013.
ISBN 978-3-87525-349-8.

Band 238: Simon Opel
Herstellung prozessangepasster Halbzeuge mit variabler Blechdicke durch die Anwendung von Verfahren der Blechmassivumformung
LFT, 165 Seiten, 108 Bilder, 27 Tab. 2013.
ISBN 978-3-87525-350-4.

Band 239: Rajesh Kanawade
In-vivo Monitoring of Epithelium Vessel and Capillary Density for the Application of Detection of Clinical Shock and Early Signs of Cancer Development
LPT, 124 Seiten, 58 Bilder, 15 Tab. 2013.
ISBN 978-3-87525-351-1.

Band 240: Stephan Busse
Entwicklung und Qualifizierung eines Schneidclinchverfahrens
LFT, 119 Seiten, 86 Bilder, 20 Tab. 2013.
ISBN 978-3-87525-352-8.

Band 241: Karl-Heinz Leitz
Mikro- und Nanostrukturierung mit kurz und ultrakurz gepulster Laserstrahlung
LPT, 154 Seiten, 71 Bilder, 9 Tab. 2013.
ISBN 978-3-87525-355-9.

Band 242: Markus Michl
Webbasierte Ansätze zur ganzheitlichen technischen Diagnose
FAPS, 182 Seiten, 62 Bilder, 20 Tab. 2013.
ISBN 978-3-87525-356-6.

Band 243: Vera Sturm
Einfluss von Chargenschwankungen auf die Verarbeitungsgrenzen von Stahlwerkstoffen
LFT, 113 Seiten, 58 Bilder, 9 Tab. 2013.
ISBN 978-3-87525-357-3.

Band 244: Christian Neudel
Mikrostrukturelle und mechanisch-technologische Eigenschaften widerstandspunktgeschweißter Aluminium-Stahl-Verbindungen für den Fahrzeugbau
LFT, 178 Seiten, 171 Bilder, 31 Tab. 2014.
ISBN 978-3-87525-358-0.

Band 245: Anja Neumann
Konzept zur Beherrschung der Prozessschwankungen im Presswerk
LFT, 162 Seiten, 68 Bilder, 15 Tab. 2014.
ISBN 978-3-87525-360-3.

Band 246: Ulf-Hermann Quentin
Laserbasierte Nanostrukturierung mit optisch positionierten Mikrolinsen
LPT, 137 Seiten, 89 Bilder, 6 Tab. 2014.
ISBN 978-3-87525-361-0.

Band 247: Erik Lamprecht
Der Einfluss der Fertigungsverfahren auf die Wirbelstromverluste von Stator-Einzelzahnblechpaketen für den Einsatz in Hybrid- und Elektrofahrzeugen
FAPS, 148 Seiten, 138 Bilder, 4 Tab. 2014.
ISBN 978-3-87525-362-7.

Band 248: Sebastian Rösel
Wirkmedienbasierte Umformung von Blechhalbzeugen unter Anwendung magnetorheologischer Flüssigkeiten als kombiniertes Wirk- und Dichtmedium
LFT, 148 Seiten, 61 Bilder, 12 Tab. 2014.
ISBN 978-3-87525-363-4.

Band 249: Paul Hippchen
Simulative Prognose der Geometrie indirekt pressgehärteter Karosseriebauteile für die industrielle Anwendung
LFT, 163 Seiten, 89 Bilder, 12 Tab. 2014.
ISBN 978-3-87525-364-1.

Band 250: Martin Zubeil
Versagensprognose bei der Prozess simulation von Biegeumform- und Falzverfahren
LFT, 171 Seiten, 90 Bilder, 5 Tab. 2014.
ISBN 978-3-87525-365-8.

Band 251: Alexander Kühl
Flexible Automatisierung der Statorenmontage mit Hilfe einer universellen ambidexteren Kinematik
FAPS, 142 Seiten, 60 Bilder, 26 Tab. 2014.
ISBN 978-3-87525-367-2.

Band 252: Thomas Albrecht
Optimierte Fertigungstechnologien für Rotoren getriebeintegrierter PM-Synchronmotoren von Hybridfahrzeugen
FAPS, 198 Seiten, 130 Bilder, 38 Tab. 2014.
ISBN 978-3-87525-368-9.

Band 253: Florian Risch
Planning and Production Concepts for Contactless Power Transfer Systems for Electric Vehicles
FAPS, 185 Seiten, 125 Bilder, 13 Tab. 2014.
ISBN 978-3-87525-369-6.

Band 254: Markus Weigl
Laserstrahlschweißen von Mischverbindungen aus austenitischen und ferritischen korrosionsbeständigen Stahlwerkstoffen
LPT, 184 Seiten, 110 Bilder, 6 Tab. 2014.
ISBN 978-3-87525-370-2.

Band 255: Johannes Noneder
Beanspruchungserfassung für die Validierung von FE-Modellen zur Auslegung von Massivumformwerkzeugen
LFT, 161 Seiten, 65 Bilder, 14 Tab. 2014.
ISBN 978-3-87525-371-9.

Band 256: Andreas Reinhardt
Ressourceneffiziente Prozess- und Produktionstechnologie für flexible Schaltungsträger
FAPS, 123 Seiten, 69 Bilder, 19 Tab. 2014.
ISBN 978-3-87525-373-3.

Band 257: Tobias Schmuck
Ein Beitrag zur effizienten Gestaltung globaler Produktions- und Logistiknetzwerke mittels Simulation
FAPS, 151 Seiten, 74 Bilder. 2014.
ISBN 978-3-87525-374-0.

Band 258: Bernd Eichenhüller
Untersuchungen der Effekte und Wechselwirkungen charakteristischer Einflussgrößen auf das Umformverhalten bei Mikroumformprozessen
LFT, 127 Seiten, 29 Bilder, 9 Tab. 2014.
ISBN 978-3-87525-375-7.

Band 259: Felix Lütteke
Vielseitiges autonomes Transportsystem basierend auf Weltmodellerstellung mittels Datenfusion von Deckenkameras und Fahrzeugsensoren
FAPS, 152 Seiten, 54 Bilder, 20 Tab. 2014.
ISBN 978-3-87525-376-4.

Band 260: Martin Grüner
Hochdruck-Blechumformung mit formlos festen Stoffen als Wirkmedium
LFT, 144 Seiten, 66 Bilder, 29 Tab. 2014.
ISBN 978-3-87525-379-5.

Band 261: Christian Brock
Analyse und Regelung des Laserstrahltiefschweißprozesses durch Detektion der Metalldampffackelposition
LPT, 126 Seiten, 65 Bilder, 3 Tab. 2015.
ISBN 978-3-87525-380-1.

Band 262: Peter Vatter
Sensitivitätsanalyse des 3-Rollen-Schubbiegens auf Basis der Finite Elemente Methode
LFT, 145 Seiten, 57 Bilder, 26 Tab. 2015.
ISBN 978-3-87525-381-8.

Band 263: Florian Klämpfl
Planung von Laserbestrahlungen durch simulationsbasierte Optimierung
LPT, 169 Seiten, 78 Bilder, 32 Tab. 2015.
ISBN 978-3-87525-384-9.

Band 264: Matthias Domke
Transiente physikalische Mechanismen bei der Laserablation von dünnen Metallschichten
LPT, 133 Seiten, 43 Bilder, 3 Tab. 2015.
ISBN 978-3-87525-385-6.

Band 265: Johannes Götz
Community-basierte Optimierung des Anlagenengineerings
FAPS, 177 Seiten, 80 Bilder, 30 Tab. 2015.
ISBN 978-3-87525-386-3.

Band 266: Hung Nguyen
Qualifizierung des Potentials von Verfestigungseffekten zur Erweiterung des Umformvermögens aushärtbarer Aluminiumlegierungen
LFT, 137 Seiten, 57 Bilder, 16 Tab. 2015.
ISBN 978-3-87525-387-0.

Band 267: Andreas Kuppert
Erweiterung und Verbesserung von Versuchs- und Auswertetechniken für die Bestimmung von Grenzformänderungskurven
LFT, 138 Seiten, 82 Bilder, 2 Tab. 2015.
ISBN 978-3-87525-388-7.

Band 268: Kathleen Klaus
Erstellung eines Werkstofforientierten Fertigungsprozessfensters zur Steigerung des Formgebungsvermögens von Aluminiumlegierungen unter Anwendung einer zwischengeschalteten Wärmebehandlung
LFT, 154 Seiten, 70 Bilder, 8 Tab. 2015.
ISBN 978-3-87525-391-7.

Band 269: Thomas Svec
Untersuchungen zur Herstellung von funktionsoptimierten Bauteilen im partiellen Presshärtprozess mittels lokal unterschiedlich temperierter Werkzeuge
LFT, 166 Seiten, 87 Bilder, 15 Tab. 2015.
ISBN 978-3-87525-392-4.

Band 270: Tobias Schrader
Grundlegende Untersuchungen zur Verschleißcharakterisierung beschichteter Kaltmassivumformwerkzeuge
LFT, 164 Seiten, 55 Bilder, 11 Tab. 2015.
ISBN 978-3-87525-393-1.

Band 271: Matthäus Brela
Untersuchung von Magnetfeld-Messmethoden zur ganzheitlichen Wertschöpfungsoptimierung und Fehlerdetektion an magnetischen Aktoren
FAPS, 170 Seiten, 97 Bilder, 4 Tab. 2015.
ISBN 978-3-87525-394-8.

Band 272: Michael Wieland
Entwicklung einer Methode zur Prognose adhäsiven Verschleißes an Werkzeugen für das direkte Presshärten
LFT, 156 Seiten, 84 Bilder, 9 Tab. 2015.
ISBN 978-3-87525-395-5.

Band 273: René Schramm
Strukturierte additive Metallisierung durch kaltaktives Atmosphärendruckplasma
FAPS, 136 Seiten, 62 Bilder, 15 Tab. 2015.
ISBN 978-3-87525-396-2.

Band 274: Michael Lechner
Herstellung beanspruchungsangepasster Aluminiumblechhalbzeuge durch eine maßgeschneiderte Variation der Abkühlgeschwindigkeit nach Lösungsglühen
LFT, 136 Seiten, 62 Bilder, 15 Tab. 2015.
ISBN 978-3-87525-397-9.

Band 275: Kolja Andreas
Einfluss der Oberflächenbeschaffenheit auf das Werkzeugeinsatzverhalten beim Kaltfließpressen
LFT, 169 Seiten, 76 Bilder, 4 Tab. 2015.
ISBN 978-3-87525-398-6.

Band 276: Marcus Baum
Laser Consolidation of ITO Nanoparticles for the Generation of Thin Conductive Layers on Transparent Substrates
LPT, 158 Seiten, 75 Bilder, 3 Tab. 2015.
ISBN 978-3-87525-399-3.

Band 277: Thomas Schneider
Umformtechnische Herstellung dünnwandiger Funktionsbauteile aus Feinblech durch Verfahren der Blechmassivumformung
LFT, 188 Seiten, 95 Bilder, 7 Tab. 2015.
ISBN 978-3-87525-401-3.

Band 278: Jochen Merhof
Sematische Modellierung automatisierter Produktionssysteme zur Verbesserung der IT-Integration zwischen Anlagen-Engineering und Steuerungsebene
FAPS, 157 Seiten, 88 Bilder, 8 Tab. 2015.
ISBN 978-3-87525-402-0.

Band 279: Fabian Zöller
Erarbeitung von Grundlagen zur Abbildung des tribologischen Systems in der Umformsimulation
LFT, 126 Seiten, 51 Bilder, 3 Tab. 2016.
ISBN 978-3-87525-403-7.

Band 280: Christian Hezler
Einsatz technologischer Versuche zur Erweiterung der Versagensvorhersage bei Karosseriebauteilen aus höchstfesten Stählen
LFT, 147 Seiten, 63 Bilder, 44 Tab. 2016.
ISBN 978-3-87525-404-4.

Band 281: Jochen Bönig
Integration des Systemverhaltens von Automobil-Hochvoltleitungen in die virtuelle Absicherung durch strukturmechanische Simulation
FAPS, 177 Seiten, 107 Bilder, 17 Tab. 2016.
ISBN 978-3-87525-405-1.

Band 282: Johannes Kohl
Automatisierte Datenerfassung für diskret ereignisorientierte Simulationen in der energieflexibelen Fabrik
FAPS, 160 Seiten, 80 Bilder, 27 Tab. 2016.
ISBN 978-3-87525-406-8.

Band 283: Peter Bechtold
Mikroschockwellenumformung mittels ultrakurzer Laserpulse
LPT, 155 Seiten, 59 Bilder, 10 Tab. 2016.
ISBN 978-3-87525-407-5.

Band 284: Stefan Berger
Laserstrahlschweißen thermoplastischer Kohlenstofffaserverbundwerkstoffe mit spezifischem Zusatzdraht
LPT, 118 Seiten, 68 Bilder, 9 Tab. 2016.
ISBN 978-3-87525-408-2.

Band 285: Martin Bornschlegl
Methods-Energy Measurement - Eine Methode zur Energieplanung für Fügeverfahren im Karosseriebau
FAPS, 136 Seiten, 72 Bilder, 46 Tab. 2016.
ISBN 978-3-87525-409-9.

Band 286: Tobias Rackow
Erweiterung des Unternehmenscontrollings um die Dimension Energie
FAPS, 164 Seiten, 82 Bilder, 29 Tab. 2016.
ISBN 978-3-87525-410-5.

Band 287: Johannes Koch
Grundlegende Untersuchungen zur Herstellung zyklisch-symmetrischer Bauteile mit Nebenformelementen durch Blechmassivumformung
LFT, 125 Seiten, 49 Bilder, 17 Tab. 2016.
ISBN 978-3-87525-411-2.

Band 288: Hans Ulrich Vierzigmann
Beitrag zur Untersuchung der tribologischen Bedingungen in der Blechmassivumformung - Bereitstellung von tribologischen Modellversuchen und Realisierung von Tailored Surfaces
LFT, 174 Seiten, 102 Bilder, 34 Tab. 2016.
ISBN 978-3-87525-412-9.

Band 289: Thomas Senner
Methodik zur virtuellen Absicherung der formgebenden Operation des Nasspressprozesses von Gelege-Mehrschichtverbunden
LFT, 156 Seiten, 96 Bilder, 21 Tab. 2016.
ISBN 978-3-87525-414-3.

Band 290: Sven Kreitlein
Der grundoperationsspezifische Mindestenergiebedarf als Referenzwert zur Bewertung der Energieeffizienz in der Produktion
FAPS, 185 Seiten, 64 Bilder, 30 Tab. 2016.
ISBN 978-3-87525-415-0.

Band 291: Christian Roos
Remote-Laserstrahlschweißen verzinkter Stahlbleche in Kehlnahtgeometrie
LPT, 123 Seiten, 52 Bilder, 0 Tab. 2016.
ISBN 978-3-87525-416-7.

Band 292: Alexander Kahrimanidis
Thermisch unterstützte Umformung von Aluminiumblechen
LFT, 165 Seiten, 103 Bilder, 18 Tab. 2016.
ISBN 978-3-87525-417-4.

Band 293: Jan Tremel
Flexible Systems for Permanent Magnet Assembly and Magnetic Rotor Measurement / Flexible Systeme zur Montage von Permanentmagneten und zur Messung magnetischer Rotoren
FAPS, 152 Seiten, 91 Bilder, 12 Tab. 2016.
ISBN 978-3-87525-419-8.

Band 294: Ioannis Tsoupis
Schädigungs- und Versagensverhalten hochfester Leichtbauwerkstoffe unter Biegebeanspruchung
LFT, 176 Seiten, 51 Bilder, 6 Tab. 2017.
ISBN 978-3-87525-420-4.

Band 295: Sven Hildering
Grundlegende Untersuchungen zum Prozessverhalten von Silizium als Werkzeugwerkstoff für das Mikroscherschneiden metallischer Folien
LFT, 177 Seiten, 74 Bilder, 17 Tab. 2017.
ISBN 978-3-87525-422-8.

Band 296: Sasia Mareike Hertweck
Zeitliche Pulsformung in der Lasermikromaterialbearbeitung – Grundlegende Untersuchungen und Anwendungen
LPT, 146 Seiten, 67 Bilder, 5 Tab. 2017.
ISBN 978-3-87525-423-5.

Band 297: Paryanto
Mechatronic Simulation Approach for the Process Planning of Energy-Efficient Handling Systems
FAPS, 162 Seiten, 86 Bilder, 13 Tab. 2017.
ISBN 978-3-87525-424-2.

Band 298: Peer Stenzel
Großserientaugliche Nadelwickeltechnik für verteilte Wicklungen im Anwendungsfall der E-Traktionsantriebe
FAPS, 239 Seiten, 147 Bilder, 20 Tab. 2017.
ISBN 978-3-87525-425-9.

Band 299: Mario Lušić
Ein Vorgehensmodell zur Erstellung montageführender Werkerinformationssysteme simultan zum Produktentstehungsprozess
FAPS, 174 Seiten, 79 Bilder, 22 Tab. 2017.
ISBN 978-3-87525-426-6.

Band 300: Arnd Buschhaus
Hochpräzise adaptive Steuerung und Regelung robotergeführter Prozesse
FAPS, 202 Seiten, 96 Bilder, 4 Tab. 2017.
ISBN 978-3-87525-427-3.

Band 301: Tobias Laumer
Erzeugung von thermoplastischen Werkstoffverbunden mittels simultanem, intensitätsselektivem Laserstrahlschmelzen
LPT, 140 Seiten, 82 Bilder, 0 Tab. 2017.
ISBN 978-3-87525-428-0.

Band 302: Nora Unger
Untersuchung einer thermisch unterstützten Fertigungskette zur Herstellung umgeformter Bauteile aus der höherfesten Aluminiumlegierung EN AW-7020
LFT, 142 Seiten, 53 Bilder, 8 Tab. 2017.
ISBN 978-3-87525-429-7.

Band 303: Tommaso Stellin
Design of Manufacturing Processes for the Cold Bulk Forming of Small Metal Components from Metal Strip
LFT, 146 Seiten, 67 Bilder, 7 Tab. 2017.
ISBN 978-3-87525-430-3.

Band 304: Bassim Bachy

Experimental Investigation, Modeling, Simulation and Optimization of Molded Interconnect Devices (MID) Based on Laser Direct Structuring (LDS) / Experimentelle Untersuchung, Modellierung, Simulation und Optimierung von Molded Interconnect Devices (MID) basierend auf Laser Direktstrukturierung (LDS)

FAPS, 168 Seiten, 120 Bilder, 26 Tab. 2017.

ISBN 978-3-87525-431-0.

Band 305: Michael Spahr

Automatisierte Kontaktierungsverfahren für flachleiterbasierte Pkw-Bordnetzsysteme

FAPS, 197 Seiten, 98 Bilder, 17 Tab. 2017.

ISBN 978-3-87525-432-7.

Band 306: Sebastian Suttner

Charakterisierung und Modellierung des spannungszustandsabhängigen Werkstoffverhaltens der Magnesiumlegierung AZ31B für die numerische Prozessauslegung

LFT, 150 Seiten, 84 Bilder, 19 Tab. 2017.

ISBN 978-3-87525-433-4.

Band 307: Bhargav Potdar

A reliable methodology to deduce thermo-mechanical flow behaviour of hot stamping steels

LFT, 203 Seiten, 98 Bilder, 27 Tab. 2017.

ISBN 978-3-87525-436-5.

Band 308: Maria Löffler

Steuerung von Blechmassivumformprozessen durch maßgeschneiderte tribologische Systeme

LFT, viii u. 166 Seiten, 90 Bilder, 5 Tab. 2018. ISBN 978-3-96147-133-1.

Band 309: Martin Müller

Untersuchung des kombinierten Trenn- und Umformprozesses beim Fügen artungleicher Werkstoffe mittels Schneidclinchverfahren

LFT, xi u. 149 Seiten, 89 Bilder, 6 Tab. 2018. ISBN: 978-3-96147-135-5.

Band 310: Christopher Kästle

Qualifizierung der Kupfer-Drahtbondtechnologie für integrierte Leistungsmodule in harschen Umgebungsbedingungen

FAPS, xii u. 167 Seiten, 70 Bilder, 18 Tab. 2018. ISBN 978-3-96147-145-4.

Band 311: Daniel Vipavc

Eine Simulationsmethode für das 3-Rollen-Schubbiegen

LFT, xiii u. 121 Seiten, 56 Bilder, 17 Tab. 2018. ISBN 978-3-96147-147-8.

Band 312: Christina Ramer

Arbeitsraumüberwachung und autonome Bahnplanung für ein sicheres und flexibles Roboter-Assistenzsystem in der Fertigung

FAPS, xiv u. 188 Seiten, 57 Bilder, 9 Tab. 2018. ISBN 978-3-96147-153-9.

Band 313: Miriam Rauer

Der Einfluss von Poren auf die Zuverlässigkeit der Lötverbindungen von Hochleistungs-Leuchtdioden

FAPS, xii u. 209 Seiten, 108 Bilder, 21 Tab. 2018. ISBN 978-3-96147-157-7.

Band 314: Felix Tenner

Kamerabasierte Untersuchungen der Schmelze und Gasströmungen beim Laserstrahlschweißen verzinkter Stahlbleche

LPT, xxiii u. 184 Seiten, 94 Bilder, 7 Tab.
2018. ISBN 978-3-96147-160-7.

Band 315: Aarief Syed-Khaja

Diffusion Soldering for High-temperature Packaging of Power Electronics

FAPS, x u. 202 Seiten, 144 Bilder, 32 Tab.
2018. ISBN 978-3-87525-162-1.

Band 316: Adam Schaub

Grundlagenwissenschaftliche Untersuchung der kombinierten Prozesskette aus Umformen und Additive Fertigung

LFT, xi u. 192 Seiten, 72 Bilder, 27 Tab.
2019. ISBN 978-3-96147-166-9.

Band 317: Daniel Gröbel

Herstellung von Nebenformelementen unterschiedlicher Geometrie an Blechen mittels Fließpressverfahren der Blechmassivumformung

LFT, x u. 165 Seiten, 96 Bilder, 13 Tab.
2019. ISBN 978-3-96147-168-3.

Band 318: Philipp Hildenbrand

Entwicklung einer Methodik zur Herstellung von Tailored Blanks mit definierten Halbzeugeigenschaften durch einen Taumelprozess

LFT, ix u. 153 Seiten, 77 Bilder, 4 Tab.
2019. ISBN 978-3-96147-174-4.

Band 319: Tobias Konrad

Simulative Auslegung der Spann- und Fixierkonzepte im Karosserierohbau: Bewertung der Baugruppenmaßhaltigkeit unter Berücksichtigung schwankender Einflussgrößen

LFT, x u. 203 Seiten, 134 Bilder, 32 Tab.
2019. ISBN 978-3-96147-176-8.

Band 320: David Meinel

Architektur applikationsspezifischer Multi-Physics-Simulationskonfiguratoren am Beispiel modularer Triebzüge

FAPS, xii u. 166 Seiten, 82 Bilder, 25 Tab.
2019. ISBN 978-3-96147-184-3.

Band 321: Andrea Zimmermann

Grundlegende Untersuchungen zum Einfluss fertigungsbedingter Eigenschaften auf die Ermüdungsfestigkeit kaltmassivumgeformter Bauteile

LFT, ix u. 160 Seiten, 66 Bilder, 5 Tab.
2019. ISBN 978-3-96147-190-4.

Band 322: Christoph Amann

Simulative Prognose der Geometrie nassgepresster Karosseriebauteile aus Gelege-Mehrschichtverbunden

LFT, xvi u. 169 Seiten, 80 Bilder, 13 Tab.
2019. ISBN 978-3-96147-194-2.

Band 323: Jennifer Tenner

Realisierung schmierstofffreier Tiefziehprozesse durch maßgeschneiderte Werkzeugoberflächen

LFT, x u. 187 Seiten, 68 Bilder, 13 Tab.
2019. ISBN 978-3-96147-196-6.

Band 324: Susan Zöller

Mapping Individual Subjective Values to Product Design

KTmfk, xi u. 223 Seiten, 81 Bilder, 25 Tab.
2019. ISBN 978-3-96147-202-4.

Band 325: Stefan Lutz

Erarbeitung einer Methodik zur semiempirischen Ermittlung der Umwandlungskinetik durchhärtender Wälzlagerstähle für die Wärmebehandlungssimulation

LFT, xiv u. 189 Seiten, 75 Bilder, 32 Tab. 2019. ISBN 978-3-96147-209-3.

Band 326: Tobias Gnibl

Modellbasierte Prozesskettenabbildung rührreibgeschweißter Aluminiumhalbzeuge zur umformtechnischen Herstellung höchstfester Leichtbaustrukturteile

LFT, xii u. 167 Seiten, 68 Bilder, 17 Tab. 2019. ISBN 978-3-96147-217-8.

Band 327: Johannes Bürner

Technisch-wirtschaftliche Optionen zur Lastflexibilisierung durch intelligente elektrische Wärmespeicher

FAPS, xiv u. 233 Seiten, 89 Bilder, 27 Tab. 2019. ISBN 978-3-96147-219-2.

Band 328: Wolfgang Böhm

Verbesserung des Umformverhaltens von mehrlagigen Aluminiumblechwerkstoffen mit ultrafeinkörnigem Gefüge

LFT, ix u. 160 Seiten, 88 Bilder, 14 Tab. 2019. ISBN 978-3-96147-227-7.

Band 329: Stefan Landkammer

Grundsatzuntersuchungen, mathematische Modellierung und Ableitung einer Auslegungsmethodik für Gelenkantriebe nach dem Spinnenbeinprinzip

LFT, xii u. 200 Seiten, 83 Bilder, 13 Tab. 2019. ISBN 978-3-96147-229-1.

Band 330: Stephan Rapp

Pump-Probe-Ellipsometrie zur Messung transienter optischer Materialeigenschaften bei der Ultrakurzpuls-Lasermaterialbearbeitung

LPT, xi u. 143 Seiten, 49 Bilder, 2 Tab. 2019. ISBN 978-3-96147-235-2.

Band 331: Michael Scholz

Intralogistics Execution System mit integrierten autonomen, servicebasierten Transportentitäten

FAPS, xi u. 195 Seiten, 55 Bilder, 11 Tab. 2019. ISBN 978-3-96147-237-6.

Band 332: Eva Bogner

Strategien der Produktindividualisierung in der produzierenden Industrie im Kontext der Digitalisierung

FAPS, ix u. 201 Seiten, 55 Bilder, 28 Tab. 2019. ISBN 978-3-96147-246-8.

Band 333: Daniel Benjamin Krüger

Ein Ansatz zur CAD-integrierten muskuloskelettalen Analyse der Mensch-Maschine-Interaktion

KTmfk, x u. 217 Seiten, 102 Bilder, 7 Tab. 2019. ISBN 978-3-96147-250-5.

Band 334: Thomas Kuhn

Qualität und Zuverlässigkeit laserdirektstrukturierter mechatronisch integrierter Baugruppen (LDS-MID)

FAPS, ix u. 152 Seiten, 69 Bilder, 12 Tab. 2019. ISBN: 978-3-96147-252-9.

Band 335: Hans Fleischmann
Modellbasierte Zustands- und Prozessüberwachung auf Basis sozio-cyber-physischer Systeme
FAPS, xi u. 214 Seiten, 111 Bilder, 18 Tab.
2019. ISBN: 978-3-96147-256-7.

Band 336: Markus Michalski
Grundlegende Untersuchungen zum Prozess- und Werkstoffverhalten bei schwingungsüberlagerter Umformung
LFT, xii u. 197 Seiten, 93 Bilder, 11 Tab.
2019. ISBN: 978-3-96147-270-3.

Band 337: Markus Brandmeier
Ganzheitliches ontologiebasiertes Wissensmanagement im Umfeld der industriellen Produktion
FAPS, xi u. 255 Seiten, 77 Bilder, 33 Tab.
2020. ISBN: 978-3-96147-275-8.

Band 338: Stephan Purr
Datenerfassung für die Anwendung lernender Algorithmen bei der Herstellung von Blechformteilen
LFT, ix u. 165 Seiten, 48 Bilder, 4 Tab.
2020. ISBN: 978-3-96147-281-9.

Band 339: Christoph Kiener
Kaltfließpressen von gerad- und schrägverzahnten Zahnrädern
LFT, viii u. 151 Seiten, 81 Bilder, 3 Tab.
2020. ISBN 978-3-96147-287-1.

Band 340: Simon Spreng
Numerische, analytische und empirische Modellierung des Heißcrimpprozesses
FAPS, xix u. 204 Seiten, 91 Bilder, 27 Tab.
2020. ISBN 978-3-96147-293-2.

Band 341: Patrik Schwingenschlögl
Erarbeitung eines Prozessverständnisses zur Verbesserung der tribologischen Bedingungen beim Presshärten
LFT, x u. 177 Seiten, 81 Bilder, 8 Tab.
2020. ISBN 978-3-96147-297-0.

Band 342: Emanuela Affronti
Evaluation of failure behaviour of sheet metals
LFT, ix u. 136 Seiten, 57 Bilder, 20 Tab.
2020. ISBN 978-3-96147-303-8.

Band 343: Julia Degner
Grundlegende Untersuchungen zur Herstellung hochfester Aluminiumblechbauteile in einem kombinierten Umform- und Abschreckprozess
LFT, x u. 172 Seiten, 61 Bilder, 9 Tab.
2020. ISBN 978-3-96147-307-6.

Band 344: Maximilian Wagner
Automatische Bahnplanung für die Aufteilung von Prozessbewegungen in synchrone Werkstück- und Werkzeugbewegungen mittels Multi-Roboter-Systemen
FAPS, xxi u. 181 Seiten, 111 Bilder, 15 Tab.
2020. ISBN 978-3-96147-309-0.

Band 345: Stefan Härter
Qualifizierung des Montageprozesses hochminiaturisierter elektronischer Bauelemente
FAPS, ix u. 194 Seiten, 97 Bilder, 28 Tab.
2020. ISBN 978-3-96147-314-4.

Band 346: Toni Donhauser
Ressourcenorientierte Auftragsregelung in einer hybriden Produktion mittels betriebsbegleitender Simulation
FAPS, xix u. 242 Seiten, 97 Bilder, 17 Tab.
2020. ISBN 978-3-96147-316-8.

Band 347: Philipp Amend
Laserbasiertes Schmelzkleben von Thermoplasten mit Metallen
LPT, xv u. 154 Seiten, 67 Bilder.
2020. ISBN 978-3-96147-326-7.

Band 348: Matthias Ehlert
Simulationsunterstützte funktionale Grenzlagenabsicherung
KTmfk, xvi u. 300 Seiten, 101 Bilder,
73 Tab. 2020. ISBN 978-3-96147-328-1.

Band 349: Thomas Sander
Ein Beitrag zur Charakterisierung und Auslegung des Verbundes von Kunststoffsubstraten mit harten Dünnschichten
KTmfk, xiv u. 178 Seiten, 88 Bilder, 21 Tab. 2020. ISBN 978-3-96147-330-4.

Band 350: Florian Pilz
Fließpressen von Verzahnungselementen an Blechen
LFT, x u. 170 Seiten, 103Bilder, 4 Tab.
2020. ISBN 978-3-96147-332-8.

Band 351: Sebastian Josef Katona
Evaluation und Aufbereitung von Produktsimulationen mittels abweichungsbehafteter Geometriemodelle
KTmfk, ix u. 147 Seiten, 73 Bilder, 11 Tab.
2020. ISBN 978-3-96147-336-6.

Band 352: Jürgen Herrmann
Kumulatives Walzplattieren. Bewertung der Umformeigenschaften mehrlagiger Blechwerkstoffe der ausscheidungshärtbaren Legierung AA6014
LFT, x u. 157 Seiten, 64 Bilder, 5 Tab.
2020. ISBN 978-3-96147-344-1.

Band 353: Christof Küstner
Assistenzsystem zur Unterstützung der datengetriebenen Produktentwicklung
KTmfk, xii u. 219 Seiten, 63 Bilder, 14 Tab.
2020. ISBN 978-3-96147-348-9.

Band 354: Tobias Gläßel
Prozessketten zum Laserstrahlschweißen von flachleiterbasierten Formspulenwicklungen für automobile Traktionsantriebe
FAPS, xiv u. 206 Seiten, 89 Bilder, 11 Tab.
2020. ISBN 978-3-96147-356-4.

Band 355: Andreas Meinel
Experimentelle Untersuchung der Auswirkungen von Axialschwingungen auf Reibung und Verschleiß in Zylinderrollenlagern
KTmfk, xii u. 162 Seiten, 56 Bilder, 7 Tab.
2020. ISBN 978-3-96147-358-8.

Band 356: Hannah Riedle
Haptische, generische Modelle weicher anatomischer Strukturen für die chirurgische Simulation
FAPS, xxx u. 179 Seiten, 82 Bilder, 35 Tab.
2020. ISBN 978-3-96147-367-0.

Band 357: Maximilian Landgraf
Leistungselektronik für den Einsatz dielektrischer Elastomere in aktorischen, sensorischen und integrierten sensomotorischen Systemen
FAPS, xxiii u. 166 Seiten, 71 Bilder, 10 Tab.
2020. ISBN 978-3-96147-380-9.

Band 358: Alireza Esfandyari
Multi-Objective Process Optimization for Overpressure Reflow Soldering in Electronics Production
FAPS, xviii u. 175 Seiten, 57 Bilder, 23 Tab.
2020. ISBN 978-3-96147-382-3.

Band 359: Christian Sand
Prozessübergreifende Analyse komplexer Montageprozessketten mittels Data Mining
FAPS, XV u. 168 Seiten, 61 Bilder, 12 Tab. 2021. ISBN 978-3-96147-398-4.

Band 360: Ralf Merkl
Closed-Loop Control of a Storage-Supported Hybrid Compensation System for Improving the Power Quality in Medium Voltage Networks
FAPS, xxvii u. 200 Seiten, 102 Bilder, 2 Tab. 2021. ISBN 978-3-96147-402-8.

Band 361: Thomas Reitberger
Additive Fertigung polymerer optischer Wellenleiter im Aerosol-Jet-Verfahren
FAPS, xix u. 141 Seiten, 65 Bilder, 11 Tab. 2021. ISBN 978-3-96147-400-4.

Band 362: Marius Christian Fechter
Modellierung von Vorentwürfen in der virtuellen Realität mit natürlicher Fingerinteraktion
KTmfk, x u. 188 Seiten, 67 Bilder, 19 Tab. 2021. ISBN 978-3-96147-404-2.

Band 363: Franziska Neubauer
Oberflächenmodifizierung und Entwicklung einer Auswertemethodik zur Verschleißcharakterisierung im Presshärteprozess
LFT, ix u. 177 Seiten, 42 Bilder, 6 Tab. 2021. ISBN 978-3-96147-406-6.

Band 364: Eike Wolfram Schäffer
Web- und wissensbasierter Engineering-Konfigurator für roboterzentrierte Automatisierungslösungen
FAPS, xxiv u. 195 Seiten, 108 Bilder, 25 Tab. 2021. ISBN 978-3-96147-410-3.

Band 365: Daniel Gross
Untersuchungen zur kohlenstoffdioxidbasierten kryogenen Minimalmengenschmierung
REP, xii u. 184 Seiten, 56 Bilder, 18 Tab. 2021. ISBN 978-3-96147-412-7.

Band 366: Daniel Junker
Qualifizierung laser-additiv gefertigter Komponenten für den Einsatz im Werkzeugbau der Massivumformung
LFT, vii u. 142 Seiten, 62 Bilder, 5 Tab. 2021. ISBN 978-3-96147-416-5.

Band 367: Tallal Javied
Totally Integrated Ecology Management for Resource Efficient and Eco-Friendly Production
FAPS, xv u. 160 Seiten, 60 Bilder, 13 Tab. 2021. ISBN 978-3-96147-418-9.

Band 368: David Marco Hochrein
Wälzlager im Beschleunigungsfeld – Eine Analysestrategie zur Bestimmung des Reibungs-, Axialschub- und Temperaturverhaltens von Nadelkränzen –
KTmfk, xiii u. 279 Seiten, 108 Bilder, 39 Tab. 2021. ISBN 978-3-96147-420-2.

Band 369: Daniel Gräf
Funktionalisierung technischer Oberflächen mittels prozessüberwachter aerosolbasierter Drucktechnologie
FAPS, xxii u. 175 Seiten, 97 Bilder, 6 Tab.
2021. ISBN 978-3-96147-433-2.

Band 370: Andreas Gröschl
Hochfrequent fokusabstandsmodulierte Konfokalsensoren für die Nanokoordinatenmesstechnik
FMT, x u. 144 Seiten, 98 Bilder, 6 Tab.
2021. ISBN 978-3-96147-435-6.

Band 371: Johann Tüchsen
Konzeption, Entwicklung und Einführung des Assistenzsystems D-DAS für die Produktentwicklung elektrischer Motoren
KTmfk, xii u. 178 Seiten, 92 Bilder, 12 Tab.
2021. ISBN 978-3-96147-437-0.

Band 372: Max Marian
Numerische Auslegung von Oberflächenmikrotexturen für geschmierte tribologische Kontakte
KTmfk, xviii u. 276 Seiten, 85 Bilder, 45 Tab. 2021. ISBN 978-3-96147-439-4.

Band 373: Johannes Strauß
Die akustooptische Strahlformung in der Lasermaterialbearbeitung
LPT, xvi u. 113 Seiten, 48 Bilder.
2021. ISBN 978-3-96147-441-7.

Band 374: Martin Hohmann
Machine learning and hyper spectral imaging: Multi Spectral Endoscopy in the Gastro Intestinal Tract towards Hyper Spectral Endoscopy
LPT, x u. 137 Seiten, 62 Bilder, 29 Tab.
2021. ISBN 978-3-96147-445-5.

Band 375: Timo Kordaß
Lasergestütztes Verfahren zur selektiven Metallisierung von epoxidharzbasierten Duromeren zur Steigerung der Integrationsdichte für dreidimensionale mechatronische Package-Baugruppen
FAPS, xviii u. 198 Seiten, 92 Bilder, 24 Tab. 2021. ISBN 978-3-96147-443-1.

Band 376: Philipp Kestel
Assistenzsystem für den wissensbasierten Aufbau konstruktionsbegleitender Finite-Elemente-Analysen
KTmfk, xviii u. 209 Seiten, 57 Bilder, 17 Tab. 2021. ISBN 978-3-96147-457-8.

Band 377: Martin Lerchen
Messverfahren für die pulverbettbasierte additive Fertigung zur Sicherstellung der Konformität mit geometrischen Produktspezifikationen
FMT, x u. 150 Seiten, 60 Bilder, 9 Tab.
2021. ISBN 978-3- 96147-463-9.

Band 378: Michael Schneider
Inline-Prüfung der Permeabilität in weichmagnetischen Komponenten
FAPS, xxii u. 189 Seiten, 79 Bilder, 14 Tab.
2021. ISBN 978-3-96147-465-3.

Band 379: Tobias Sprügel

Sphärische Detektorflächen als Unterstützung der Produktentwicklung zur Datenanalyse im Rahmen des Digital Engineering

KTmfk, xiii u. 213 Seiten, 84 Bilder, 33 Tab. 2021. ISBN 978-3-96147-475-2.

Band 380: Tom Häfner

Multipulseffekte beim Mikro-Materialabtrag von Stahllegierungen mit Pikosekunden-Laserpulsen

LPT, xxviii u. 159 Seiten, 57 Bilder, 13 Tab. 2021. ISBN 978-3-96147-479-0.

Band 381: Björn Heling

Einsatz und Validierung virtueller Absicherungsmethoden für abweichungsbehaftete Mechanismen im Kontext des Robust Design

KTmfk, xi u. 169 Seiten, 63 Bilder, 27 Tab. 2021. ISBN 978-3-96147-487-5.

Band 382: Tobias Kolb

Laserstrahl-Schmelzen von Metallen mit einer Serienanlage – Prozesscharakterisierung und Erweiterung eines Überwachungssystems

LPT, xv u. 170 Seiten, 128 Bilder, 16 Tab. 2021. ISBN 978-3-96147-491-2.

Band 383: Mario Meinhardt

Widerstandselementschweißen mit gestauchten Hilfsfügeelementen - Umformtechnische Wirkzusammenhänge zur Beeinflussung der Verbindungsfestigkeit

LFT, xii u. 189 Seiten, 87 Bilder, 4 Tab. 2022. ISBN 978-3-96147-473-8.

Band 384: Felix Bauer

Ein Beitrag zur digitalen Auslegung von Fügeprozessen im Karosseriebau mit Fokus auf das Remote-Laserstrahlschweißen unter Einsatz flexibler Spanntechnik

LFT, xi u. 185 Seiten, 74 Bilder, 12 Tab. 2022. ISBN 978-3-96147-498-1.

Band 385: Jochen Zeitler

Konzeption eines rechnergestützten Konstruktionssystems für optomechatronische Baugruppen

FAPS, xix u. 172 Seiten, 88 Bilder, 11 Tab. 2022. ISBN 978-3-96147-499-8.

Band 386: Vincent Mann

Einfluss von Strahloszillation auf das Laserstrahlschweißen hochfester Stähle

LPT, xiii u. 172 Seiten, 103 Bilder, 18 Tab. 2022. ISBN 978-3-96147-503-2.

Band 387: Chen Chen

Skin-equivalent opto-/elastofluidic in-vitro microphysiological vascular models for translational studies of optical biopsies

LPT, xx u. 126 Seiten, 60 Bilder, 10 Tab. 2022. ISBN 978-3-96147-505-6.

Kurzzusammenfassung

Die hautäquivalenten opto-/elastofluidischen mikrophysiologischen In-vitro-Gefäßmodelle werden als funktionelle Validierungstesttafeln zur Bewertung der Korrektheit der biooptischen Messungen/Bildgebung vorbereitet. Die opto-/elastofluidischen Modelle werden mit dem Einsatz von TiO_2/molekularen Farbstoffen konstruiert. Die Gewebeäquivalenzen zum Hautgewebe des Menschen werden charakterisiert. Es wird bewiesen, dass diese Opto-/Elastofluidik einem hohen Flüssigkeitsdruck von bis zu 6 bar und einer hohen Durchflussrate von 10 mL/min standhalten kann, um die Simulation der realen Bluthydraulik zu ermöglichen. Die optischen Parameter μ_a und μ_s' der Haut von menschlichen Probanden werden in den elastofluidischen Phantomen simuliert. Die Elastizitätsmoduln E der elastofluidischen Phantommatrizen werden so manipuliert, dass sie auf die mechanische Belastung genauso reagieren wie die reale weiche Hautkutis. Die Schallgeschwindigkeit, die sich durch die PVCp-Matrizen ausbreitet, wird auf 1350 bis 1500 m/s eingestellt, was der Geschwindigkeit im realen Gewebe von etwa 1540 m/s nahe kommt. Die diffuse optische Biopsie dient zur Messung der optischen Weglängenfaktoren aller wichtigen Chromophore der in den Phantomen enthaltenen künstlichen Hämoglobinverdünnungen. Sowohl für sauerstoffhaltiges als auch für sauerstoffarmes Hämoglobin sind die Konzentrationsabhängigkeiten der optischen Weglängenfaktoren definiert als $f_{Pf}(Ct) \sim Ct^{-0.5}$. Humanexperimente werden an Spinnennävi und Knötchenläsionen durchgeführt und belegen die Gewebeäquivalenzen der mikrophysiologischen elastofluidischen Hautmodelle.

The skin equivalent opto-/elastofluidic in-vitro microphysiological vascular models are prepared as the functional validation test charts to evaluate the correctness of the bio-optical measurements/ imaging. The opto-/elastofluidic models are constructed with the TiO_2/molecular dye insertions. The tissue equivalences to the cutaneous tissue of human are characterized. It is proved that these opto-/elastofluidics can withstand high liquid pressure up to 6 bar and high flow rate of 10 mL/min to allow the simulation of the real blood hydraulics. It is also proved that the in-vivo skin optical parameters μ_a and μ'_s of the human volunteers match the elastofluidic phantoms. The Young's moduli E of the elastofluidic phantom matrices are manipulated to give the same reaction to the mechanical load as the real soft skin cutis. The speed of sound propagating through the PVCp matrices is tailored at 1350 to 1500 m/s, which approach that in the real tissue of about 1540 m/s. The diffuse optical biopsy is built to measure the optical path length factors of all major chromophores of the artificial hemoglobin dilutions included in the phantoms. For both oxy- and deoxygenated hemoglobin, the concentration dependencies of the optical path length factors are defined as $f_{Pf}(Ct) \sim Ct^{0.5}$. Preliminary human experiments are done on the suspicious spider nevi and the embedded nodule lesion, and prove the tissue equivalences of the microphysiological elastofluidic skin models.

ISBN 978-3-96147-505-6

FAU UNIVERSITY PRESS 2022